Solution Plasma Synthesis of Heterographene
for Energy Conversion System

Seunghyo Lee

Solution Plasma Synthesis of Heterographene
for Energy Conversion System

ソリューションプラズマによるエネルギー変換用
ヘテログラフェンの作製

A Doctoral Dissertation by

Seunghyo Lee

2018

Graduate School of Engineering,

Department of Materials, Physics and Energy Engineering,

Nagoya University

In partial fulfillment of the requirements for the degree of

Doctor of Engineering

Table of contents

Chapter 1 –General introduction

Chapter 2 – Generation of non-equilibrium condition in solution plasma discharge using low-pass filter circuit

Chapter 3 – Enhancement of Nitrogen Self-Doped Nanocarbons Electrocatalyst Activity via Tune-up Solution Plasma

Chapter 4 – Solution Plasma Synthesis of Boron-Carbon-Nitrogen Catalyst with Controllable Bond Structure

Chapter 5 – Summary

Achievements

Acknowledgements

Abstract

Efficient electrocatalyst for the oxygen reduction reaction (ORR) have attracted widespread attention to accomplish optimal performance for application in energy conversion systems such as fuel cell (FC) and metal-air batteries (MABs). However, the catalysts on the cathode suffer from several critical obstacles, and the possible commercialization of FC and MABs is difficult due to the inherent sluggish kinetics and high overpotential in the ORR. Currently, platinum (Pt) and platinum supported on carbon materials (Pt/C) are regarded as the best issues to solve these problems because of a four-electron reduction pathway in ORR process but, prohibitive cost, low reserves, and methanol tolerance interrupt the development of the large-scale commercialization. In this regard, ongoing research efforts have been devoted searching to replace Pt with Pt-free catalyst with highly efficient performance, selectivity, and durability, such as non-precious metal supported on nanocarbons, or metal-free heterogeneous nanocarbons. Among them, the metal-free heterogeneous nanocarbons have been regarded as one of the most prominent alternatives for the ORR electrocatalyst when they incorporate heteroatoms (e.g. N, B, P, S, and I) into the carbonaceous skeleton.

Solution Plasma (SP), a non-equilibrium discharge in liquids at atmospheric pressure and room temperature, has emerged as a useful synthetic method for various nanomaterial such as nanoparticles, nanocarbons, heterogeneous nanocarbons, and transition metal-carbon composites. Among these nanomaterials, the most interesting achievement is the formation of heterogeneous nanocarbons. However, the conventional SP synthesis is still at a beginning stage in the field of carbon fabrication and, especially, difficult to control the morphology, structure, and bonding configuration between carbon and the doped heteroatoms. To overcome these limitations, we have developed the tune-up SP system which is composed of a low-pass filter circuit to improve the discharge stability by controlling the current oscillations.

In Chapter 2, a low-pass filter circuit was introduced to increase the density and temperature of electrons involved in a non-equilibrium condition. The discharge properties of the solution plasma generated by conventional and low-pass filter circuits were characterized and comparatively analyzed. Filtration of the MHz range current oscillations, an increase in the maximum discharge current, and a higher stability of solution plasma were obtained by simply inserting a resistorcapacitor (RC) component in the circuit, which leads to the increases in the density and temperature of electrons. This novel strategy using a low pass filter circuit provides plasma stability and energy control during the discharge in liquid.

Applying a low-pass filter circuit in solution plasma synthesis, in terms of a tune-up solution plasma (SP) synthesis, Chapter 3 researches to the fabrication of nitrogen doped nanocarbons depending on a low-pass filter circuit. We suggest a tune-up SP synthesis based on a simple one step and cost-effective method to fabricate nitrogen self-doped graphitic carbon nanosheets (NGS) as an electrocatalyst. This novel strategy using a low pass filter circuit provides plasma stability and energy control during the discharge in pyridine, determining the graphitic structure of nanocarbons doped with nitrogen. Notably, NGS has the relatively high surface area (621 m^2/g), and high contents of nitrogen bonded as pyridinic-N and pyrrolic-N with 55.5 and 21.3 at. %, respectively. As an efficient metal-free electrocatalyst, NGS exhibits a high onset potential (-0.18 V vs. Ag/AgCl) and 3.8 transferred electrons pathway for ORR in alkaline solution, as well as better long-term durability (4% current decreases after 10000 s operation) than the commercial Pt/C (22% current drop).

On the other hands, boron-carbon-nitrogen (BCN) ternary systems with graphitic phase have been highlighted for their novel structural and electronic properties. Interestingly, BCN hetero-nanocarbons can be regarded as alternative low-cost metal-free electrocatalysts for oxygen reduction reaction (ORR). Hence, in chapter 4, using selected precursors a new strategy for the

simultaneous synthesis of nanocarbon co-doped with heteroatoms was found. The synergetic effect of N and B in an uncoupling bond state improved the formation of new active sites for the ORR performance by changing the electronic structure of the base carbon. Meanwhile, when B and N are bonded together, the BCN catalyst contributes to a reduced ORR activity by forming a balanced electronic structure in carbon. The BCN nanocarbon with uncoupling bond state exhibits an enhanced ORR activity under alkaline conditions, with onset potential of -0.25 V versus -0.31 V for B/N coupling and 3.43 transferred electrons during the ORR. Although the ORR activity of the B/N uncoupling nanocarbon was not as good as the typical Pt/C, the durability of this synthesized material (15.1 % current decrease after 20000 s of operation) was significantly better than that of the Pt/C catalyst (61. 5 % current drop under the same conditions). After durability test, the increase of the chemical states containing oxygen was higher for Pt/C than B/N uncoupling.

In summary, we suggest a novel route to synthesize hetero-nanocarbons using a tune-up solution plasma system. The proposed method gives several advantages over assembling of nanocarbons: (a) one-step process, (b) ambient reaction environment, (c) straightforward and easy setup, (d) cost-effective production, (e) possible large-scale of synthesis quantities, and (f) eco-friend fabrication. In particular, the tune-up SP synthesis provides stability during the discharge in liquid, influencing the synthesized nanocarbon characteristics. In detail, the electrochemical measurements demonstrate a comparable catalytic activity and superior stability to Pt/C in alkaline medium, so that a low cost and large scale of hetero-nanocarbons is a promising candidate for the next generation of electrocatalyst in metal-air batteries.
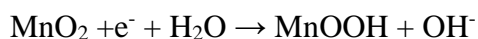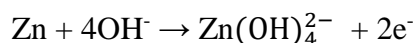
Chapter 1
General introduction
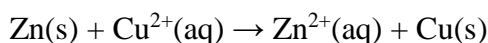
Chapter 1 General introduction

1.1 Electrocatalytic Oxygen Reduction Reactions (ORR)

A typical electrochemical reaction is the reaction occurring in the cell. For example, in the zinc electrode, zinc atom is transferred to zinc hydroxide ion with loss of electron. And the following reaction is occurring in the manganese dioxide electrode.

$$Zn + 4OH^- \rightarrow Zn(OH)_4^{2-} + 2e^-$$

$$MnO_2 + e^- + H_2O \rightarrow MnOOH + OH^-$$

These reactions are known as main reactions in alkaline cell, the first reaction is oxidation of the zinc with the loss of electrons and the next reaction is reduction of the manganese dioxide with gain of electrons. As shown above, the electrochemical reaction is oxidation reaction or reduction reaction. This pair of reactions, so called redox reactions, involves in chemical reaction by the transfer of electrons. The oxidation is occurring in one electrode and the reduction is occurring in the counter electrode during electrochemical reaction process. The difference with common chemical redox reaction is that it does not directly transfer electron between oxidized and reduced molecules and the electrons transferred from the electrode to the other electrode via connected leading wire. In this cell, the electrode which occurring oxidation called anode and occurring reduction called cathode.

The whole-cell reaction of Daniel cell (Zn│Zn^{2+} ∷ Cu^{2+}│Cu) is as fallows.

$$Zn(s) + Cu^{2+}(aq) \rightarrow Zn^{2+}(aq) + Cu(s)$$

The chemical potential (μ_i) of a chemical species i means that the rate of increase of Gibbs free energy (G) is related to mole fraction, which defined as $(\partial G/\partial n_i)_{T, p}$. When chemical species i exist in both phase and their concentration in equilibrium, μ_i are at the same levee. According to the activity a_i, μ_i increases as $\mu_i = \mu_i° + RT \ln a_i$. The μ_i of Cu^{2+}(aq) and Zn^{2+}(aq) are as shown below according to each activity.

$$\mu_{Zn^{2+}} = \mu°_{Zn^{2+}} + RT \ln a_{Zn^{2+}}$$

$$\mu_{Cu^{2+}} = \mu°_{Cu^{2+}} + RT \ln a_{Cu^{2+}}$$

The μ_i of the solid Zn(s) and Cu(s) have no change in concentration which are constant as $\mu°_{Zn}$ and $\mu°_{Cu}$, thus, the ΔG in this reaction is as follows,

$$\Delta G = \mu_{Zn^{2+}} + \mu°_{Cu} - \mu_{Cu^{2+}} - \mu°_{Zn}$$

$$= \mu°_{Zn^{2+}} + RT \ln a_{Zn^{2+}} + \mu°_{Cu} - (\mu°_{Cu^{2+}} + RT \ln a_{Cu^{2+}} + \mu°_{Zn})$$

$$= \Delta G° + RT \ln \frac{a_{Zn^{2+}}}{a_{Cu^{2+}}}$$

where $a_{Zn^{2+}}$ and $a_{Cu^{2+}}$ are μ_i of two chemical species and $\Delta G°$ is ΔG when both of μ_i have a value of one. The concentration of $a_{Zn^{2+}}$ and $a_{Cu^{2+}}$ can change to $[Zn^{2+}]$ and $[Zn^{2+}]$, because the activity rate has almost same level with concentration rate in the dilute solution.

$$\Delta G \cong \Delta G° + RT \ln \frac{[Zn^{2+}]}{[Cu^{2+}]}$$

The Cu electrode becomes positive pole owing to electron loss while the Zn electrode becomes negative pole owing to electron gain. However, this decline of free energy must have same level with a charged network in the cell, thus the Cu electrode potential is higher than that of Zn electrode and their gap designate E_{cell} as cell potential.

$$\Delta G = -nFE_{cell}$$

$$\Delta G° = -nFE°_{cell}$$

where $E°_{cell}$ is standard cell potential and from the relation shown above the Nernst equation as given below,

$$E_{cell} = E°_{cell} + \frac{RT}{2F} \ln \frac{a_{Zn^{2+}}}{a_{Cu^{2+}}}$$

$$= E°_{cell} + 2.303 \frac{RT}{2F} \log \frac{a_{Zn^{2+}}}{a_{Cu^{2+}}}$$

$$\cong E°_{cell} + 2.303 \frac{RT}{2F} \log \frac{[Zn^{2+}]}{[Cu^{2+}]}$$

1.2 Mechanism for Oxygen Reduction Reaction

The oxygen reduction reaction (ORR) is one of the important reactions in energy conversion device systems including fuel cells and metal-air battery. The ORR is irreversible and quite complicate reaction which involves various intermediates. The schematic ORR process under acidic and alkaline electrolyte shown in the Fig 1.1. In the aqueous electrolyte, the ORR is classified into two types of reduction pathway. (1) Direct 4 electron reduction pathway produce to H_2O or OH^- from O_2. (2) Indirect 2 electron reduction pathway produces to H_2O or OH^- from O_2 through hydrogen peroxide or peroxide anion as intermediates. The standard electrode potentials of direct process are 1.23 V and 0.40 V, respectively, under acidic and alkaline conditions. The different in potential is corresponding to the different chemical reaction involves in that specific pH range. The standard potential decreases approximately 0.059 V/pH as increase the pH value.

(a)

Electrolyte	ORR reaction	Standard electrode Potential (V)
Acidic media	Direct : $O_2 + 4H^+ + 4e^- \rightarrow H_2O$ Indirect : $O_2 + 2H^+ + 2e^- \rightarrow H_2O_2$ $H_2O_2 + 2H^+ + 2e^- \rightarrow 2H_2O$	$E^o = 1.23$ V $E^o = 0.70$ V $E^o = 1.76$ V
Alkaline media	Direct : $O_2 + 2H_2O + 4e^- \rightarrow 4OH^-$ Indirect : $O_2 + H_2O + 2e^- \rightarrow HO_2^- + OH^-$ $HO_2^- + H_2O + 2e^- \rightarrow 3OH^-$	$E^o = 0.40$ V $E^o = -0.065$ V $E^o = 0.867$ V

(b)

Acidic media

$$O_{2,aq} \longrightarrow O_{2,ads} \xrightarrow{2e^-} H_2O_{2,ads} \xrightarrow{2e^-} H_2O$$

with $4e^-$ pathway from $O_{2,ads}$ to H_2O

Alkaline media

$$O_{2,aq} \longrightarrow O_{2,ads} \xrightarrow{2e^-} HO^-_{2,ads} \xrightarrow{2e^-} H_2O$$

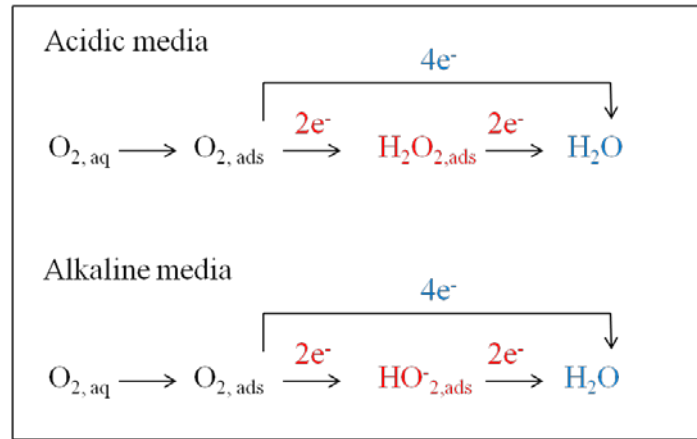with $4e^-$ pathway from $O_{2,ads}$ to H_2O

Fig. 1.1 (a) The ORR reaction and standard electrode potential (b) ORR pathway in the acidic and alkaline media.

The Butler-Volmer equation is desirable to studies electro kinetics and overpotentials on ORR. The anodic and cathodic overpotential can address by given below equation [1].

$$i = i_0 \left\{ e^{\left[\frac{(1-\alpha_{Rd})nF}{RT}(E-E_r) \right]} - e^{\left[\frac{-\alpha_{Ox}nF}{RT}(E-E_r) \right]} \right\}$$

where i is reduction current density, i_0 is exchange current density, α is transfer coefficient, n is the number of electrons transferred, F is the Faraday constant, R is the gas constant and T is operating temperature. The E_r is the reversible potential, i.e. equilibrium potential. This equilibrium potential can concluded 0 V at anode [1] and 1.229 V (25 °C, atmospheric pressure) at cathode. Potential gap between electrode potential to equilibrium potential is called overpotential which is requiring potential gap for generate current. Also, the Butler-Volmer equation can apply in both of electrodes. The anode has positive overpotential ($E_a > E_{r,a}$), thus oxidation current is mainly occurs and as followings.

$$i_a = -i_{0,\,a}\ e^{\left[\frac{-\alpha_{Ox}nF}{RT}(E_a - E_{r,a})\right]}$$

Consequently, it is signify negative current value means that the loss of electrons at electrode. Withal, the cathode overpotential has negative value ($E_c > E_{r,\,c}$), reduction current mainly occurring.

$$i_c = i_{0,\,c}\{e^{\left[\frac{(1-\alpha_{Rd})nF}{RT}(E_c - E_{r,c})\right]}$$

Plasma discharge in liquid have been investigated [1, 2] for a wide area of applications as materials synthesis [3, 4], decomposition of compounds [5, 6], and biology sterilization from harmful bacteria and compounds [7, 8]. Historically, plasma in liquids is known till 1899 by J. Wilsing and 1902 by Sir N. Lockyer who studied discharges in water for astrophysical purpose [9, 10].

1.3 Catalysts material for ORR

Many researches recently have been efforts to find other substitutions of Pt-based catalysts with compatible catalytic activity. These alternative catalysts may classify them under two large groups. The first one is metal particle based catalysts include transition metal oxides [2,3], transition metal chalcogenides [6,7], transition metal carbides [8,9], and the other one is non-particle based metal catalysts include transition metal macrocyclic compound [10-12] and metal-free hetero-atom doped carbon materials [4,5].

In this section, we focused on the particle-based and non-particle based metal

catalysts

(1) Non-noble metals alloys and oxides

Transition metal oxide with spinel and perovskite structures have attracted much more attention and exhibited desire ORR activity and durability in alkaline medium [13,14]. Many researches have been reported investigating the metal oxides as catalysts for ORR, and also, many kind of transition metal were applied to form with oxides such as W, Co, Mn, Zr, Ti, Ta, and Nb [15-19]. In recent, Dai, *et al.* reported that the cobalt oxide with N-doped graphene has ORR activity and further enhanced ORR activity by manganese cobalt oxide which closed to platinum catalysts [14]. However, these ORR activity is not only came from oxides catalyst which might be originated from synergy between oxides and N-doping. Also, tantalum was applied to form oxide, it still remain problems for ORR catalysts [20]. Even though tantalum oxide exhibited higher ORR potential, it shows very lower electrical conductivity which might bring problems about electron transportation.

(2) Transition metal chalcogenides

Recently, transition metals with chalcogen atoms such as sulfur, selenium and tellurium have attracted attention as potential catalysts for ORR [21-24]. Especially, ruthenium is most popular material as a metal part in metal chalcogenides structure. The Ru_xX_y chalcogenides has shown good enough methanol tolerance in oxygen saturated environments [25-27]. It also exhibited higher ORR activity in acidic medium. Among the Ru based catalysts, RuSe shows the highest ORR activity. And the effect of chalcogen atoms on ORR was as follows; RuSe > RuS > Ru black [22,28]. In metal chalcogenides Ru-O bonding is mainly concerned for the active site of ORR [29]. The metal core was bind with metal atom inside of matrix, and the chalcogen atoms were coordinated outside of the cluster. The amount of coordinating

chalcogen atoms are changing according to the type of it, which is affecting the interaction between core metal and oxygen [29]. Too much chalocogen atoms are disturb active site for ORR, and thus, it is necessary to optimize suitable structure [29,30]. The role of the chalcogen atom is subserve to form of active site, electronic structure, and chemically stabilizes the metal core to interact with oxygen [29].

Even though Ru based chalocogenides demonstrate good electrochemical properties for ORR, it still remain some problem in alternative catalyst. Because Ru is classified as a noble metal, and thus it can't certainly regards as non-noble metal catalyst. Therefore, recently, the researchers are focused on 3d transition metal chalcogenides, in particular iron and cobalt based chalocogenides. Reyimjan, *et al*. reported that the (200) direction of CO_9S_8 was shows similar behavior to compare with platinum on ORR in theoretical calculation [31]. Also, Feng, *et al*. synthesized Co_3S_4 which presents ORR activity, but it still incompatible to that of Ru based catalysts [32]. Susac, *et al*. reported about iron based catalyst, FeS_2 thin films was prepared by magnetron sputtering. The prepared FeS_2 was form to pyrite structure, and the ORR activity was depended on interaction with some polyslufides [33].

(3) Transition metal carbides

Transition metal carbide, in particular tungsten carbide, has attracted attentions as one of the new type non-noble catalyst due to its unique electronic structure and high resistance of carbon monoxide which offers a long-term durability [34,35]. In addition, tungsten carbide could be applied as catalysts in various chemical reactions such as hydrogen evolution and methanol oxidation reactions [36-39]. Trassatti, *et al.* reported that WC, TaC, TiC, and TiN exhibited catalytic activity for ORR in acid media [40]. However, WC did not show durability in the long-term operation. In order to further enhancing ORR activity, Lee, *et al.* reported that the WC could be improved in ORR catalytic activity and durability by the addition of Ta [41].

However, it still incomparable to other commercial catalysts. On the other hand, the addition of Ag can highly enhance catalytic activity for ORR. The Ag-WC/C exhibited comparable ORR potential to commercial catalysts [42]. From above report, it concludes that the role of WC is in catalyst which can act as a promoter and an enhancer for a better catalytic activity and stability as ORR catalyst.

Reference

[1] A. J. Bard, L. R. Faulkner, *Electrochemical methods. Fundamentals and applications,* 2. ed. ed., Wiley, New York, 2001.

[2] W. Lia, P. Haldara, *Electrochem. Solid-State Lett.*, 2010, 13, 47.

[3] H´ector R. Col´on-Mercado, Branko N. Popov, *J. Power Sources*, 2006, 155, 253.

[4] K.P. Gong, F. Du, Z.H. Xia, M. Durstock, L.M. Dai, *Science*, 2009, 323, 760.

[5] A. Sidik, B. Anderson, P. Subramanian, P. Kumaraguru, N. Popov, *J. Phys. Chem. B*, 110, 2006, 1787-1793

[6] T.J. Schmidt, U.A. Paulus, H.A. Gasteiger, N. Alonso-Vante, R.J. Behm, *J. Electrochem Soc*, 2000, 147, 2620.

[7] R.G. G. Huerrta, J.A. C. Carvayar, O. S. Feria, *J. Power Sources*, 2006, 153, 11.

[8] A.L. Stottlemyer, E.C. Weigert, J.G.G. Chen, *Ind Eng Chem Res*, 2011, 50, 16.

[9] X. Zhou, Y. Qiu, J. Yu, J. Yin, S. Gao, *J. hydrogen energy*, 2011, 36, 7398.

[10] D. Lee, W. Lee, W. Lee, S. Kim, Y. Kim, *Phys. Rev. Lett.*, 2011, 106, 175502.

[11] M. Lefèvre, E. Proietti, F. Jaouen, J.P. Dodelet, *Science*, 2009, 324, 71.

[12] J. Zagal, P. Bindra, E. A. Yeager, *J Electrochem Soc*, 1980, 127, 1506.

[13] J. Suntivich, H. A. Gasteiger, N. Yabuuchi, H. Nakanishi, J. B. Goodenough and Y. Horn1, *Nature Chemistry,* 2011, 3,546–550

[14] Y. Liang, J. Wang , T. Regier, and H. Dai, *J. Am. Chem. Soc.*, 2012, 134, 3517.

[15]S. Doi, A. Ishihara, S. Mitsushima, N. Kamiya and K. I. Ota, *J. Electrochem. Soc.*, 2007, 154, B362.

[16] A. Ishihara, K. Lee, S. Doi, S. Mitsushima, N. Kamiya, M. Hara, K. Domen, K. Fukuda and K. Ota, *Electrochem. Solid-State Lett.*, 2005, 8, A201.

[17] Y. Liu, A. Ishihara, S. Mitsushima, N. Kamiya and K. Ota, *Electrochem. Solid-State Lett.*, 2005, 8, A400.

[18] Y. Liu, A. Ishihara, S. Mitsushima, N. Kamiya and K. Ota, *J.Electrochem. Soc.*, 2007, 154, B664.

[19] Y. Liu, A. Ishihara, S. Mitsushima and K. Ota, *Electrochim. Acta*, 2010, 55, 1239.

[20] J. Kim, T. Oh, Y. Shin, J. Bonnett and K. Weil, *Int. J. Hydrogen Energy*, 2011, 36, 4557.

[21] L. Zhang, J. Zhang, D.P. Wilkinson, H. Wang, *J. Power Sources*, 2006, 156,171.

[22] D. Cao, A. Wieckowski, J. Inukai, N. Alonso-Vante, *J. Electrochem. Soc.*, 2006, 153, A869.

[23] V. Trapp, P. Christensen, A. Hamnett, *Faraday Trans.*, 1996, 92, 4311.

[24] E. Vayner, R.A. Sidik, A.B. Anderson, B.N. Popov, *J. Phys. Chem. C*, 2007, 111, 10508.

[25] O. Solorza-Feria, K. Ellmer, M. Giersig, and N. Alonso-Vante, *Electrochim. Acta*, 39, 1647, 1994.

[26] T. J. Schmidt, U. A. Paulus, H. A. Gasteiger, N. Alonso-Vante, and R. J. Behm, *J. Electrochem. Soc.*, 147, 2620, 2000.

[27] I. V. Malakhov, S. G. Nikitenko, E. R. Savinova, D. I. Kochubey, and N. Alonso-Vante, *J. Phys. Chem. B*, 106, 1670, 2002.

[28] H. Kim, I. Rabelo de Moraes, G. Tremiliosi-Filho, R. Haasch, A. Wieckowski, *Surf. Sci. Lett.*, 2001, 474, L203.

[29] N. Alonso-Vante, I.V. Malakhov, S.G. Nikitenko, E.R. Savinova, D.I. Kochubey, *Electrochim. Acta*, 2002, 47, 3807.

[30] I. V. Malakhov, S. G.Nikitenko, E. R. Savinova, D. I.Kochubey, N. Alonso-Vante, *J. Phys. Chem. B* 2002, 106, 1670.

[31] R. A. Sidik and A. B. Anderson, *J. Phys. Chem. B* 2006, 110, 936.

[32] Y. Feng, T. He and N. Alonso-Vante, *Chem. Mater.* 2008, *20,* 26.

[33] D. Susac, L. Zhu, M. Teo, A. Sode, K. C. Wong, P. C. Wong, R. R. Parsons, D. Bizzotto, K.A. R. Mitchell, and S. A. Campbell, *J. Phys. Chem. C,* 2007, 111, 18715.

[34] V. Nikolova, I. Nikolova, P. Andreev, V. Najdenov, T. Vitanov, *J. Appl. Electrochem.*, 2000,

30, 705.

[35] K. Lee, A. Ishihara, S. Mitsushima, N. Kamiya, K.I. Ota, *Electrochim. Acta*, 2004, 49, 3479.

[36] L.H. Bennett, J.R. Cuthill, A.J. McAlister, N.E. Erickson, R.E. Watson, *Science*, 1974, 184, 563.

[37] R. Ganesan, J.S. Lee, *Angew. Chem. Int. Ed.*, 2005, 44, 6557.

[38] P.N. Ross Jr., P. Stonehart, *J. Catal.*, 1977, 48, 42.

[39] H. Meng, P.K. Shen, *J. Phys. Chem. B*, 2005, 109, 22705.

[40] F. Mazza, S. Trassatti, *J. Electrochem Soc.* 1963, 110, 847.

[41] Lee K, Ishihara A, Mitsushima S, Kamiya N, Ota K, *Electrochim Acta*, 2004, 49, 3479.

[42] H. Meng, P.K. Shen, *Electrochem. Commun.* 2006, 8, 588.

Chapter 2
Generation of non-equilibrium condition
in solution plasma discharge
using low-pass filter circuit

Chapter 2 Generation of non-equilibrium condition in solution plasma discharge using low-pass filter circuit

2.1 Introduction

Plasma discharge in liquid have been investigated [1, 2] for a wide area of applications as materials synthesis [3, 4], decomposition of compounds [5, 6], and biology sterilization from harmful bacteria and compounds [7, 8]. Historically, plasma in liquids is known till 1899 by J. Wilsing and 1902 by Sir N. Lockyer who studied discharges in water for astrophysical purpose [9, 10].

The processes in the discharge in liquids are similar with the processes from an atmospheric pressure plasma where excited and ionized atoms, molecules, and radicals are produced by elastic and inelastic collisions and plasma can be characterized by its density and temperature [1-9, 11]. In an atmospheric pressure plasma most of the excited species have a short lifetime and return to lower excited or ground levels by emitting a photon. The metastable states decay by energy transfer through collisions. Plasma in liquid processing has one important advantage since different states of materials can be treated inside this plasma. In a typical gas phase plasma the gas is supplied for generation the discharge in vacuum or at atmospheric pressure. In the discharge in liquids, plasma can be produced starting from a liquid where different solid compounds can be dissolved or various gases can be introduced. This means that in this plasma, gases, liquids, and solid compounds could be processed and new possibilities for material synthesis are open [12-14]. In addition, the electrode material can be combined with the species from the liquid phase and new materials with new properties can be

obtained [1-4, 12-16].

When plasma obeys the local thermal equilibrium (LTE) condition, it is defined as "hot plasma" or "thermal plasma" where the temperature of ions is similar to that of electrons [3, 5, 6, 11, 16-19].   In thermal plasma, the ion exerts dominant reaction within solution chemistry since the mass of ions is much higher than the mass of electrons. As a result, the thermal effect contributes significantly to the reaction field. With a higher reactivity and temperature within the plasma field, most of the reactions will be limited to irreversible chemical reactions by energy equilibrium condition. On the other hand, a non-equilibrium condition at which the density and temperature of electrons are higher than those of ions can occur if plasma operates as a glow discharge or cold plasma, including the chemical reaction by provide electrons rather than thermal effect.

Recently, a particular type of plasma discharge in liquid was re-defined by Takai and Saito.[12,13,16,17,20–44] Our group has expanded the research field of "plasma discharge in liquid" to "solution plasma (SP)"with the concept of varying the "solution" media including its chemical reaction. The chemical reaction can be controlled by solution chemistry such as the concentration, conductivity, or pH of aqueous solutions or by simply employing another organic compound in liquid form. The SP which induces both the LTE condition and non-equilibrium condition is favorable to synthesize metastable materials with new characteristics by dominating the non-equilibrium condition. In this study, a low-pass filter circuit was introduced to increase the density and temperature of electrons mainly involved in the non-equilibrium condition. The discharge properties of the solution plasma generated by conventional and low-pass filter circuits were characterized and comparatively analyzed.

2.2 Experimental procedure

Fig. 2.1 shows a typical plasma device which is composed of the bipolar pulsed power supply (MPS - R06K01C - WP1 - 6CH, Kurita, Japan) (Fig. 2.2 (a)), the pin to pin discharge device (Shinku, Japan) (Fig. 2.2 (b)). The primary voltage could be converted from the input three-phase voltage of 115 V to a maximum output voltage of 4 kV using a transformer, according to the relationship $\frac{n_1}{n_2} = \frac{V_1}{V_2} = \frac{I_2}{I_1} = \sqrt{\frac{Z_1}{Z_2}}$, $n_1 : n_2 = 1 : 16$, where n, V, I, and Z are the number of active coils, voltage, current, and impedance. The bipolar signal with the frequency in the range from 1 ~ 50 kHz and the pulse width in the range of 1 ~ 10 s could be generated by using a pulse modulator. The output phase was perfectly confirmed as $v(t) = (V_{setup} \times \frac{t}{2})$, where $v(t)$, V_{setup} and t are the time related voltage function, set voltage, and time as is shown in Fig. 2.3.

A tree-axes glass vessel with a volume of 200 mL was designed to fix the discharge electrodes and the optical fiber. A pair of tungsten wires with 0.6 mm diameter was used as electrodes with a gap distance adjusted to be 0.5 mm. In this experiment the solution media was deionized water.

The conventional circuit consists in the bipolar pulsed power supply and the pin to pin discharge device as shown in Fig. 2.1 (a) and Fig. 2.2 [12-17, 20-44]. A low pass filter circuit, which is denoted as the oscillation filter part, was constructed using a parallel capacitor of 2 nF and two resistors in series with $50\,\Omega$ and $100\,\Omega$. The SP was generated in the same power conditions for each circuit. The applied voltage, the repetition frequency, the pulse width, and the discharge time were strictly controlled to be 1.6 kV, 30 kHz, 2.0 μs and 20 min.,

respectively.

The optical emission spectrum (OES) during plasma discharge was recorded by a spectrograph (USB4000, Ocean Optics, USA) with an integration time of 100 ms. The optical fiber (P400-2-UV/VIS, Ocean Optics, USA) was fixed in a quartz tube above the discharge. In order to analyze the excited species, the resolution and instrumental broadenings of the collected optical emission light were measured to be 0.44 nm and 0.7 nm, respectively [13]. The current-voltage waveform was measured using an oscilloscope (DLM 2024, Yokogawa, Japan) with a current probe (PBC 50 and PBC 100, 50 and 100 MHz respectively, Yokogawa, Japan) and a differential high voltage probe (PBDH 0150, 150 MHz, Yokogawa, Japan). In addition, water temperature was measured using an IR camera (InfraRed, NEC Avio, Japan) with an automatic recording interval of 5 s.
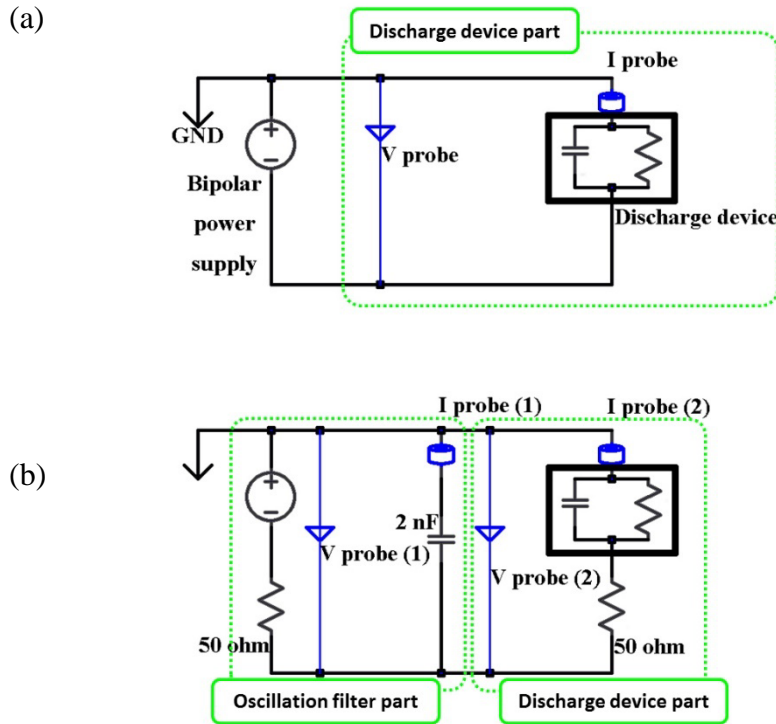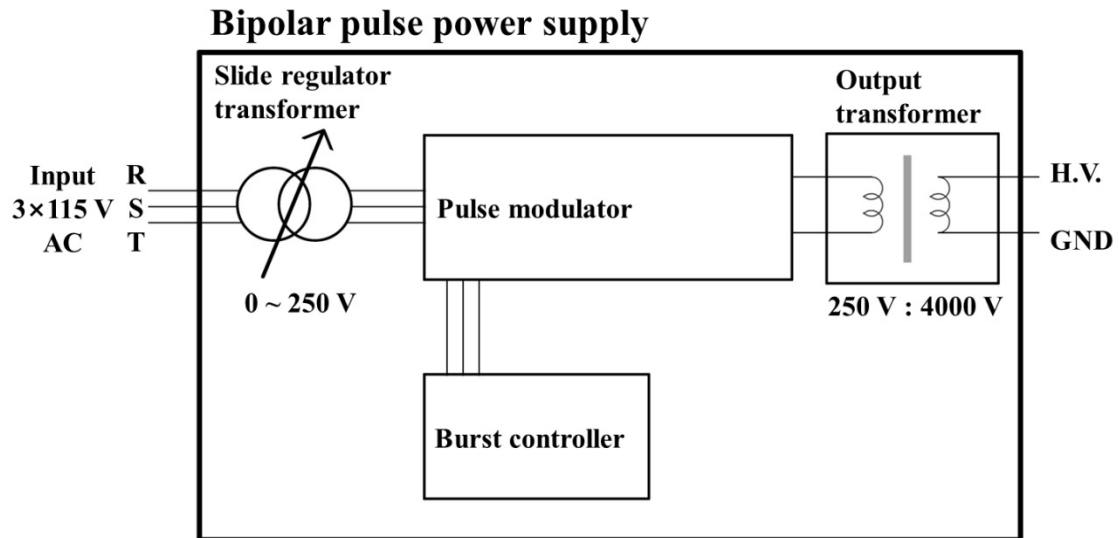

Fig. 2.1. Schematics setup of the solution plasma process with (a) the conventional circuit and (b) the low pass filter circuit.
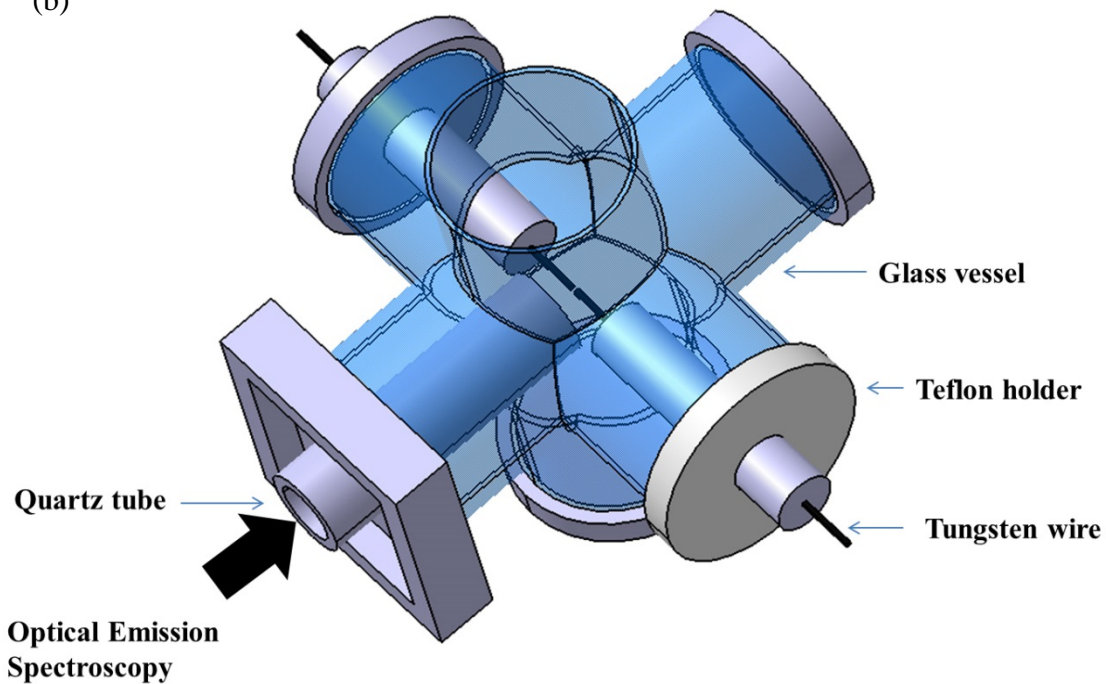
(a)

Bipolar pulse power supply

Slide regulator
transformer

Output
transformer

Input   R
3×115 V S
AC   T

Pulse modulator

0 ~ 250 V

H.V.

GND

250 V : 4000 V

Burst controller

(b)

Glass vessel

Teflon holder

Quartz tube

Tungsten wire

Optical Emission
Spectroscopy

Fig. 2.2. Diagram of solution plasma setup: (a) the bipolar pulsed power supply and (b) the pin to pin discharge device.
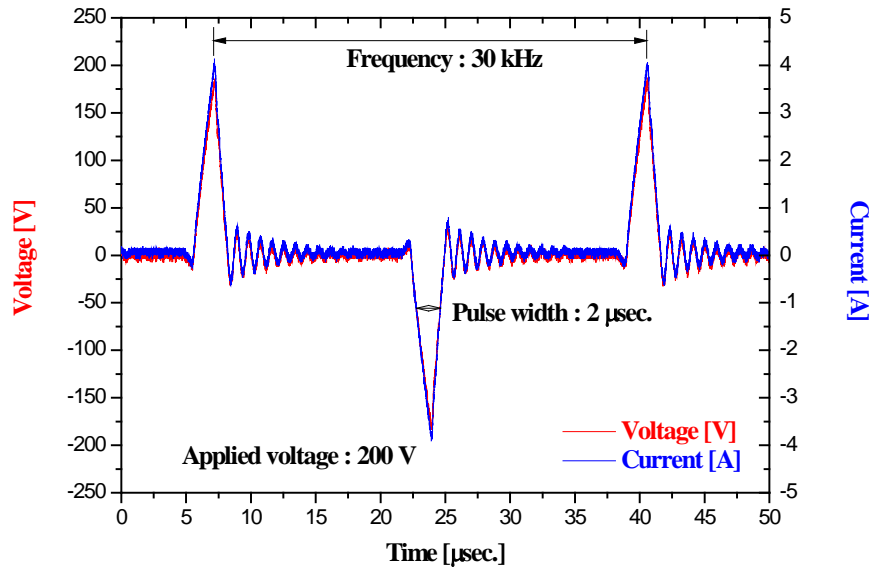
Fig. 2.3. Current-voltage waveform through the circuit when a resistor of 50 Ω was directly connected to the power supply. The applied voltage of 200 V is on the slide regulator transformer.

The conventional circuit consists in the bipolar pulsed power supply and the pin to pin discharge device as shown in Fig. 2.1 (a) and Fig. 2.2 [12-17, 20-44]. A low pass filter circuit, which is denoted as the oscillation filter part, was constructed using a parallel capacitor of 2 nF and two resistors in series with 50 Ω and 100 Ω. The SP was generated in the same power conditions for each circuit. The applied voltage, the repetition frequency, the pulse width, and the discharge time were strictly controlled to be 1.6 kV, 30 kHz, 2.0 μs and 20 min., respectively.

The optical emission spectrum (OES) during plasma discharge was recorded by a spectrograph (USB4000, Ocean Optics, USA) with an integration time of 100 ms. The optical fiber (P400-2-UV/VIS, Ocean Optics, USA) was fixed in a quartz tube above the discharge. In order to analyze the excited species, the resolution and instrumental broadenings of the

23

collected optical emission light were measured to be 0.44 nm and 0.7 nm, respectively [13]. The current-voltage waveform was measured using an oscilloscope (DLM 2024, Yokogawa, Japan) with a current probe (PBC 50 and PBC 100, 50 and 100 MHz respectively, Yokogawa, Japan) and a differential high voltage probe (PBDH 0150, 150 MHz, Yokogawa, Japan). In addition, water temperature was measured using an IR camera (InfraRed, NEC Avio, Japan) with an automatic recording interval of 5 s.

2.3 Results and discussion

2.3.1 Electrical properties of the solution plasma

The electrical properties of the SP were analyzed from the current-voltage waveforms for each type of circuit as shown in Fig. 2.4. To simply explain the mechanism of the SP, the waveform corresponding to the discharge during one pulse was divided into following four stages depending on the voltage and current conditions.

> **i) The steady condition**: The voltage is off (0 V), as is the current is 0 A.
>
> **ii) The applied voltage stage**: The voltage is on with a value of 1600V for 2 μs of pulse width, and the current becomes a few microamperes.
>
> **iii) The breakdown stage**: the voltage is on and decreases to a lower value and the current rapidly increases.
>
> **iv) The plasma generation stage**: the discharge current flows with a maximum value of 6-13 A depending on the circuit.
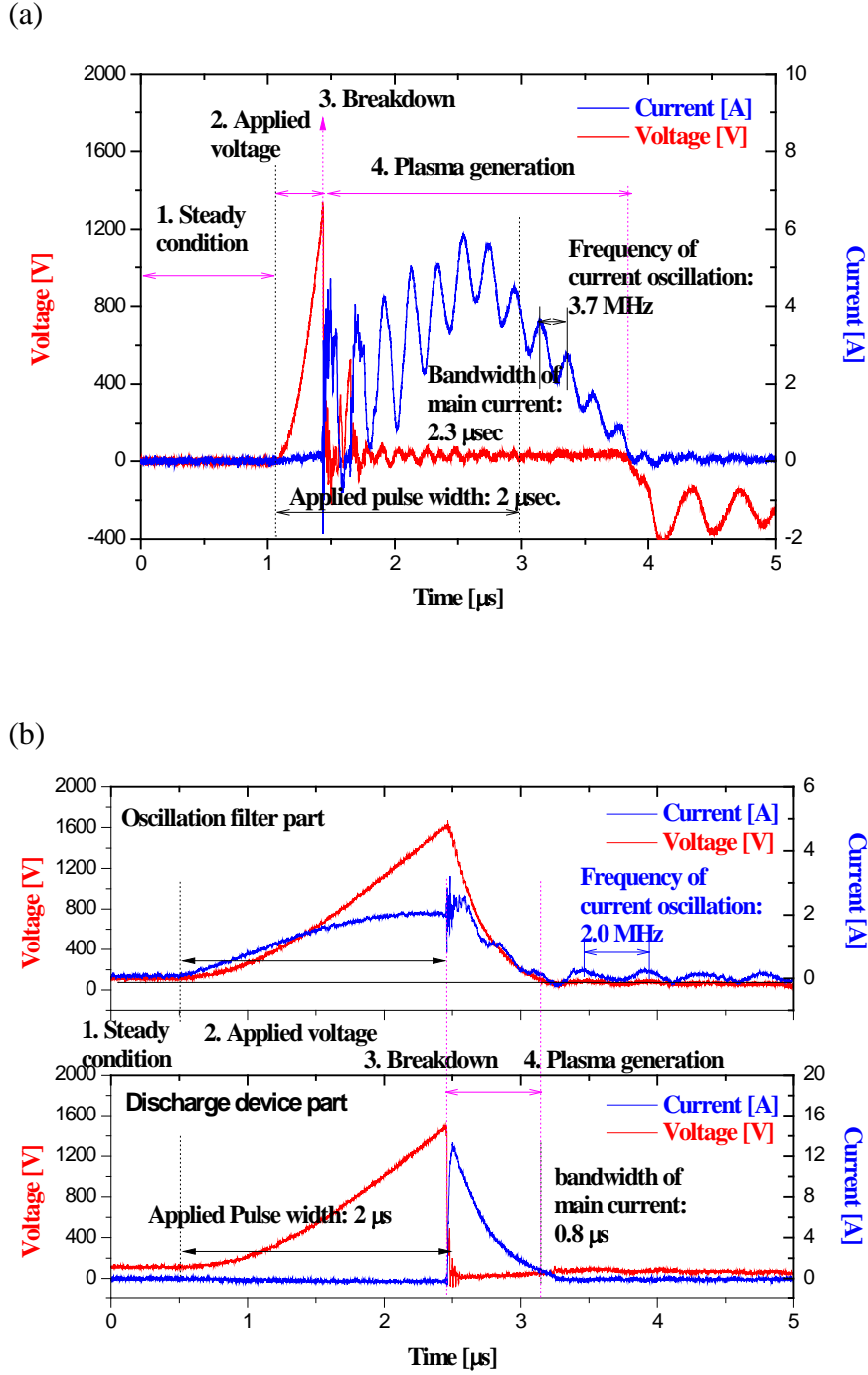
(a)

(b)

Fig. 2.4. Current-voltage waveforms of the SP discharge with (a) the conventional circuit and (b) the low pass filter circuit. In figure (b) the probe was set in point (1) and (2) corresponding to the voltage-current waveforms displayed on the top and bottom, respectively. The stages of the plasma evolution in time are indicated.

For a conventional circuit, the discharge device was connected directly to the bipolar pulsed power supply. The resistance of a conventional circuit under the steady condition region I) in Fig. 2.4(a) was measured to be 18.5Ω from the measured I-V plot. When a pulsed bipolar voltage was applied with a value of 1600V during 2 μs (within the error of 5%), the resistance of the circuit increased from 18.5Ω to 27 kΩ (region II). The pulse width of the voltage was set at 2.0 μs, but the breakdown of the discharge suddenly started within 0.5 μs and the measured resistance decreased from 27 kΩto 53mΩ (region III).

On the other hand, in the case of low-pass filter circuit, the voltage continuously increased to 1600 V for 2 μs of applied pulse width, and the average resistance value increased from 515.5 Ω to 3.7 kΩ before the breakdown (region II). After the continuous increase in voltage, that is, sufficient charge accumulation during 2 μs, a breakdown occurred and the resistance decreased from 3.7 kΩ to 108 mΩ (region III). It should be noted from Fig. 2.4 that the current shape, peak current value, and the degree of current oscillations in plasma generation stage IV were different for the conventional and low-pass filter circuits. For a conventional circuit, the overall shape of the current was similar to a regular triangle with a significant current fluctuation. The discharging current increased to a maximum value of ~6 A and the frequency of current oscillations was 3.7 MHz. These current waveforms and oscillation phenomena in Fig. 2.4 (a) are generally observed in the SP generation using the conventional circuit and pin-to-pin discharge device.[12–14,17,20–45] The current waveforms of the low-pass filter circuit in Fig. 2.4 (b) were clearly different from those of conventional circuit. The voltage waveform of the oscillation filter part perfectly matched with the calculated waveform in Fig. 2.5. The current of the oscillation filter part exhibited an oscillation frequency of 2.0 MHz with smaller amplitude, compared with the conventional circuit. The current of the discharging device part sharply increased to ~13 A and decreased with negligible fluctuations
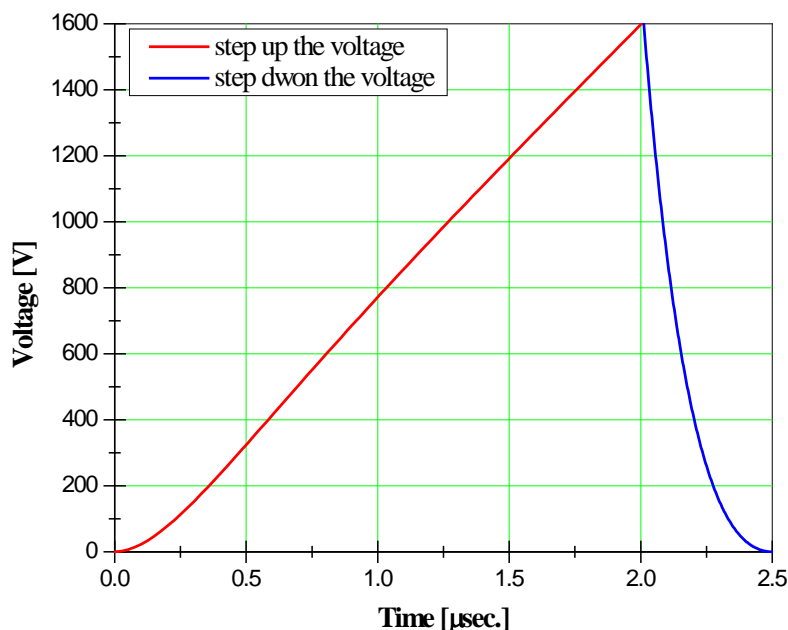
during the SP discharge.

Fig. 2.5. Calculated theoretical voltage waveform when the applied voltage was 1600V.

2.3.2 Optical properties of the solution plasma

A typical OES of the SP operating with the conventional circuit and low-pass filter circuit are shown in Fig. 2.6 (a) and (b), respectively. The excited oxygen and hydrogen atoms in plasma were identified by their dominant emission peaks detected at 777.1 nm for O, and 434.0, 486.1, and 656.3 nm for H_γ, H_β, and H_α, respectively. These active species are generated from the dissociation of water molecules, which is often observed for the SP in an aqueous solution. It was found that the intensity and stability of the OES of the excited species depended on the SP operating circuit. From 1200 times measurements of the OES, the signal intensity ratio of H_β to H_α, $I(H_\beta)/I(H_\alpha)$ for the low-pass filter circuit was determined to be 0.077 ± 0.040, which was higher than that for the conventional circuit (0.050 ± 0.200).
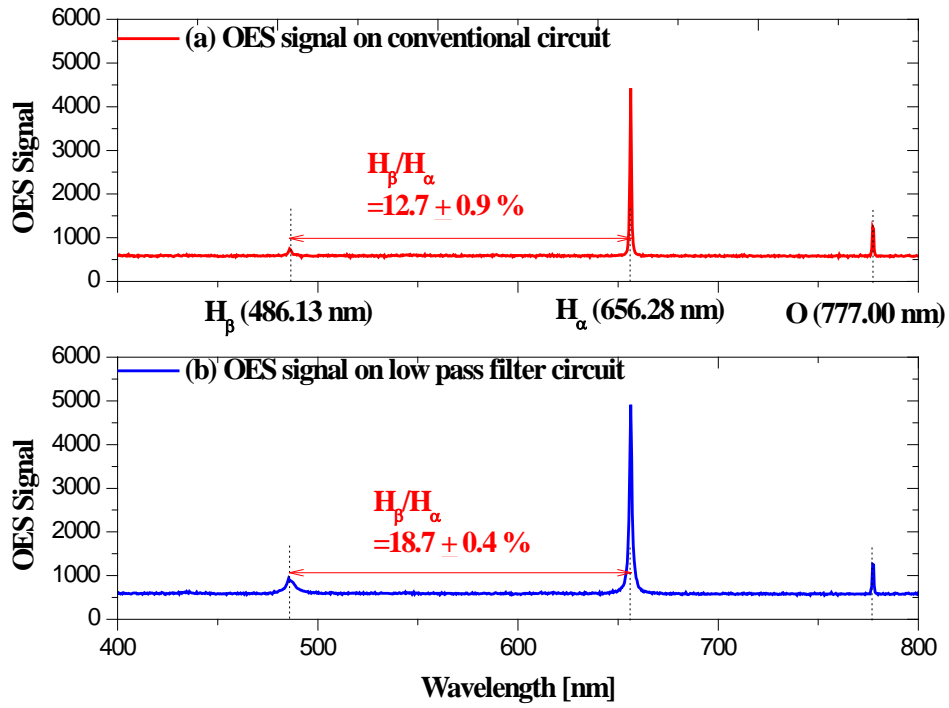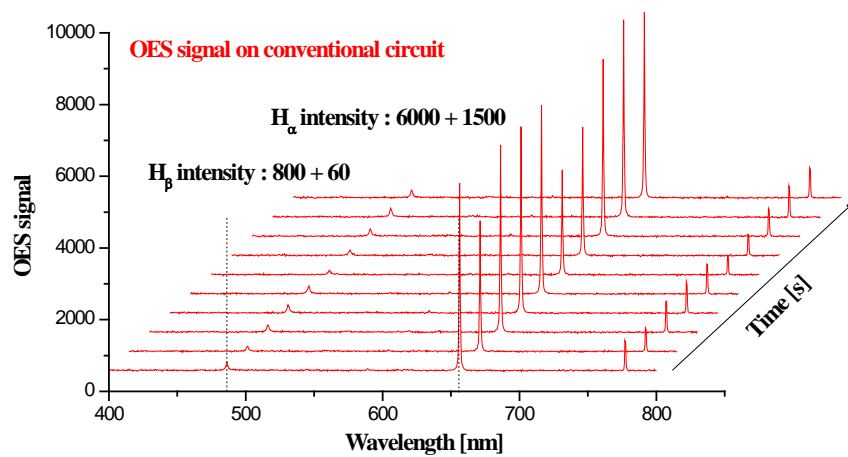
Fig 2.6. Typical optical emission spectra showing the most significant excited species in the SP: hydrogen lines H_β, H_α and oxygen in (a) SP operating with a conventional device and (b) with a low pass filter circuit.

Fig. 2.7 (a) and (b) exhibited a time behavior of the OES for the conventional circuit and the low-pass filter circuit, respectively. By using the RC component in the circuit, the intensity of H_α decreased from 4709 ± 914 to 3525 ± 104, and the intensity of H_β increased from 235 ± 44 to 272 ± 1. The increased $I(H_\beta)/I(H_\alpha)$ for the low-pass filter circuit is due to the decreased H_α and increased H_β.
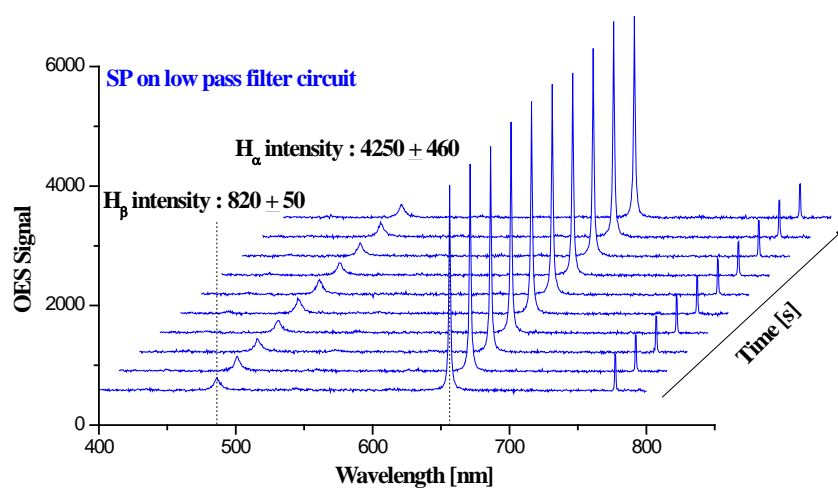
(a)

(b)

Fig. 2.7. Time behavior of the OES during 10 s of excited species for (a) a conventional circuit and (b) a low pass filter circuit.

2.3.3 Heat energy and vaporized water quantity during the SP

The solution temperature was continuously monitored during the discharge of 20 min, as presented in Fig. 2.8. The initial temperature of DI water was 290 K and the final temperature of the water after the discharge during 20 min slightly increased to 298.5 K and 297.4 K for the conventional and low-pass filter circuits, respectively. After the plasma discharge, the theoretical thermal energy E was calculated as $E = cm\Delta T$, where c, m, and ΔT are the specific heat, mass of the material, and the temperature difference between the beginning and end of the experiment, respectively. [46] The generated heat energies were calculated to be 7113 J and 6192 J for the conventional and the low-pass filter circuits, respectively. Also, quantities of 0.09 g and 0.30 g water were evaporated during a 20-min period for the conventional and low-pass filter circuits, respectively.
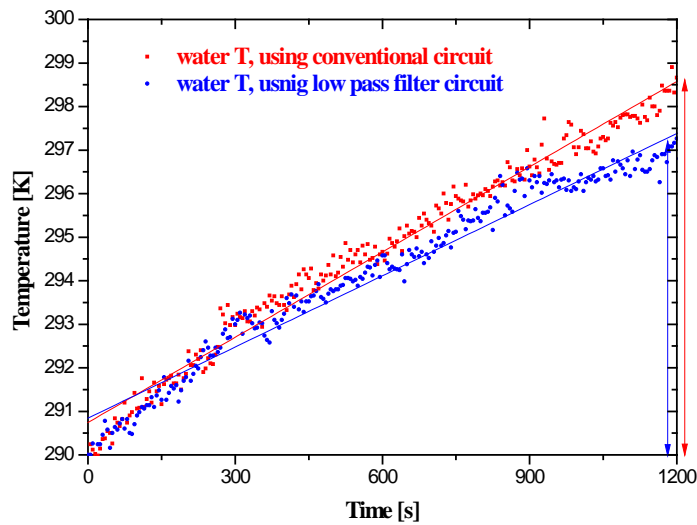

Fig. 2.8. Temperature of the solution phase (DI water) during the discharge of SP.

2.4 Discussion

Three complicatedly mixed phases are involved in the SP, namely, liquid, gas, and plasma. A description of the SP must take into account various interfaces implicated during plasma operation: Gas-liquid, gas-plasma, plasma-liquid, electrode-liquid, electrode-plasma, and gas-electrode. Bubble formation or gas generation owing to the thermal heat (Joule heating) and electrolysis can explain the breakdown in the SP.[1,2,18,19,45] The SP generation proceeds by (a) the formation of micro-bubbles or gas by electrolysis and Joule heating (stage II), (b) the breakdown in the largely grown bubbles or expanded gas phase region (stage III), and (c) the formation of a full plasma channel (stage IV) in sequence, as seen in Fig. 2.9.
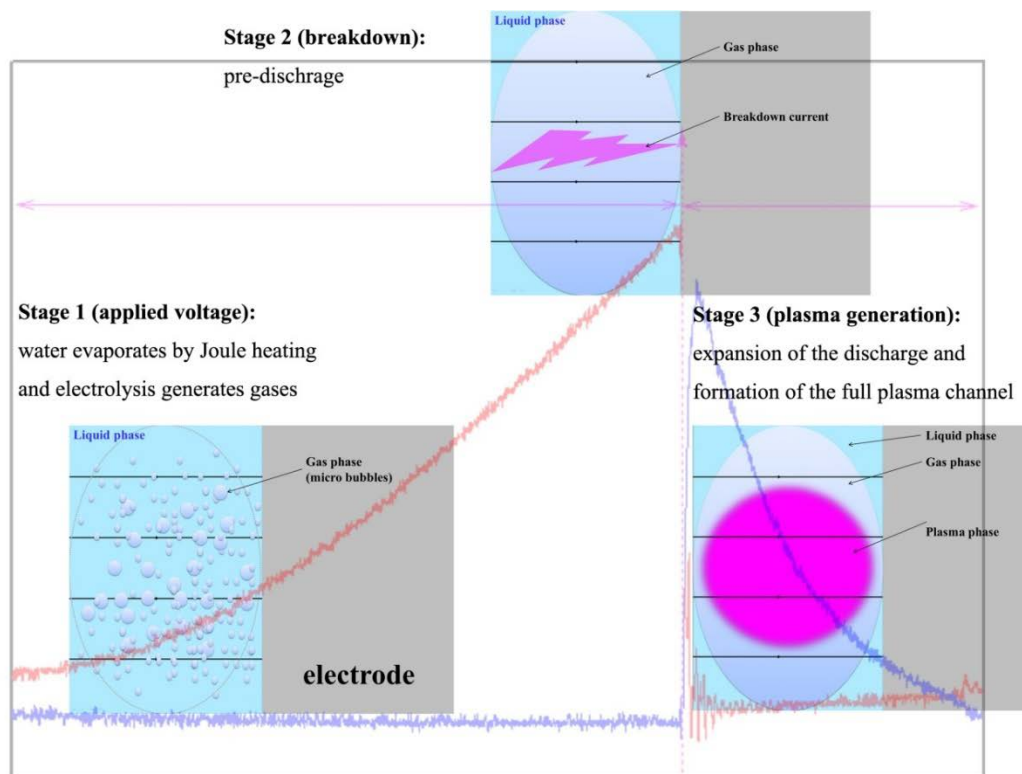

Fig. 2.9. Schematic diagram of the applied voltage, breakdown, and plasma generation stages in the SP (the background is the current and voltage waveform in the bottom of the Fig. 2.4(b)).

In stage II, micro-bubbles or gas phase are formed by the thermal heat (Joule heating) and electrolysis, and the bubbles grow bigger as the applied potential increases, which leads to the continuous increase in the resistance, as explained in the current-voltage waveforms. The breakdown occurs through the largely grown bubbles or expanded gas phase region and the current rapidly increases in stage III. A plasma channel connects the electrodes and the discharge occurs in stage IV, as confirmed by the current-voltage waveforms and optical emission spectra. One of the purposes of this research is to control the stability of the SP using external RC components in the circuit, that is, low-pass filter circuit. From the comparative analyses of discharge current variation in stage IV, it was found that the peak current increased and the oscillation frequency and amplitude of the current waveforms decreased using the low-pass filter circuit, indicating an enhanced discharge stability of the SP.
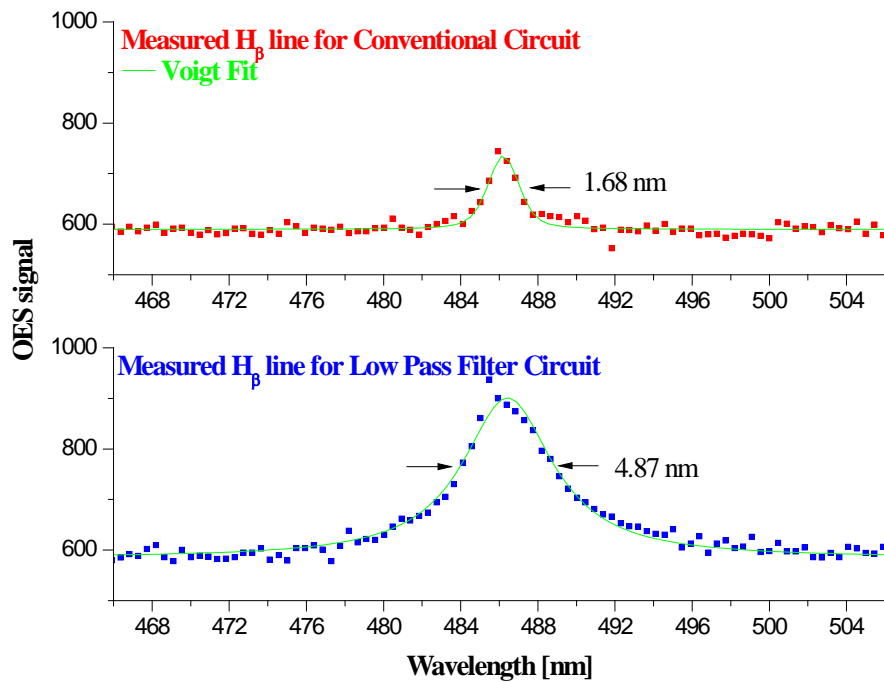

Fig. 2.10. The line shape of the hydrogen emission H_β for both circuits. The spectral line was fitted with a Voigt profile and by deconvolution the Stark broadening was extracted.

When the hydrogen mole fraction is small enough, the electron density can be estimated using Stark broadening extracted by Voigt fitting of the H_β emission line and the deconvolution of the spectral line from other effects such as van der Waals, Doppler, and resonance broadenings as shown in Fig. 2.10. [12,14,47–49] First, the natural broadening can be ignored as it is much smaller than other broadenings. The instrumental broadening was determined to be 0.7 nm. The van der Waals and Doppler broadenings were estimated to be 0.01 nm and 0.001 nm, respectively, at an atmospheric pressure of 1 atm and gas temperature of 1600 K, when water was used in the discharge.[12,14,49] The electron density is calculated using the equation below:

$$\Delta\lambda_{Stark} = 4.8 \times (n_e \times 10^{-23})^{0.68} \qquad (1)$$

where the full width at half maximum (FWHM) of H_β emission line in OES is 1.68 nm and 4.87 nm for the conventional and the low-pass filter circuits, respectively, and ne represents the electron density. The electron densities, n_e were calculated to be $2.13 \times 10^{22}/m^3$ for the conventional circuit and $1.02 \times 10^{23}/m^3$ for low-pass filter circuit. It was also confirmed by OES that the $I(H_\beta)/I(H_\alpha)$ for low-pass filter circuit was determined to be 0.077 ± 0.040, which was higher than that for the conventional circuit (0.050 ± 0.200), suggesting that the excitation of the hydrogen to high energy level was more improved using the low-pass filter circuit. The electron temperature can be determined from the relative intensities of the spectral lines of the excited hydrogen H_β to H_α, assuming a quasi-local thermodynamic equilibrium in the SP, using the following equation[50]:

$$\frac{I_1}{I_2} = \frac{A_1 g_1 \lambda_2}{A_2 g_2 \lambda_1} \exp\left\{-\frac{E_1 - E_2}{kT}\right\} \qquad (2)$$

where I, A, g, λ, E, k and T represent the emission intensity of H radicals from OES data, the transition probability or Einstein coefficient (s^{-1}), statistical weight, wavelength (m), upper

level energy (J), Boltzmann constant (1.38×10^{-23} J/K), and electron temperature (eV), respectively. The electron temperatures in the SP discharge with the conventional circuit and the external low-pass filter circuit were calculated to be 4700 ± 900 K and 6400 ± 300 K, respectively. From the above results, it is indicated that the increased electron density and electron temperature, that is, increased electron energy, was achieved using the external low-pass filter in circuit. The parameters of the SP using conventional and low-pass filter circuit were summarized in Table 2.1. It was noted from Table 2.1 that the low-pass filter circuit gave a smaller heat energy, which might be due to a lower transfer of the SP energy into the ion generation. A smaller quantity of the vaporized water for the low-pass filter circuit may be attributed to the increased electron energy and vigorous bubble formation by electrolysis.

The frequency of the current oscillations is associated with the frequency of the plasma ion or electron oscillations, which is given through the following equation [51]:

$$\omega_p[Hz] = \sqrt{\frac{4\pi n e^2}{m}} \qquad (3)$$

where ω_p, m, n, and e represent, respectively the ion plasma frequency, mass of electron or ion, density of electron or ion, and the electric charge. The electron oscillations are generally in the GHz range, whereas the ion oscillations often remain in the MHz range owing to the larger mass of the ions compared with the electrons.[51,52] When the SP operates with the low-pass filter circuit, the current oscillation frequency decreased from 3.7 to 2.0 MHz and the ion densities were calculated from Equation (3) to be $3.13 \times 1017/m^3$ and $9.20 \times 1016/m^3$ for conventional circuit and low-pass filter circuit, respectively. The distances between the ions were 1.47 and 2.22 µm in average value for the conventional circuit and low-pass filter circuit, respectively, from the calculation based on Tonks and Langmuir (1929). [51] The decreases in the frequency and amplitude of the current oscillation and the corresponding decreased ion density for the low-pass filter circuit improved the SP discharge stability. The consequently

increased density and temperature of electrons, that is, the increased electron energy of the low-pass filter circuit are favorable to generate the non-equilibrium SP condition.

Table 2.1. Parameters of the SP using conventional and low-pass filter circuits

Parameter	Conventional circuit	Low pass filter circuit
Maximum current in the SP discharge [A]	6	13
Current oscillation frequency in the SP discharge [MHz]	3.7	2.0
Electron density, n_e [/m^3]	2.13×10^{22}/m^3	1.02×10^{23}/m^3
Intensity ratio of H$_\beta$ to H$_\alpha$ in OES [-]	0.050 ± 0.200	0.077 ± 0.040
Electron temperature, T_e [K]	4700 ± 900	6400 ± 300
Temperature increase of DI water [K]	8.5	7.4
Vaporized water mass [g]	0.09	0.30
Heat energy [J]	7113	6192

2.5 Conclusion

In this study, the non-equilibrium SP condition at which the electron energy was higher than the ion energy was controlled by introducing the RC component in the plasma circuit. In the SP discharge, the maximum discharge current of the low-pass filter circuit was 13 A, which was higher than 6 A of the conventional circuit. The frequency and amplitude of the current oscillations related to the ion oscillations were decreased by means of low-pass filter circuit, leading to the enhanced SP discharge stability. From the analyses of OES, it was found that the low-pass filter circuit provided a higher electron density and temperature (i.e., higher electron energy) compared with the conventional circuit. The modified SP circuit increasing the electron energy will provide an effective way to synthesize metastable materials formed under the non-equilibrium condition.

REFERENCES

[1] W. G. Graham, K. R. Stalder, J Phys D: Appl Phys 2011, 44, 174037.

[2] Y. Yang, Y. I. Cho, A. Fridman, Plasma Discharge in Liquid: Water Treatment and Applications. CRC press, New York 2011.

[3] D. Bera, S. C. Kuriy, M. McCutchen, S. Seal, H. Heinrich, G. C. Slane, J Appl Phys 2004, 96, 5152.

[4] P. Wu, J. H. Sun, Y. Y. Huang, G. F. Gu, D. G. Tong, Mater Lett 2012, 82, 191.

[5] B. Sun, M.Sato, J. C. Clements, J PhysD:ApplPhys 1999, 32, 1908.

[6] P. Lukes, M. Clupek, V. Babicky, E. Spectlikova, I. Sisrova, E.Marsalkova, B. Marsalek, Plasma Chem Plasma P 2013, 33, 83.

[7] P. Lubicki, S. Jayaram, Bioelectrochem Bioenerg 1997, 43, 135.

[8] K. H. Schoenbach, R. P. Joshi, R. H. Stark, IEEE Trans Dielectr Electr Insul 2000, 7, 637.

[9] J. Wilsing, Astrophys J 1899, 10, 113.

[10] S. N. Lockyer, Astrophys J 1902, 15, 190.

[11] C. Tendero, C. Tixier, P. Tristant, J. Desmaison, P. Leprince, Spectrochim Acta B 2006, 61, 2.

[12] M. A. Bratescu, S. P. Cho, O. Takai, N. Saito, J Phys Chem C 2011, 115, 24569.

[13] Y. K. Heo, S. Y. Lee, Met Mater Int 2011, 17, 431.

[14] Y. K. Heo, M. A. Bratescu, T. Ueno, N. Saito, J Appl Phys 2014, 116, 024302.

[15] H. S. Lee, M. A. Bratescu, T. Ueno, N. Saito, RSC Adv 2014, 4, 51758.

[16] S. M. Kim, Y. K. Heo, K. T. Bae, Y. T. Oh, M. H. Lee, S. Y. Lee, Carbon 2016, 101, 420.

[17] I. V. Lisitsyn, H. Nomiyama, S. Katsuki, H. Akiyama, IEEE Trans Dielectr Electr Insul 1999, 6, 351.

[18] S. Katsuki, H. Akiyama, A. A. Ghazala, K. H. Schoenbach, IEEE Trans Dielectr Electr Insul 2002, 9, 498.

[19] C. Miron, M. A. Bratescu, N. Saito, O. Takai, J Appl Phys 2011, 109, 123301.

[20] O. Takai, Pure Appl Chem 2008, 80, 2003.

[21] T. Takeda, J. S. Chang, T. Ishizaki, N. Saito, O. Takai, IEEE Trans Plasma Sci 2008, 36, 115.

[22] J. Hieda, N. Saito, O. Takai, Surf Coat Tech 2008, 2002, 5343.

[23] J. Hieda, T. Shirafuji, Y. Noguchi, N. Saito, O. Takai, J Jpn I Met 2009, 73, 738.

[24] Y. Ichin, K. Mitamura, N. Saito, O. Takai, J Vac Sci Technol A 2009, 27, 826.

[25] N. Saito, J. Hieda, O. Takai, Thin Solid Films 2009, 518, 912.

[26] P. Pootawang, N. Saito, O. Takai, Jpn J Appl Phys 2010, 49, 126202.

[27] S. P. Cho, M. A. Bratescu, N. Saito, O. Takai, Nanotechnology 2011, 22, 455701.

[28] X. Hu, S. P.Cho,O. Takai,N. Saito, CrystGrowthDes 2011, 12, 119.

[29] I. Prasertsung, S. Damrongsakkul, C. Terashima, N. Saito, O. Takai, Carbohydr Polym 2012, 87, 2745.

[30] P. Pootawang, N. Saito, O. Takai, S. Y. Lee, Nanotechnology 2012, 23, 395602.

[31] P. Pootawang, N. Saito, O. Takai, S. Y. Lee, Mater Res Bull 2012, 47, 2726.

[32] J. Kang, O. L. Li, N. Saito, Nanoscale 2013, 5, 6874.

[33] O. L. Li, J. Kang, K. Urashima, N. Saito, Int J Plasma Environ Sci Technol 2013, 7, 31.

[34] P. Pootawang, N. Saito, S. Y. Lee, Nanotechnology 2013, 24, 055604.

[35] X. Hu, X. Shen, O. Takai, N. Saito, J Alloy Compd 2013, 552, 351.

[36] A. Watthanaphanit, N. Saito, Polym Degrad Stab 2013, 98, 1072.

[37] M. A. Bratescu, O. Takai, N. Saito, J Alloy Compd 2013, 562, 74.

[38] J. Kang, O. L. Li, N. Saito, Carbon 2013, 60, 292.

[39] I. Prasertsung, S. Damrongsakkul, N. Saito, Polym Degrad Stab 2013, 98, 2089.

[40] A. Watthanaphanit, G. Panomsuwan, N. Saito, RSC Adv 2014, 4,1622.

[41] G. Panomsuwan, S. Chiba, Y. Kaneko, N. Saito, T. Ishizaki, J Mater Chem A 2014, 2, 18677.

[42] D. Kim, O. L. Li, P. Pootawang, N. Saito, RSC Adv 2014, 4, 16813.

[43] A. Watthanaphanit, Y. K. Heo, N. Saito, J Taiwan Inst Chem Eng 2014, 45, 3099.

[44] T. Sudare, T. Ueno, A. Watthanaphanit, N. Saito, Phys Chem Chem Phys 2014, 17, 30255.

[45] H. Akiyama, IEEE Trans Dielectr Electr Insul 2000, 7, 646.

[46] F. P. Incropera, D. P. DeWitt, T. L. Bergman, A. S. Lavine, Fundamentals of Heat and Mass Transfer, 6th ed., John Wiley and Sons Inc, New Jersey 2007.

[47] C. O. Laux, T. G. Spence, C. H. Kruger, R. N. Zare, Plasma Sources Sci Technol 2003, 12, 125.

[48] W. Demtröder, Laser Spectroscopy, 4th ed., Springer, Berlin 2008.

[49] P. Bruggeman, D. Schram, M. Å. Gonzalez, R. Rego, M. G. Kong, C. Leys, Plasma Sources Sci Technol 2009, 18, 025017.

[50] W. Lochte-Holtgreven, Plasma Diagnostics. American Institute of Physics, New York 1998.

[51] L. Tonks, I. Langmuir, Phys Rev 1929, 33, 195.

[52] M. A. Lieberman, A. J. Lichtenberg, Principles of Plasma Discharges and Materials Processing, 2nd ed., John Wiley and Sons Inc, New Jersey 2005.

Chapter 3
Enhancement of Nitrogen Self-Doped Nanocarbons Electrocatalyst Activity via Tune-up Solution Plasma

Chapter 3 Enhancement of Nitrogen Self-Doped Nanocarbons Electrocatalyst Activity via Tune-up Solution Plasma
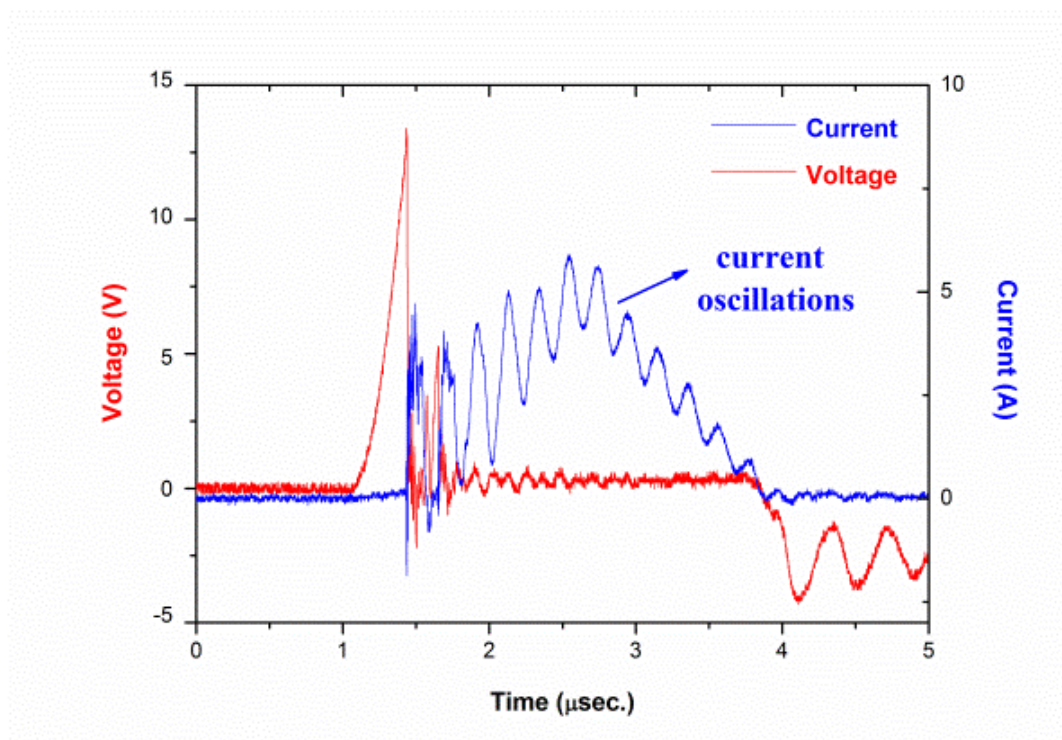
3.1 Introduction

Efficient electrocatalyst for the oxygen reduction reaction (ORR) have attracted widespread attention to accomplish optimal performance for application in energy storage and conversion devices, such as fuel cell (FC) and metal-air batteries (MABs). [1-4] However, the catalysts on the cathode suffer from several critical obstacles, and the possible commercialization of FC and MABs is difficult due to the inherent sluggish kinetics and high overpotential in the ORR. Currently, platinum (Pt) and platinum supported on carbon materials (Pt/C) are regarded as the best issues to solve these problems because of a four-electron reduction pathway in ORR process but, prohibitive cost, low reserves, and methanol tolerance interrupt the development of the large-scale commercialization. [1, 5-7] In this regard, ongoing research efforts have been devoted searching to replace Pt with Pt-free catalyst with highly efficient performance, selectivity, and durability, such as non-precious metal supported on nanocarbons, [3, 8, 9] or metal-free heterogeneous nanocarbons. [3, 7, 10, 11] Among them, the metal-free heterogeneous nanocarbons have been regarded as one of the most prominent alternatives for the ORR electrocatalyst when they incorporate heteroatoms (e.g. N, B, P, S, and I) into the carbonaceous skeleton.[12-20] In particular, N-functionalized nanocarbons represent the most investigated catalyst for an efficient ORR activity, because of their comparable catalytic efficiency, low cost, and stability in an alkaline medium. [7, 11] In detail, N-functionalized nanocarbons can play a crucial role in the ORR by imparting higher positive

charge density on neighboring carbon atoms and facilitating the dissociation of O-O bond on the neighboring C atoms. [7, 12, 15, 21, 22-27]

A two-dimensional (2D) carbon nanosheet, which is a few to multi-layers sheet, exhibits intrinsic characteristics such as large surface area, excellent electrical conductivity, and high mechanical/chemical stability. 28, 29 Moreover, a number of catalytic sites with an efficient pathway for the ORR can be created by the planar structure of a 2D carbon nanosheet. Particularly, carbon nanosheets containing heteroatoms, especially nitrogen, have been demonstrated to effectively improve the ORR activity in the alkaline electrolyte using practical experiments and theoretical calculations. [12, 15, 22, 25, 30-34] However, the synthesis procedure and condition are relatively complicated and strict, resulting in a high fabrication cost.

Solution Plasma (SP), a non-equilibrium discharge in liquids at atmospheric pressure and room temperature, has emerged as a useful synthetic method for various nanomaterial such as nanoparticles, [35-37] nanocarbons, [38] heterogeneous nanocarbons, [39-40] and transition metal-carbon composites.[41] Among these nanomaterials, the most interesting achievement is the formation of heterogeneous nanocarbons. SP synthesis approach has not only provided new insight into the fabrication and design of nanocarbons but was also further extended to a series of heteroatom doping simply by selecting the organic precursors containing the desired heteroatoms. [41] However, the conventional SP synthesis is still at a beginning stage in the field of carbon fabrication and, especially, difficult to control the morphology, structure, and bonding configuration between carbon and the doped heteroatoms. To overcome these limitations, we have developed the tune-up SP system which is composed of a low-pass filter circuit to improve the discharge stability by controlling the current oscillations (Fig. 3.1). [42]
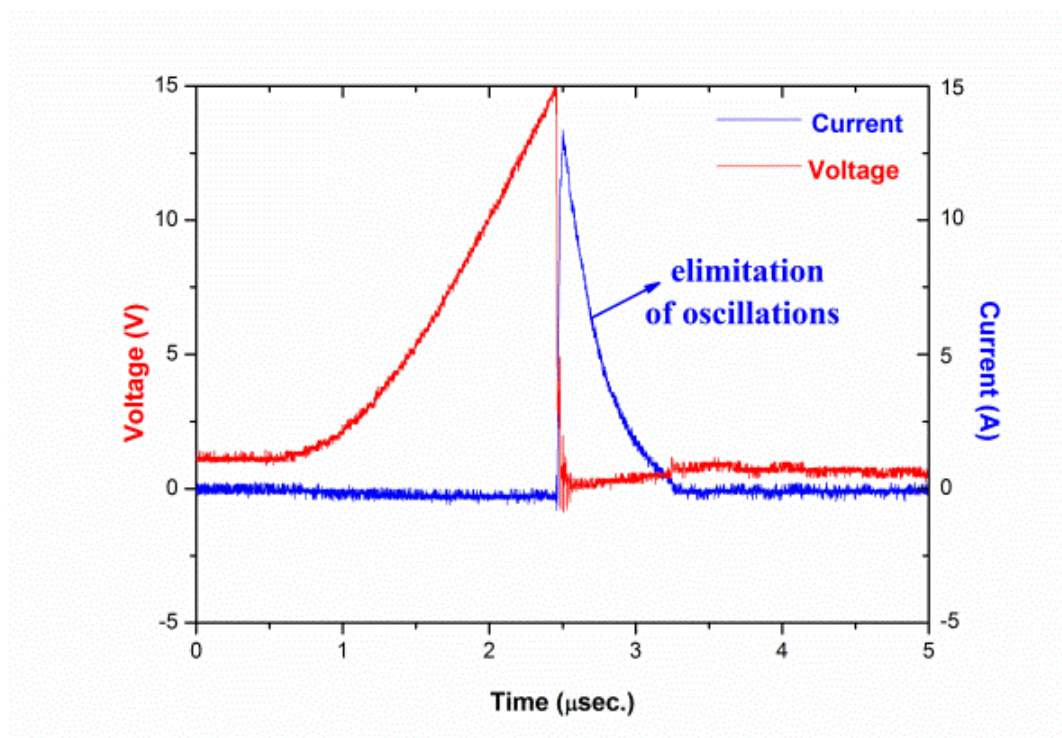
(a)

(b)

Fig. 3.1 Current-voltage waveforms of SP discharge with (a) conventional, and (b) tune-up SP.

The voltage and the current waveforms of the plasma in pyridine. The current oscillations were

successfully eliminated after tune-up SP.

Herein, we have proposed a new synthetic approach of nitrogen self-doped nanocarbons by the tune-up SP system. Notably, our synthesis strategy has the advantage to produce milligrams of material within ten minutes without any pre or post treatment, which is a one-step process, as compare to other processes.[7, 1, 16, 25] The nitrogen doped graphitic carbon nanosheets (NGS) was synthesized by this new tune-up SP approach and the nitrogen doped amorphous carbon nanoparticles (NAP) by the conventional SP. As-prepared NGS exhibits a graphitic structure with high surface area and mesoporous structure, as well as an ORR activity that as comparable with that of the commercial Pt/C in alkaline media, and shows an excellent stability.

3.2 Experimental section

3.2.1 Materials

Tungsten electrode (Φ 0.8 mm, 99.9% purity) was obtained from Nilaco Corporation. Pyridine (C_5H_6N, ≥99.5% purity), ethanol (C_2H_5OH, ≥99.5% purity) and 0.1M potassium hydroxide aqueous solution (0.1 M KOH, ≥99.5% purity) were purchased from Kanto Chemical Co., Inc. Nafion® DE 521 solution (5 wt% in a mixture of lower aliphatic alcohols and water), and 20 wt % Pt on Vulcan XC-72 (20% Pt/C) were purchased from Sigma-Aldrich. Ultrapure water (18.2 MΩ cm-1 at 25 °C) was provided from Advantec RFD 250NB system. All chemicals were of analytical grade and used without further purification.

3.2.2 Synthesis of NGS and NAP

To generate the plasma in pyridine for the synthesis of NGS, a tune-up SP system was setup, as shown in Fig. 3.2. The synthesized nanocarbons using the conventional SP system was denoted as NAP. Two tungsten electrodes shielded with an insulating ceramic tube were fixed at the center of a Teflon® reactor with a gap distance of 1.0 mm. The plasma was

generated between these electrodes using a bipolar pulsed power supply (MPS - R06K01C - WP1 - 6CH, Kurita) used in two cases with or without the low-pass filter circuit made in our laboratory. The low-pass filter circuit consists a parallel capacitor of 2 nF, a variable resistor series from 50 to 150 Ω, and a variable inductor set at 100 µH to adjust the plasma stability. Using the tune-up SP system, the stability of plasma was considerably improved by eliminating the energy fluctuations which determine the structure of the synthesized nanocarbons. Fig. 3.1 shows the characterization of plasma by the electrical energy according to the current-voltage (I-V) curve. The optimum pulse duration and pulse repetition frequency were 0.5 µs and 30 kHz, respectively. To observe the electrical properties of the solution plasma (SP), the current-voltage (I-V) waveforms were measured using oscilloscope (DLM 2024, Yokogawa) with a current probe (PBC 50 and PBC 100, 50 and 100 MHz, respectively, Yokogawa) and a differential high-voltage probe (PBDH 0150, 150 MHz, Yokogawa). Also, to analyze the optical properties of SP, the optical emission spectrum (OES) during discharge was recorded by a spectrograph (USB 4000, Ocean Optics) with an integration time of 100 ms. The optical fiber (P400-2-UV/VIS, Ocean) was fixed in a quartz tube above the discharge. The discharge was generated in a volume of 200 ml pyridine under stirring. After discharging for 30 min., the obtained black powder material was separated from the unreactive pyridine using a membrane filter paper (0.1 µm, PTFE) using a suction pump equipment, and washed several times with ethanol until the remaining solvent after washing was colorless. The acquired nanocarbon material was dried at 60 °C in an oven for 12 h.
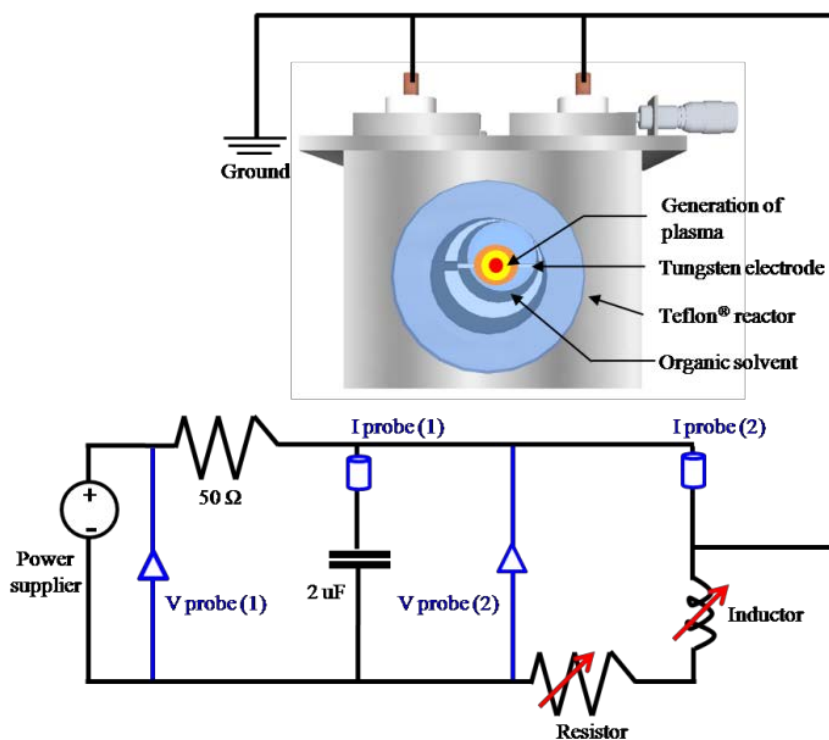
Fig. 3.2 Schematic setup of the tune-up SP system with the low pass filter circuit for NGS synthesis. The tune-up SP system consists of a low-pass filter circuit with a parallel capacitor of 2 nF, a variable resistor series from 50 to 150 Ω, and a variable inductor set at 100 μH to adjust the plasma stability.

3.2.3 Characterization

Transmission Electron Microscopy, Selected Area Electron Diffraction, and Electron Dispersive Spectroscopy (TEM, SAED, and EDS, JEOL JEM-2500SE at 200 kV) observations were conducted for the study the microstructure, shape and size, and the elemental composition of the synthesized nanocarbon material. The image obtained from Nanoscope IIIa Multimode Atomic Force Microscopy (AFM, Veeco) was used to measure the thickness of the NGS sample prepared by dropping the dispersed nanocarbon material in ethanol on a Si/SiO2 substrate. The X-ray diffraction (XRD) patterns of all samples were performed using Cu Kα (0.154 nm) X-rays source in the range from 15˚ to 60˚ with 0.02˚ step and 2˚ min^{-1} scan speed. Raman spectra were recorded with a Raman spectrometer (JASCO NRS-100) equipped with a laser with the wavelength of 532.5 nm. Nitrogen adsorption-desorption isotherms were measured on Belsorp-mini II sorption analyzer (MicrotracBEL Corp.) to investigate the specific surface area, pore volume, and pore size distribution of all samples. The specific surface area was measured by the Brunauer-Emmett-Teller (BET) method at the relative pressure between 0.05 and 0.30 and liquid nitrogen temperature. The pore volume and pore size distribution were determined by the Barrett-Joyner-Halenda (BJH) method. The chemical bond structures were examined by the X-ray photoelectron spectroscopy (XPS, Ulvac-PHI 5000 versaprobe II) using Al Kα radiation (1486.6 eV) as an X-rays source. The emission current and the anode voltage of the source were set at 0.1 mA and 15 kV, respectively. The binding energy (BE) was calibrated by using the containment carbon (C 1s= 284.5 eV). Each binding energy was referred from NIST XPS Database.[43] The elemental analysis (EA) of C, H, and N was performed using elemental analyzer (Perkin Elmer 2400 Series). The electrical conductivity was measured with a device based on a four probes method with a resistivity meter (2001 multimeter, TFT Corp., Keithley Instruments) and DC constant power supply (model

692A, Metronix Corp.). The samples were inserted into a Teflon cylinder with 0.5 cm diameter. The prepared samples were compressed with 0.6 MPa between two brass electrodes.

3.2.4 Electrochemical characterization

The electrochemical measurements were carried out on an HZ-5000 electrochemical analyzer ((Hokudo Denko Inc.) equipped with a rotating disk electrode (RDE). A Pt wire and Ag/AgCl electrode filled with saturated KCl solution were used as the counter and reference electrode, respectively. All the samples for the electrochemical measurements were coated on the glassy carbon (GC) electrode with 3 mm diameter and prepared as follows: 50 µL Nafion solution was added to 0.5 mL ethanol, and then 5 mg of finely ground catalyst was dispersed in the as-prepared solution by at least 30 min sonication to form a homogeneous suspension. Then a volume of 5µL from the suspension was loaded onto the GC electrode and dried at room temperature. Before measurements, N_2 or O_2 gasses were purged into 0.1 M KOH electrolyte at least 1 hour. Cyclic voltammetry (CV) was conducted at a scan rate of 50 mVs^{-1} from -1.0 to 0.3 V (vs. Ag/AgCl). Linear sweep voltammetry (LSV) was performed with a scan rate of 10 mVs-1 from -1.0 to 0.3 V (vs. Ag/AgCl). The rotation speed was varied from 100 to 3600 rpm. The commercial 20% Pt/C was selected as the performance benchmark. The electrochemical stability was measured by the chronoamperometric response in 0.1 M KOH saturated with oxygen during 10000 s at -0.4 V. All the polarization curves were corrected for the background currents, which were determined in the N_2-saturated electrolyte.

3.3 Results

The morphological structure of NGS and NAP were investigated by TEM. As shown in Fig. 3.3 (a), NGS shows typical sheet-like morphology. The corresponding SAED pattern shown in the inset from Fig. 3.3 (a) reveals well-defined diffraction spots which mean that the NGS is crystallized. The HR-TEM image further indicates that the NGS is composed of multi-layer graphitic nanosheets as shown in Fig. 3.3 (b). The well-contoured edges originated from the graphitic layer with the d space of the 002 crystal plane of approximately 0.350 nm clearly appear, which is closer to that of the single-crystal graphite with d = 0.335 nm. [44, 45]

The phase identification of the samples was performed by XRD as shown in Fig. 3.4. The NGS presents two prominent peaks, near $2\theta \approx 25.4°$ and $42.9°$ which indicate 002 and 100/101 diffraction planes of graphite, respectively. Using Bragg's law, the interlayer distance of NGS was calculated approximately to be 0.351 nm from the 002 diffraction peak, which is slightly larger than that of the single-crystal graphite 0.335 nm. This result agrees with TEM results as well. The AFM image in Fig. 3.5 demonstrates that the thickness of most NGS samples is 2.97 ±0.94 nm, corresponding to 10 layers according to the theoretical thickness a single-layer graphene (0.34 nm). The EDS mapping images of NGS correspond to the elemental composition (Fig. 3.3 (c)). Carbon and nitrogen atoms are distributed throughout the carbon frame indicating a homogenous incorporation of nitrogen into the graphitic carbon nanosheets. Water impurity in pyridine and the slight oxidation while drying the samples might explain the presence of oxygen in the composition of the synthesized materials.

In contrast, NAP samples reveal the formation of aggregates of small carbon particles with a diameter of approximately 10-30 nm as shown in Fig. 3.6 (a). The corresponding SAED pattern (the inset from Fig. 3.6 (a)) presents a bright center and diffuse ring pattern without any diffraction spots, confirming its amorphous nature. [46, 47] The major two peaks in XRD

pattern are also broad, which means amorphous and disordered carbon. From these results, we can conclude that NAP synthesized by conventional SP is an amorphous form of carbon nanoparticles in accordance with many other works. [38-40]
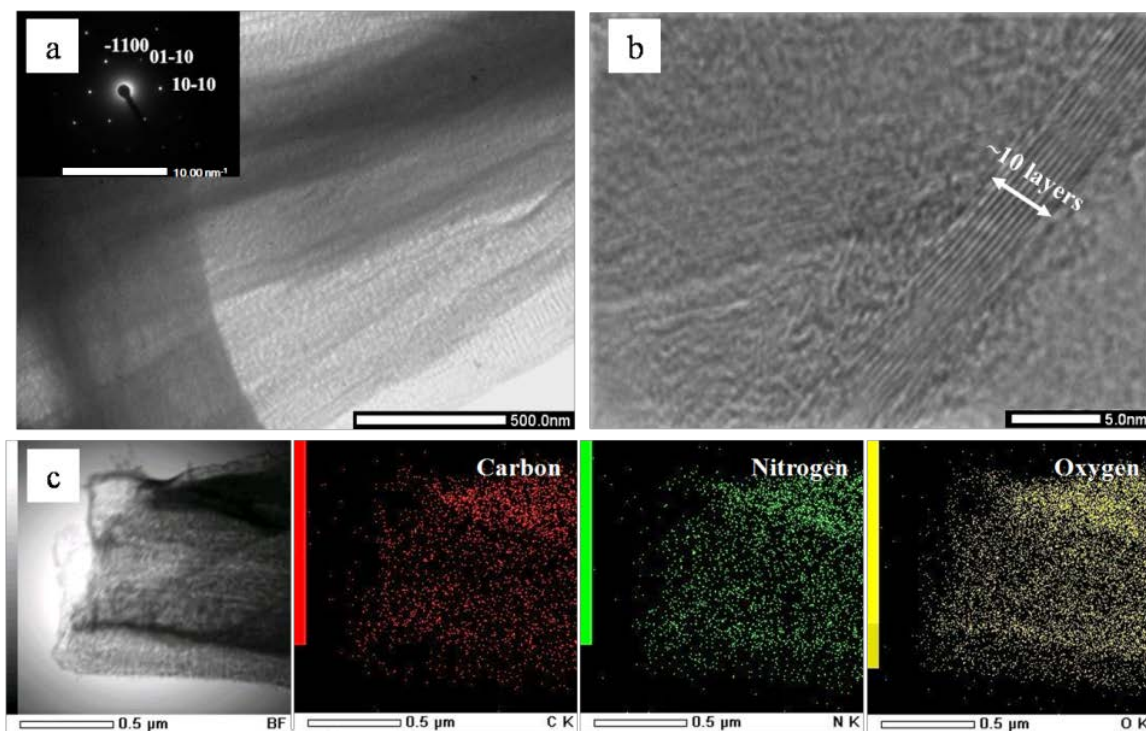

Fig. 3.3 (a) Wide-field TEM images of NGS; the corresponding SAED pattern (inset) shows well-defined diffraction spots which mean that the NGS is crystallized. (b) HR-TEM image of NGS indicates well-contoured edges originated from the graphitic layer with the *d* space of 0.350 nm. (c) Dark-field TEM image of NGS, and the corresponding carbon, nitrogen, and oxygen element mapping images.
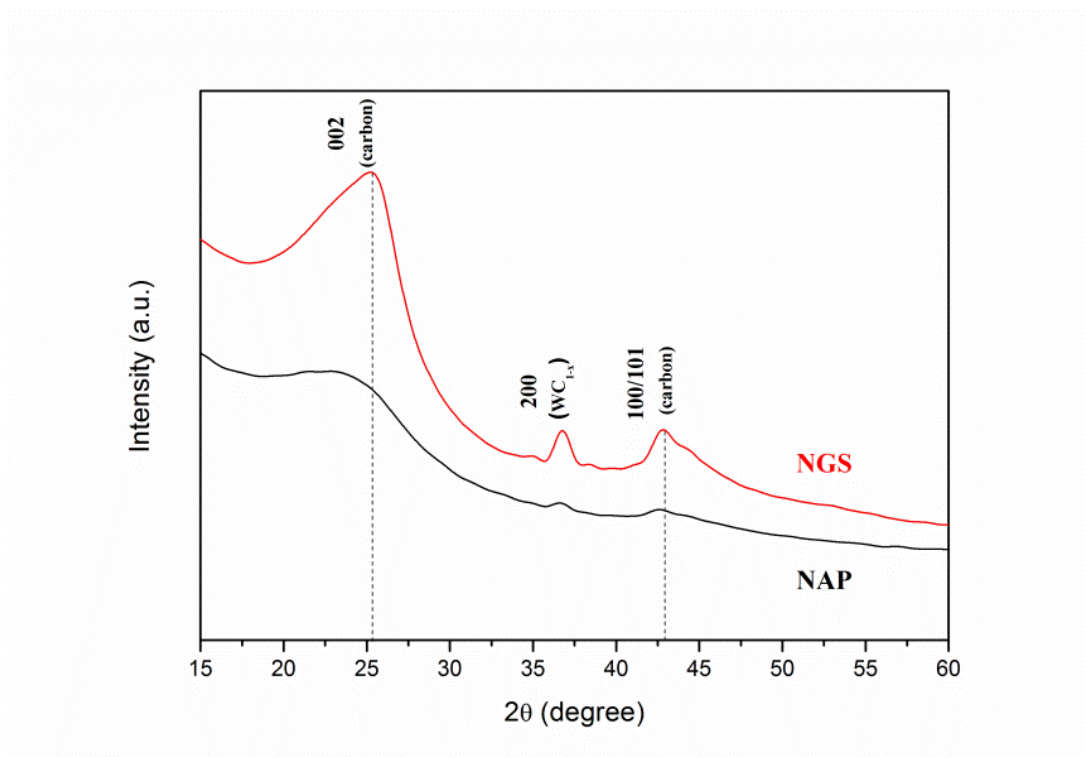
Fig. 3.4 X-ray diffraction (XRD) patterns of NGS and NAP. Using Bragg's law, the interlayer distance of NGS was calculated approximately to be 0.351 nm from the 002 diffraction peak, which is slightly larger than 0.335 nm of the single-crystal graphite.
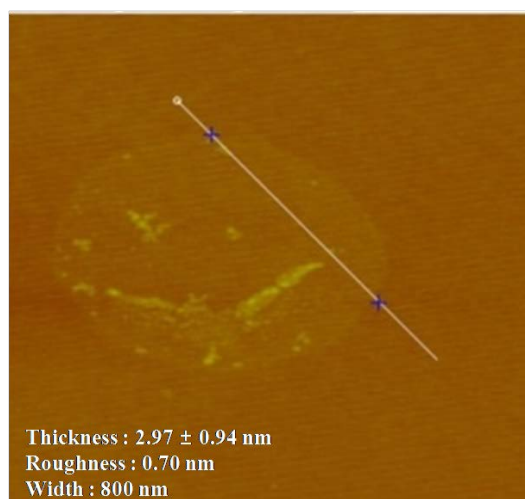

Fig. 3.5 AFM image of nitrogen doped graphitic carbon nanosheets (NGS
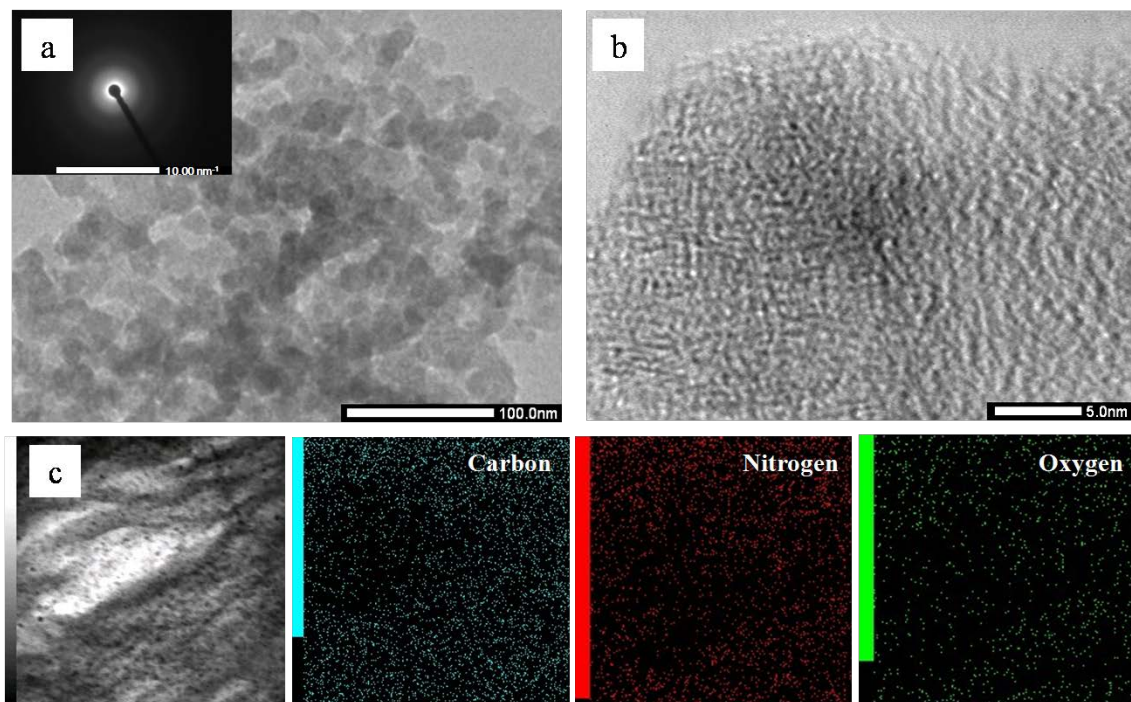
51

Fig. 3.6 (a) Wide-field TEM images of NAP; the corresponding SAED pattern (inset) shows a broad ring-like pattern without any diffraction spots, suggesting the amorphous phase. (b) HR-TEM images of NAP. (c) Dark-field TEM image of NAP, and the corresponding carbon, nitrogen, and oxygen element mapping images.

Raman spectroscopy conducted the further structural investigation. Both Raman spectra of NGS and NAP show two bands, at approximately ~1595 cm^{-1} for the G band and ~1349 cm^{-1} for D band, as shown in Fig. 3.7. The G band is attributed to one of the two E_{2g} modes of the stretching vibrations in the sp^2 domains of perfect graphite. The D band refers to the disorder and imperfection of sp^2 hybridized carbon. [48, 49] The second-order D band (2D) at ~2712 cm^{-1} is the typical feature of graphitic carbon.[50] The integrated intensities ratio between the G band to D band (I_G/I_D) linearly depends on the crystallite size(L_a) of nanocarbons, which was calculated from the equation: $L_a(nm) = (2.4 \times 10\text{-}10)\lambda_l^4(I_D/I_G)^{-1}$, where λ_l is the laser wavelength in nanometer units. [51] The I_G/I_D of NGS is 1.05 which is much higher than that of the value

of NAP (0.55), so that the crystallite size of NGS (95.9 nm) is bigger than that of NAP (50.6 nm), implying that the carbon nanosheets have long-range order and a high degree of graphitization. This result is correlated with the SAED above and HR-TEM data that NGS has graphitic structure while NAP contains amorphous carbon structure. In the Raman spectrum of NGS, the intensity of D band is still high as compared with few layers of graphene, which means that NGS has more defect sites which can influence on the electrocatalytic activity for ORR because of the enhanced charge density on carbon atoms.

Specific surface area (SSA) and porosity which are necessary for understanding the ORR activity, were investigated by N_2 sorption analysis. The BET surface area of NAP was measured to be 48 m^2g^{-1}. The BET surface area of NGS synthesized using the tune-up SP system, greatly increased and reached up to 621 m^2g^{-1}, as shown in Fig. 3.8. All samples exhibit the type IV adsorption/desorption isotherm with a hysteresis loop at the relative pressure ranging from 0.4 to 0.9, suggesting the characteristic of a mesoporous structure. [52-54] The corresponding pore size distributions of all samples derived by the BJH method indicate a broad distribution on the meso-macro length scales (the inset from Fig. 3.8). The average pore diameters and total pore volumes of all samples determined by the BJH method are listed in Table 3.1. The high specific surface area and total pore volume of NGS than those of NAP provide a significant potential of active sites and channels for electrocatalytic reactions. [30, 11, 55]
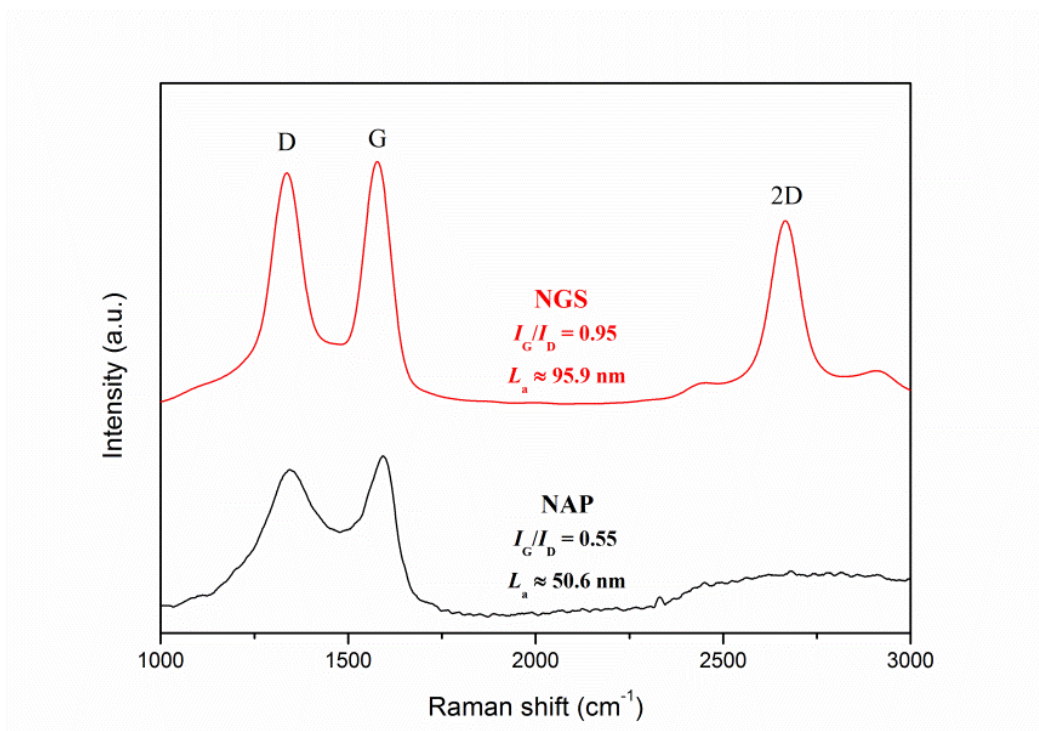
Fig. 3.7 Raman spectra with the corresponding I_D/I_G ratios of NGS and NAP. The I_D/I_G of NGS is about 0.95 which is much lower than that of the value of NAP (1.8). This result is correlated with the SAED above and HR-TEM data that NGS has a high degree of graphitization while NAP contains amorphous carbon structure.

Table 3.1 Textural parameters derived from the N_2 adsorption-desorption isotherms of NAG and NAP.

Samples	Shape	Surface area (m²/g)	Pore volume (cm³/g)	Mean pore diameter (nm)
NGS	Sheet-like	621.48	1.54	4.96
NAP	Sphere-like	48.09	0.12	10.24

Although the active sites for ORR on nitrogen-doped carbon materials are still an open question, there is no doubt that the nitrogen containing functional groups facilitate the electron to enhance ORR kinetics in a carbon matrix. [12-15, 22, 27] XPS measurements were used to demonstrate the ORR activity in dependence with the bonding configuration of nitrogen in the nanocarbon structure. The incorporation of nitrogen atoms in carbon structure was confirmed by XPS and EA measurements. The survey XPS spectra of the NGS and NAP clearly show a peak at 400.0 eV for N 1s in addition to the dominant graphitic C 1s peak at 284.5 eV, which indicate the presence of nitrogen into the carbon structure as shown in Fig 3.9.
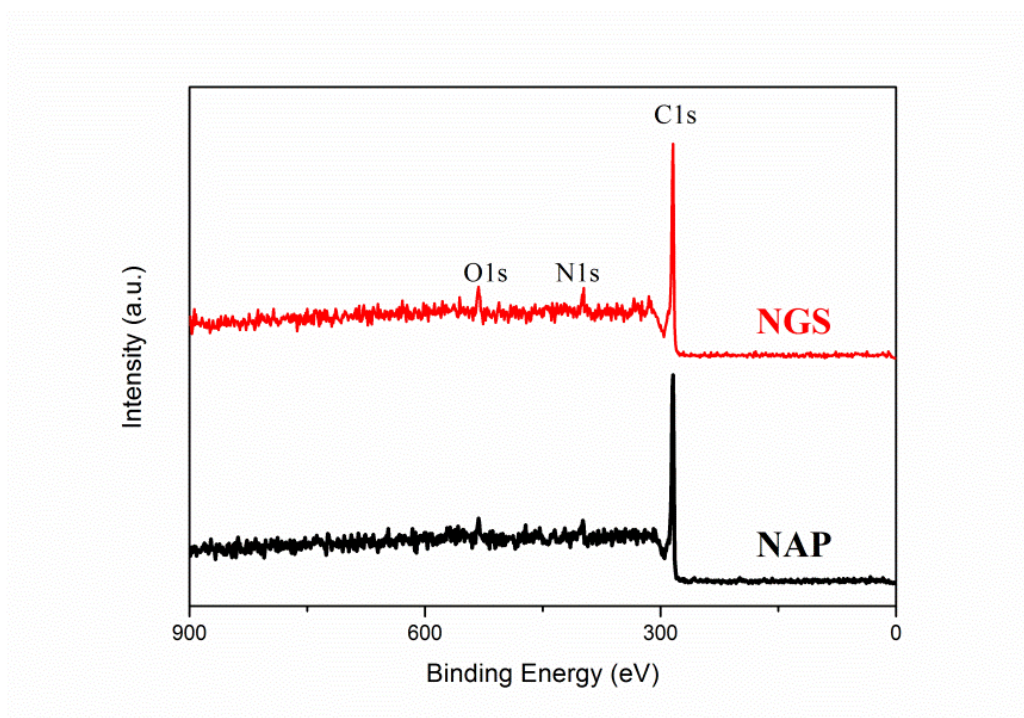

Fig. 3.9 XPS spectra of NGS and NAP. The XPS spectra of all samples shows the major peaks corresponding to C 1s, N 1s and O 1s, while a significant peak from tungsten was not detected during any measurements. This suggests that the erosion of tungsten electrode during SP discharge is negligible. In addition, the spectra show the presence of very small amount of surface adsorbed oxygen.

Importantly, no peak of tungsten electrode was found in the spectra. The atomic contents of C, O, and N for NGS and NAP derived from the XPS analysis are summarized in Table 3.2. The XPS data give that the nitrogen content of NGS (6.0 at.%) was around two times higher than that of NAP (2.9 at.%), which was almost similar to the results acquired from EA analysis (Table 3.3). The XPS data give that the nitrogen content of NGS (6.0 at.%) was around two times higher than that of NAP (2.9 at.%), which was almost similar to the results acquired from EA analysis. This can be regarded that the surface is enriched with nitrogen atoms because the graphitic sheets stacks are thicker than the information depth. Also, a non-uniform distribution of surface groups throughout the carbon sample may explain this observation. [59]

Table 3.2 Surface elemental compositions in NGS and NAP by XPS analysis.

(at. %)	C	O	N	N/C
NGS	88.80	5.20	6.00	0.05
NAP	90.80	6.10	2.90	0.02

Table 3.3 Bulk elemental compositions in NGS and NAP by elemental analysis (EA).

(wt. %)	C	H	N	N/C
NGS	85.17	5.82	2.55	0.05
NAP	89.31	1.24	0.96	0.01

High-resolution XPS measurements examined more details on the chemical bonding configuration of the NGS and NAP on C 1s and N 1s peaks (Fig 3.10 (a)-(d)). High resolution asymmetric peak of C 1s region presented in Fig. 3.10 (a) and (c) indicates the presence of different carbon bondings: C=C bond (284.5 eV eV), C-C bond (285.0 eV), C-N bond (285.9 eV), C-O bond (286.5 eV), and C=O bond (287.0 eV), [56] proving the graphitic carbon and the successful incorporation of nitrogen into the carbon structure. To clarify the effect of the nitrogen incorporation, we analyzed the high-resolution N 1s peak as shown in Fig. 3.10 (b) and (d). The XPS N 1s peak can be deconvoluted into four components corresponding to pyridinic-N (398.9 eV), pyrrolic-N (400.4 eV), graphitic-N (400.9 eV), and pyridinic N-oxide (403.2 eV). [58-60] The XPS results of NGS show higher relative contents of nitrogen bonded as pyridinic-N and pyrrolic-N with 55.5 and 21.3 at. %, respectively, as compare to NAP (47.2 and 8.5 at.%, respectively) as represented in Fig. 3.10 (f). Also, the calculated atomic percentages of nitrogen bondings in the prepared samples are given in Table 3.4. It is clearly confirmed a significant increase of pyridinic-N and pyrrolic-N bonds, while there was no considerable change of graphitic-N and pyridinic oxide-N bonds in the material synthesized by the tune-up SP system. Pyridinic-N refers to nitrogen atoms possible attached at the edges of the graphite planes, where each N atom is bonded to two carbon atoms and donates one of the lone pair electrons to the aromatic π conjugation. The pyrrolic-N atom is incorporated into the five-membered heterocyclic ring, which is bonded to two carbon atoms and contributes to two p-electrons in the π system. The pyridinic-N and pyrrolic-N can be located at the graphite edge (Fig. 3.11).[61, 62] According to many references, [61-63] the formation of the edge-N which is composed of pyridinic-N and pyrrolic-N, can reduce the adsorption energy of O_2. NGS possesses a higher content of edge-N than NAP, implying that the ORR performance might be enhanced.
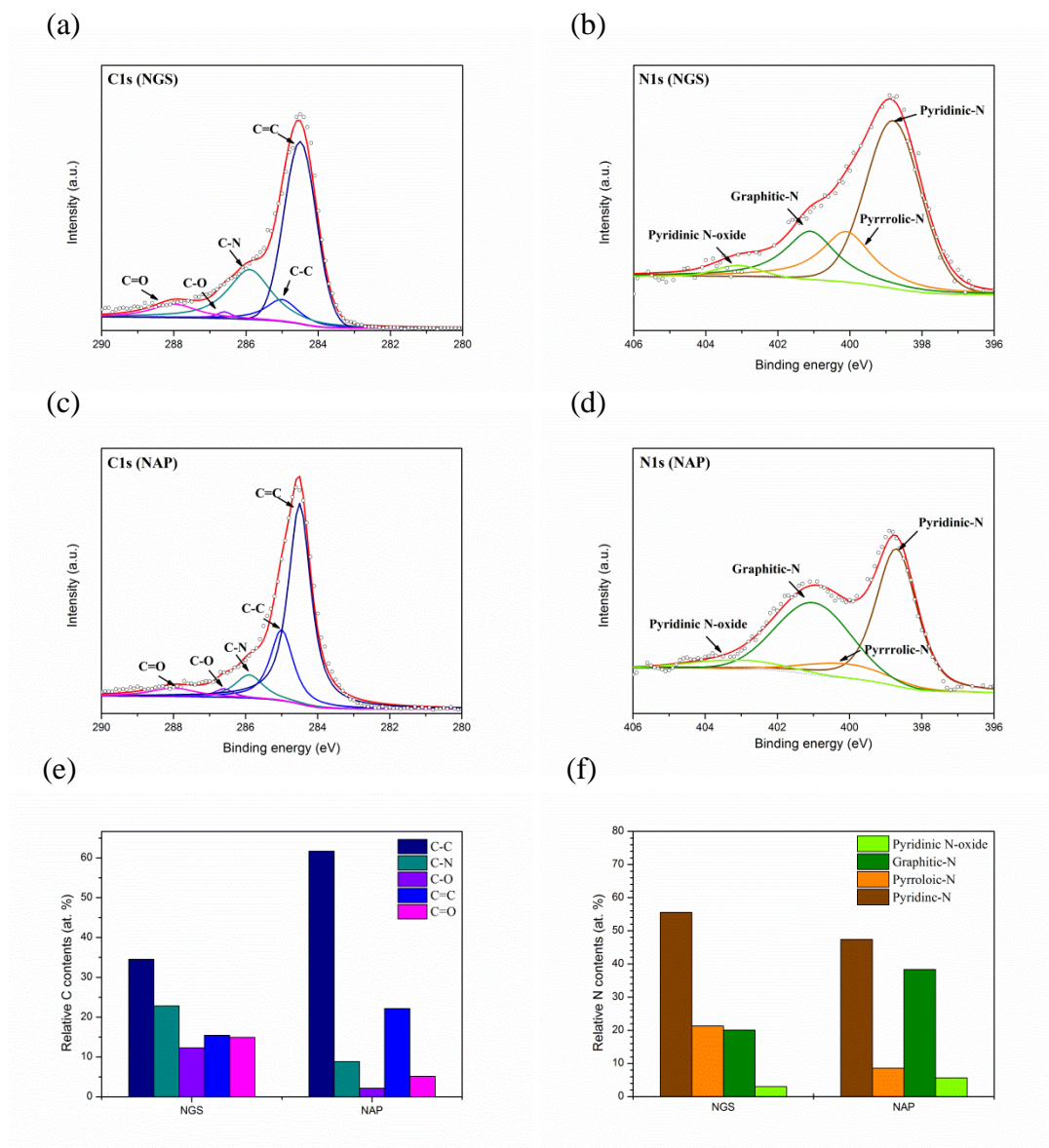
Fig. 3.10 High resolutions XPS scan of NGS and NAP for C 1s and N1s peak of (a), (b) and(c), (d), respectively. The content of N (e) and C species (f) in the NGS and NAP, respectively. NGS shows higher relative nitrogen contents when bonded as pyridinic-N and pyrrolic N with 55.5 and 21.3 at. %, respectively, as compare to NAP (47.2 and 8.5 at.%, respectively).

Table 3.4 Total surface nitrogen content and concentration of different nitrogen functionalities acquired by XPS

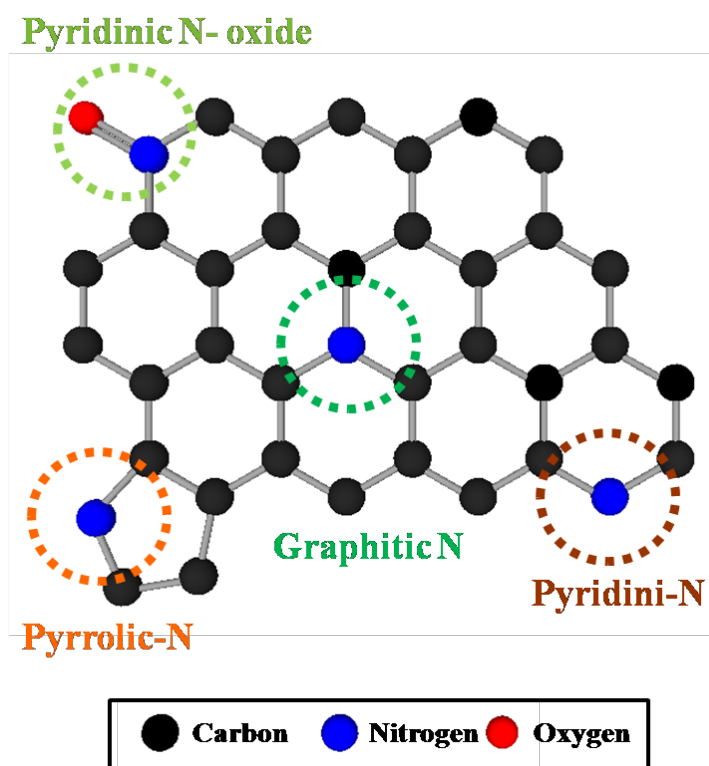| Samples	Nitrogen Content (at%)	Concentration of different nitrogen functionalities (at%)			
		Pyridinic-N	Pyrrolic-N	Graphtic-N	N-oxides of pyridinic-N
NGS	6.0	3.3	1.3	1.2	0.2
NAP	2.9	1.4	0.2	1.1	0.2

Fig. 3.11 Schematic of four types of N atoms in the nitrogen self-doped nanocarbons; pyridinc-N and pyrrolic-N is located on the edge of the graphite matrix and graphitic-N can be both edge-graphtic N and bulk-like grphitic-N.

To verify the catalytic activity, the ORR of all the synthesized nanocarbons was measured by the CV as shown in Fig. 3.12 (a). All samples show a well-defined characteristic ORR peak in O_2-saturated 0.1 M KOH solution. The peak potential of the ORR of NGS sample at -0.25 V vs. Ag/AgCl reference electrode significantly shifts to a positive value in comparison with the NAP sample with the peak potential at -0.52 V vs. Ag/AgCl.
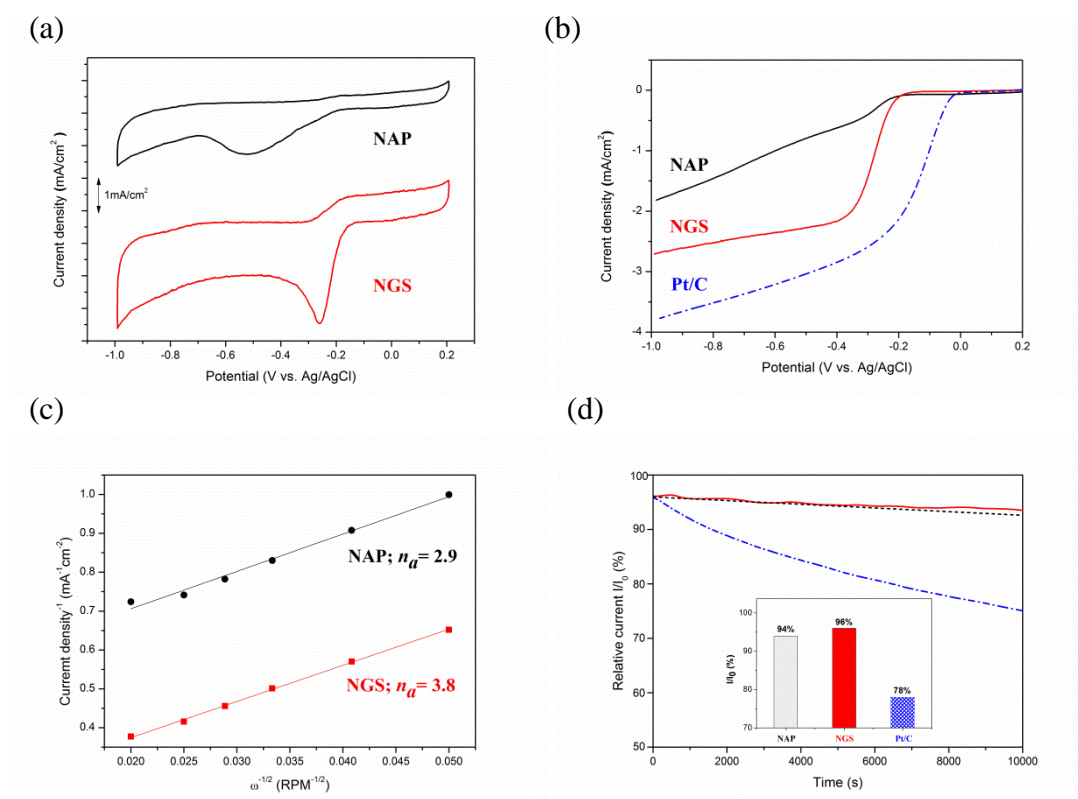

Fig. 3.12 (a) CV curves of NAP and NGS in O_2-saturated 0.1 M KOH electrolyte. (b) LSV curves on RDE of NAP and NGS, as compared 20 wt.% Pt/C in O_2-saturated 0.1 M KOH electrolyte with a sweep rate of 10 mVs-1 at a rotation speed of 1600 rpm after background correction by subtracting the measured current density in N_2-saturated solution. (c) K-L plots of J^{-1} vs. $\omega^{-1/2}$ at 0.6 V for NGS and NAP. (d) Current-time (*I-t*) chronoamperometry response of NAP, NGS, and Pt/C at -0.4 V in O2-saturated 0.1 M KOH solution during 10000 s.

Also, the NGS catalyst presents a higher cathodic current density than NAP, suggesting a considerably enhanced ORR activity due to the increased electrical conductivity. The electrical conductivity results are shown in Table 3.5. Linear sweep voltammetry (LSV) measurements on the rotating disk electrode (RDE) were further performed to verify the electrocatalytic kinetics toward ORR. For comparison, the commercial 20 wt% Pt/C as reference catalyst was measured with the same mass loading on GC electrode as the samples. Fig. 3.12 (b) exhibits LSV curves obtained from the rotation rate of 1600 rpm, which obviously exhibit the differences in the ORR activity. It is revealed a more positive onset potential (E_{onset}= -0.18 V), half-wave potential ($E_{1/2}$= -0.28 V) and higher limiting current density (LCD= 2.7 mAcm^{-2}) for NGS than those of NAP (E_{onset}= -0.21 V, $E_{1/2}$= 0.24 V and LCD= 1.8 mAcm^{-2}). Although NGS is inefficient as compared with the commercial Pt/C for what E_{onset}= -0.03 V, $E_{1/2}$= -0.14 V, and LCD=3.8 mAcm^{-2}, still it shows the possibility to be used as a metal-free catalyst in ORR. To further understand the ORR mechanism of this catalyst, ORR polarization curves of NAP and NGS at various rotations from 100 to 3600 rpm were carried out as indicated at Fig. 3.13.

Table 3.5 The conductivity test results of all samples and references.

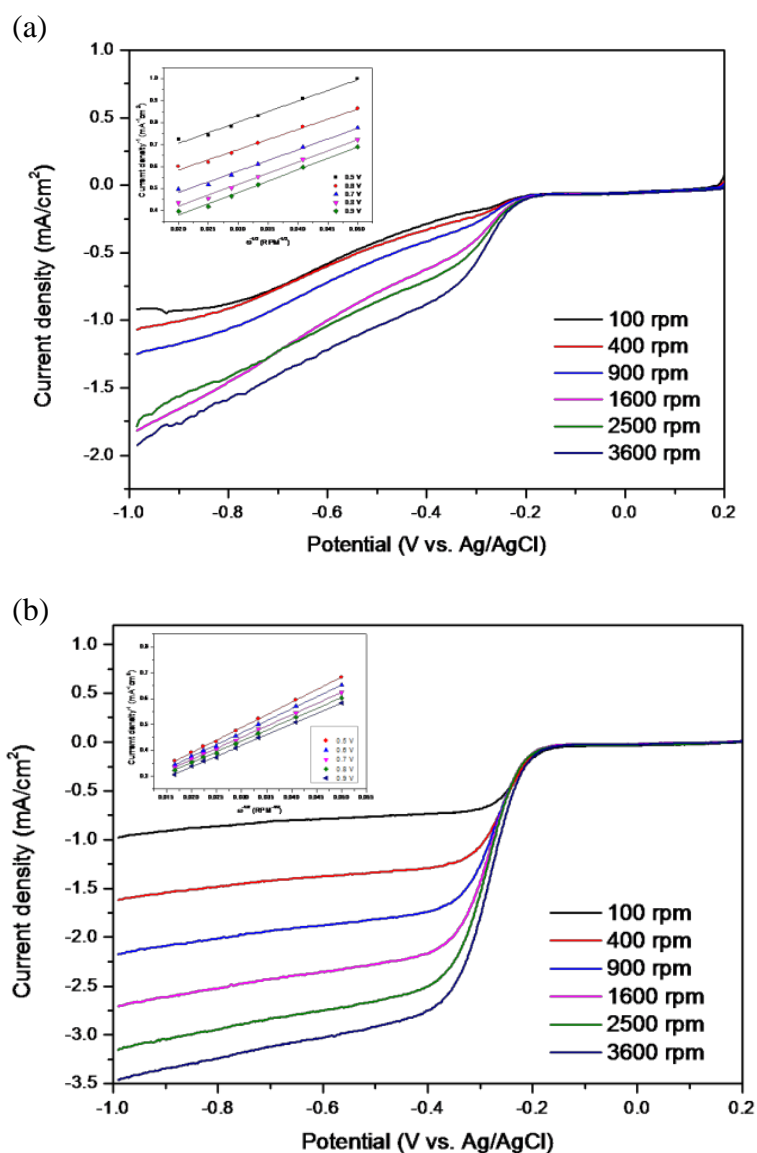| Samples	Resistivity ρ (Ω·cm)	Conductivity (S cm^{-1})	Ref
NGS	0.042	23.80	This work
NAP	1.4	0.71	This work
B and N doped graphitic carbon nanosheets	0.0289	34.60	[72]
Nitrogen-doped CNTs	0.04	25	[73]

Fig. 3.13 (a) LSV curves of NAP electrode in O2-saturated 0.1 M KOH solution with a sweep rate of 10 mV s-1 at the different rotation rates. (inset)Corresponding Koutecky-Levich (K-L) plots at different potentials. (b) LSV curves of NGS electrode in O2-saturated 0.1 M KOH solution with a sweep rate of 10 mV s-1 at the different rotation rates. (inset) Corresponding Koutecky-Levich (K-L) plots at different potentials.

The Koutechy-Levich formula was employed to calculate the average electron number (n_a) in

the reduction reaction deduced from the fact that the ORR current density is a function of the electrode rotation rates as followings; [64]

$$1/j = 1/j_L + 1/j_k \quad \quad (1)$$

$$1/j = 1/B\omega^{1/2} + 1/j_k \quad \quad (2)$$

$$B = 0.201 \ n \ FA \ C_{O2}D_o^{2/3} \ v^{-1/6} \quad \omega^{1/2} \quad (3)$$

where, j is the measured current density (mA/cm^2), j_k and j_L are the kinetic and diffusion-limiting current densities (mA/cm^2), ω is the angular velocity of the disk in rpm, F is the Faradays constant (F= 96485 C mol^{-1}), n is the number of electrons transferred per oxygen molecule, C_o * and D_o are the oxygen bulk concentration (1.2 x10^{-3} mol cm^{-3}) and diffusion coefficient of O$_2$ (1.9 X 10^{-5} cm^2 s^{-1}), respectively, and v is the kinematic viscosity of the electrolyte (1.1 × 10^{-2} cm^2 s^{-1}). According to the slope of the K-L plots inset in Fig. 3.13, the n_a of NAP was found to be 2.9, which represents a poor ORR activity, while the n_a of NGS was calculated to be 3.8, which is close to a 4 electrons transfer number on Pt/C catalyst in Fig. 3.12. The value of 3.8 may suggest that NGS was mainly dominated by a four electrons reaction pathway similar to Pt/C. On the other hand, n_a = 2.9 of NAP may proceed predominantly with a pathway of two electrons and four electrons reactions simultaneously. The higher current density and the four electrons process indicate that the NGS is a kind of high efficient ORR catalyst. Consequently, based on the above characterization of the catalyst, the enhanced electrocatalytic performance of NGS can be attributed to the good electric conductivity, high surface area, porous structure, and a high content of edge-N species. The better electric conductivity of NGS results from the sheet-like morphology and graphitic structure as compare with that of NAP, consequently determines a higher current density during ORR and assures a good electron transfer to and from the catalytic site. The relatively high surface area (621.48 m^{2}g^{-1}) and the mesoporous structure of NGS catalyst mean a lot of active sites and have a direct

influence on ORR activity and mass transfer of O_2. The analysis of N active sites was carried out by representing the onset potential together with the N species concentration as in Fig. 3.14. Importantly, the onset potential shifts more positively according to the increase of the edge-N contents, implying an enhanced ORR activity. DFT calculation [33, 32, 34] and experimental results [7, 25, 67, 68] indicate that pyridinic-N and pyrrolic-N, which possess one lone pair electrons in addition to one electron donated to the conjugated π bond, facilitate the high spin density. In conclusion, the high content of edge-N of NGS determines a good ORR activity.
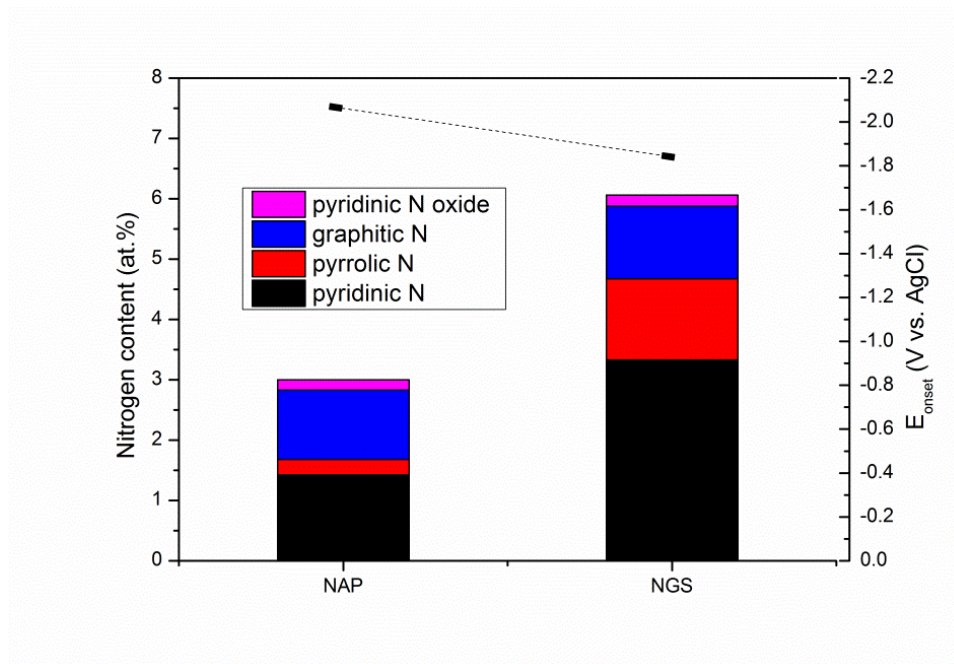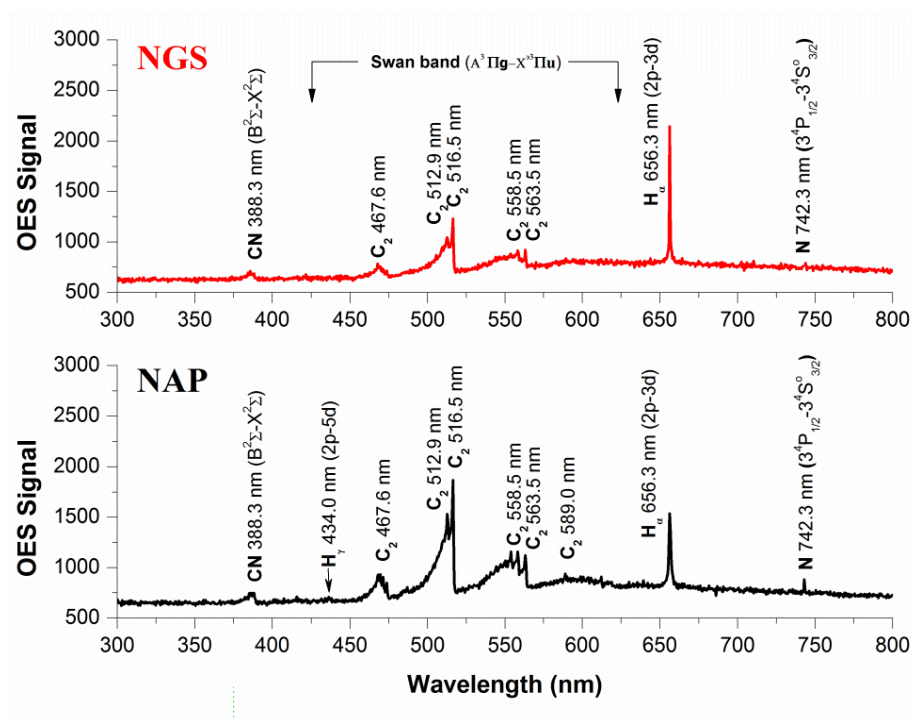

Fig. 3.14 The dependence of onset potential on the N functionality distribution.

The stability of NAP, NGS, and Pt/C catalyst was acquired by the *i-t* chronoamperometric response in O_2-saturated 0.1 M KOH solution. As shown in Fig. 3.12 (d), the current density of NGS decreases to 96% after 10000 s, which is higher than that of NAP (94%), due to the high content of pyridinic-N and pyrrolic N as well as the graphitic carbon structure in the NGS (Fig. 3.11 (f). [41] Although the electrocatalytic activity of NAP and NGS is not yet as comparable as that of Pt/C, the ORR stability presents better performance in alkaline media. The poor durability of Pt/C (78%) can be caused by the migration, aggregation of Pt particles and dissolution, and detachment from the carbon support under the continuous potential. [1, 5-7] These problems can be solved by the metal-free carbon based materials with the covalent bonding of catalytically active heteroatom in the carbon framework.
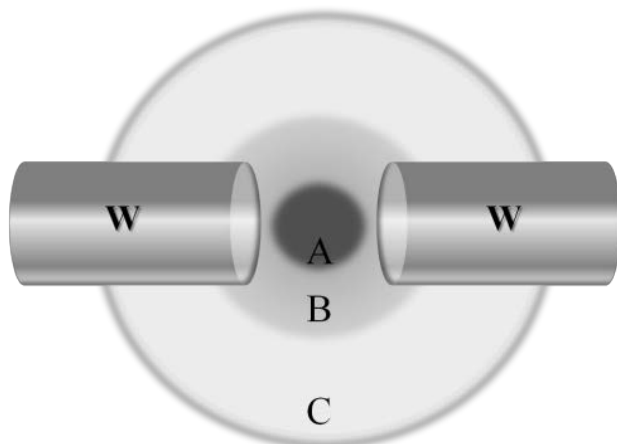
3.4 Discussion

To elucidate the differences in material characteristics between the NGS and NAP according to plasma stability during the synthesis, we performed plasma diagnostics using OES method as shown in Fig. 3.15 (a). The emission spectra present the dissociation degree of pyridine in the two types of SP and the presence of the active species as radicals in the plasma. [69] From the emission intensities, only the relative radical number density can be discussed. The Swan bands of the C_2 molecule emission are much higher intensity in the case of plasma during the synthesis of NAP that that of NGS, exhibiting a higher electron excitation energy of NAP (5000 K, 0.43eV) as shown in Table S6, which produces a higher dissociation degree of pyridine as shown in Fig. 3.15 (a). The excitation temperature of C_2 molecules in plasma was calculated to be 5000 K, which means that the organic compound was highly decomposed so that amorphous carbon structure was synthesized by carbonization.

Fig. 3.15 (a) The OES spectra of NAP (using conventional SP system) and NGS (using tune-up SP system). The Swan bands of the C_2 molecule emission are much higher intensity in the case of plasma during the synthesis of NAP that that of NGS, exhibiting a higher dissociation degree of pyridine. (b) Reaction areas according to temperature distributions during the synthesis of NGS.
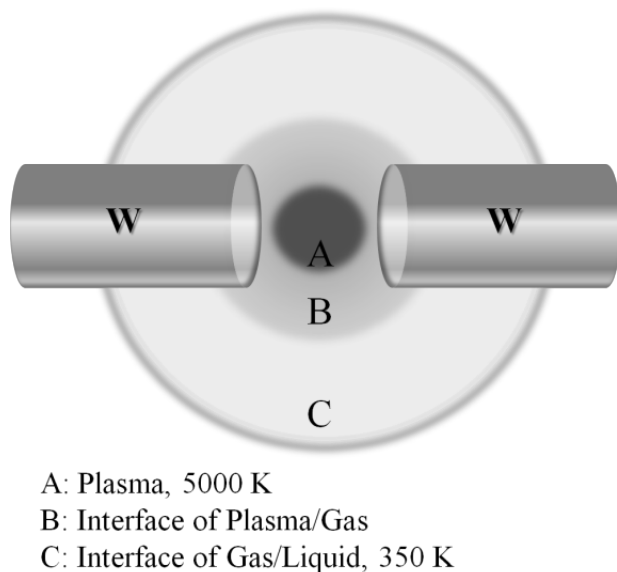
A: Plasma, 5000 K
B: Interface of Plasma/Gas
C: Interface of Gas/Liquid, 350 K

Fig. 3.16 Reaction areas according to temperature distributions during the synthesis of NAP.

On the other hands, the decomposition of C_2 molecules from the pyridine decreased when the SP system was tuned-up by the low-pass filter circuit. The C_2 molecules were mainly produced at the interface between the plasma and liquid since a large gradient of temperature from the plasma to the interface was relatively lower than of without tune-up condition (conventional SP) as shown in Fig 3.15 (b) and Fig 3.16. These C_2 molecules, which might exist as C_2H_2 and C_2H_4, lead the reaction, and subsequently, C_2 molecules are mainly assembled at the interface, which can provide the graphitic structure. [70, 71] N species can be explained in the same way as above, as well. The high dissociation of pyridine leads to nitrogen species as CN and N radicals in the conventional SP system. However, the formed nitrogen leaves plasma as a gas resulting in a low content of nitrogen in the NAP samples (Table 3.2, 3.3). In contrast, the low degree of dissociation of nitrogen in the tune-up SP system favors the preservation of the pyridine structure rather than breaking the aromatic ring. This reaction might create not only more nitrogen contents in graphitic carbon structure by aromatic rings assembling, but also create active sites with edge-N such as pyridinic-N and pyrrolic-N useful in the ORR (Fig.

3.10).

3.5 Conclusion

In summary, we suggest a novel route to synthesize nitrogen doped graphitic carbon nanosheets (NGS), using a tune-up solution plasma system. The proposed method gives several advantages over assembling of nanocarbons: (a) one-step process, (b) ambient reaction environment, (c) straightforward and easy setup, (d) cost-effective production, (e) possible large-scale of synthesis quantities, and (f) eco-friend fabrication. In particular, the tune-up SP synthesis provides stability during the discharge in liquid, influencing the synthesized nanocarbon characteristics. The NGS material has not only a large surface area, high nitrogen content, good electrical conductivity, but also the appropriate active N species of a catalyst to enhance the ORR activity. In detail, the electrochemical measurements demonstrate that NGS shows comparable catalytic activity and superior stability to Pt/C in alkaline medium, so that a low cost and large scale of nitrogen self-doped nanocarbon is a promising candidate for the next generation of electrocatalyst in metal-air batteries.

REFERENCES

[1] Mark K. Debe, Electrocatalyst approaches and challenges for automotive fuel cells, Nature 486, (2012), 43–51.

[2] Md. Arafat Rahman, Xiaojian Wang and Cuie Wenz, High Energy Density Metal-Air Batteries: A Review, J. Electrochem. Soc. (2013) volume 160, issue 10, A1759-A1771.

[3] Fangyi Cheng and Jun Chen, Metal–air batteries: from oxygen reduction electrochemistry to cathode catalysts, Chem. Soc. Rev., 2012, 41, 2172-2192.

[4] Yan Jiao, Yao Zheng, Mietek Jaroniec and Shi Zhang Qiao, Design of electrocatalysts for oxygen- and hydrogen-involving energy conversion reactions, Chem. Soc. Rev., 2015,44, 2060-2086.

[5] Cordelia Sealy, The problem with platinum, Mater. Today, 2008, 11, 65-68.

[6] R. R. Adzic, J. ZhangK. SasakiM. B. VukmirovicM. ShaoJ. X. WangA. U. NilekarM. MavrikakisJ. A. ValerioF. Uribe, Top. Catal. (2007), 46, 249-262.

[7] Kuanping Gong, Feng Du, Zhenhai Xia, Michael Durstock, Liming Dai, Nitrogen-Doped Carbon Nanotube Arrays with High Electrocatalytic Activity for Oxygen Reduction, Science, 2009, 323, 760-764.

[8] Bao Yu Xia, Ya Yan, Nan Li, Hao Bin Wu, Xiong Wen (David) Lou & Xin Wang, Nat. Energy1, A metal–organic framework-derived bifunctional oxygen electrocatalyst, 2015, 444-452.

[9] Zhongwei Chen, Drew Higgins, Aiping Yu, Lei Zhang and Jiujun Zhang, A review on non-precious metal electrocatalysts for PEM fuel cells, Energy Environ. Sci., 2011,4, 3167-3192.

[10] Qing Li, Ruiguo Cao, Jaephil Cho, Gang Wu, Nanocarbon Electrocatalysts for Oxygen Reduction in Alkaline Media for Advanced Energy Conversion and Storage, Adv. Energy Mater. 4, 1301415 (2014).

[11] Hai-Wei Liang, Xiaodong Zhuang, Sebastian Brüller, Xinliang Feng & Klaus Müllen, Hierarchically porous carbons with optimized nitrogen doping as highly active electrocatalysts for oxygen reduction, Nat. Commun., 5, 2014, 4973.

[12] Yao Zheng, Yan Jiao, Mietek Jaroniec, Yonggang Jin, Shi Zhang Qiao, Nanostructured Metal-Free Electrochemical Catalysts for Highly Efficient Oxygen Reduction, Small, 2012, 8, No. 23, 3550–3566.

[13] Jingjing Duan, Sheng Chen, Mietek Jaroniec, and Shi Zhang Qiao, Heteroatom-Doped

Graphene-Based Materials for Energy-Relevant Electrocatalytic Processes, ACS Catal., 2015, 5 (9), pp 5207–5234.

[14] Minhua Shao, Qiaowan Chang, Jean-Pol Dodelet, and Regis Chenitz, Recent Advances in Electrocatalysts for Oxygen Reduction Reaction, Chem. Rev., 2016, 116 (6), pp 3594–3657.

[15] Liming Dai, Yuhua Xue, Liangti Qu, Hyun-Jung Choi, and Jong-Beom Baek, Metal-Free Catalysts for Oxygen Reduction Reaction, Chem. Rev., 2015, 115 (11), pp 4823–4892.

[16] Yao Zheng, Yan Jiao, Lei Ge, Mietek Jaroniec, Shi Zhang Qiao, Two-Step Boron and Nitrogen Doping in Graphene for Enhanced Synergistic Catalysis, Angew. Chem. Int. Ed., 52, (2013), 3110-3116.

[17] Xuejun Zhou, Jinli Qiao, Lin Yang, Jiujun Zhang, A Review of Graphene-Based Nanostructural Materials for Both Catalyst Supports and Metal-Free Catalysts in PEM Fuel Cell Oxygen Reduction Reactions, Adv. Energy Mater. 4, 1301523 (2014).

[18] Yang. Z. Yao. Z. L. G. F. Fang, G. Y. Nie, H. G. Liu. Z., Zhou. X. M., Chen. X., Huang. S. M., Sulfur-Doped Graphene as an Efficient Metal-free Cathode Catalyst for Oxygen Reduction, ACS Nano 2012, 6, 205– 211.

[19] Li. Rong, Wei. Zidong, Gou. Xinglong, Xu. Wei, Phosphorus-doped graphene nanosheets as efficient metal-free oxygen reduction electrocatalysts, RSC Adv., (2013), 3 (25), 9978-9984.

[20] Yao. Zhen, Nie. Huagui, Yang. Zhi, Zhou. Xuemei, Liu. Zheng, Huang. Shaoming, Catalyst-free synthesis of iodine-doped graphene via a facile thermal annealing process and its use for electrocatalytic oxygen reduction in an alkaline medium, Chem. Commun., 2012, 48, 1027-1029.

[21] K.N. Wood, R. O'Hayre, S. Pylypenko, Recent progress on nitrogen/carbon structures designed for use in energy and sustainability applications, Energy Environ. Sci., 7 (2014), pp. 1212–1249.

[22] Haibo Wang, Thandavarayan Maiyalagan, and Xin Wang, Review on Recent Progress in Nitrogen-Doped Graphene: Synthesis, Characterization, and Its Potential Applications, ACS Catal., 2012, 2 (5), pp 781–794.

[23] Zhao, Y., Nakamura, R., Kamiya, K., Nakanishi, S. & Hashimoto, K. Nitrogen-doped carbon nanomaterials as non-metal electrocatalysts for water oxidation. Nature Commun. 4, 2390.

[24] Dingshan Yu, Enoch Nagelli, Feng Du and Liming Dai, Metal-Free Carbon Nanomaterials Become More Active than Metal Catalysts and Last Longer, J. Phys. Chem. Lett., 2010, 1 (14), pp 2165–2173.

[25] L. Qu, Y. Liu, J.-B. Baek, L. Dai, Nitrogen-doped graphene as efficient metal-free electrocatalyst for oxygen reduction in fuel cells, ACS Nano, 4 (2010), pp. 1321–1326.

[26] Yuyan Shao, Sheng Zhang, Mark H. Engelhard, Guosheng Li, Guocheng Shao, Yong Wang, Jun Liu, Ilhan A. Aksay and Yuehe Lin, Nitrogen-doped graphene and its electrochemical applications, J. Mater. Chem., 2010,20, 7491-7496.

[27] Da-Wei Wang and Dangsheng Su, Heterogeneous nanocarbon materials for oxygen reduction reaction, Energy Environ. Sci., 2014, 7, 576-591.

[28] A. Fasolino, J. H. Los and M. I. Katsnelson, Intrinsic ripples in graphene, Nature Materials 6, 858 - 861 (2007).

[29] A. K. Geim and K. S. Novoselov, The rise of graphene, Nature Materials 6, 183 - 191 (2007).

[30] Dang Sheng Su, Siglinda Perathoner, and Gabriele Centi, Nanocarbons for the Development of Advanced Catalysts, Chem. Rev., 2013, 113 (8), pp 5782–5816.

[31] Sheng-Feng Huang, Kiyoyuki Terakura, Taisuke Ozaki, Takashi Ikeda, Mauro Boero, Masaharu Oshima, First-principles calculation of the electronic properties of graphene clusters

doped with nitrogen and boron: Analysis of catalytic activity for the oxygen reduction reaction, PHYSICAL REVIEW B 80, 235410 (2009).

[32] Lipeng Zhang and Zhenhai Xia, Mechanisms of Oxygen Reduction Reaction on Nitrogen-Doped Graphene for Fuel Cells, J. Phys. Chem. C, 2011, 115 (22), pp 11170–11176.

[33] Elizabeth J. Biddinger, Umit S. Ozkan, Role of Graphitic Edge Plane Exposure in Carbon Nanostructures for Oxygen Reduction Reaction, J. Phys. Chem. C, 2010, 114 (36), pp 15306–15314.

[34] Heejin Kim, Kirak Lee, Seong Ihl Woo, Yousung Jung, On the mechanism of enhanced oxygen reduction reaction in nitrogen-doped graphene nanoribbons, Phys. Chem. Chem. Phys., 2011, 13, 17505-17510.

[35] Maria Antoaneta Bratescu, Osamu Takai, Nagahiro Saito, One-step synthesis of gold bimetallic nanoparticles with various metal-compositions, Journal of Alloys and Compounds, 562, (2013) 74–83.

[36] Maria Antoaneta Bratescu, Sung-Pyo Cho, Osamu Takai, Nagahiro Saito, Size-Controlled Gold Nanoparticles Synthesized in Solution Plasma, J. Phys. Chem. C, 2011, 115 (50), pp 24569–24576.

[37] Yong Kang Heo, Maria Antoaneta Bratescu, Tomonaga Ueno, Nagahiro Saito, Synthesis of mono-dispersed nanofluids using solution plasma, Journal of Applied Physics 116, 024302 (2014).

[38] Jun Kang, Oi Lun Li, Nagahiro Saito, Synthesis of structure-controlled carbon nano spheres by solution plasma process, Carbon, 60, (2013), 292-298.

[39] Dae-wook Kim, Oi Lun Li, Nagahiro Saito, Enhancement of ORR catalytic activity by multiple heteroatom-doped carbon materials, Phys.Chem.Chem.Phys., 2015, 17, 407-413.

[40] Koangyong Hyun, Tomonaga Ueno, Gasidit Panomsuwan, Oi Lun Li, Nagahiro Saito,

Heterocarbon nanosheets incorporating iron phthalocyanine for oxygen reduction reaction in both alkaline and acidic media, Phys.Chem.Chem.Phys.,2016, 18, 10856-10563.

[41] SeungHyo Lee, YongKang Heo, Maria Antoaneta Bratescu, Tomonaga Ueno, Nagahiro Saito, Solution Plasma Synthesis of Boron-Carbon-Nitrogen Catalyst with Controllable Bond Structure, Phys.Chem.Chem.Phys.,2017, 19, 15264-15272.

[42] Heo YK, Lee SH, Bratescu MA, Kim SM, Lee G-J, and Saito N., Generation of non-equilibrium condition in solution plasma discharge using low-pass filter circuit, Plasma Process Polym. 2016;9999:e201600163.

[43] NIST X-ray Photoelectron Spectroscopy Database, Version 4.1 (National Institute of Standards and Technology, Gaithersburg, (2012); http://srdata.nist.gov/xps/.

[44] B. E. Warren, P. Bodenstein, The Diffraction Pattern of Fine Particle Carbon Blacks, Acta Cryst. (1965). 18, 282-286.

[45] Z. Q. Li, C. J. Lu, Z. P. Xia, Y. Zhou, Z. Luo, X-ray diffraction patterns of graphite and turbostratic carbon, Carbon, 2007, 45, 1686-1695.

[46] T.J. Konno, R. Sinclair, Crystallization of amorphous carbon in carbon—cobalt layered thin films, Acta Metall. Mater., 43, (1995), 471-484.

[47] Latha Kumari, S.V. Subramanyam, Optical properties and electrical transport in intercalated amorphous carbon, Mater. Res. Bull., 41 (2006) 2000–2006.

[48] F. Tuinstra, J. L. Koenig, Raman Spectrum of Graphite, The Journal of Chemical Physics 53, 1126 (1970).

[49] A. C. Ferrari and J. Robertson, Interpretation of Raman spectra of disordered and amorphous carbon, Phys. Rev. B 61, (2000), 14095-14107.

[50] A. C. Ferrari, J. C. Meyer, V. Scardaci, C. Casiraghi, M. Lazzeri, F. Mauri, S. Piscanec, D. Jiang, K. S. Novoselov, S. Roth, and A. K. Geim, Raman Spectrum of Graphene and

Graphene Layers, Phys. Rev. Lett. 97, (2006), 187401.

[51] L. G. Cancado, K. Takai and T. Enoki, Applied Physics Letters, 2006, 88, 163106.

[52] K. S. W. Sing, Reporting physisorption data for gas/solid systems with special reference to the determination of surface area and porosity (Recommendations 1984), Pure & Appl. Chem., 57, (1985), 603—619.

[53] Xiaodan Huang, Kun Qian, Jie Yang, Jun Zhang, Li Li, Chengzhong Yu, Dongyuan Zhao, Functional Nanoporous Graphene Foams with Controlled Pore Sizes, Adv. Mater. 2012, 24, 4419–4423.

[54] Johan C. Groen, Louk A. A. Peffer, Javier Pérez-Ramírez, Pore size determination in modified micro- and mesoporous materials. Pitfalls and limitations in gas adsorption data analysis, Microporous and Mesoporous Materials 60 (2003) 1–17.

[55] Wei Wei, Haiwei Liang, Khaled Parvez, Xiaodong Zhuang, Xinliang Feng, Klaus Müllen, Nitrogen-Doped Carbon Nanosheets with Size-Defined Mesopores as Highly Efficient Metal-Free Catalyst for the Oxygen Reduction Reaction, Angew. Chem. Int. Ed., 53, (2014), 1570-1574.

[56] Sasha Stankovich, Dmitriy A. Dikin, Richard D. Piner, Kevin A. Kohlhaas, Alfred Kleinhammes, Yuanyuan Jia, Yue Wu, SonBinh T. Nguyen, Rodney S. Ruoff, Synthesis of graphene-based nanosheets via chemical reduction of exfoliated graphite oxide, Carbon, 45, (2007), 1558-1565.

[57] Paul H. Matter, Ling Zhang, Umit S. Ozkan, The role of nanostructure in nitrogen-containing carbon catalysts for the oxygen reduction reaction, Journal of Catalysis, 239, (2006), 83–96.

[58] J. R. Pels, F. Kapteijn, J. A. Moulijn, Q. Zhu,K. M. Thomas, Evolution of nitrogen functionalities in carbonaceous materials during pyrolysis, Carbon, 33, (1995), 1641-1653.

[59] R. J. J. Jansen, H. van Bekkum, XPS of nitrogen-containing functional groups on activated carbon, Carbon, 33, (1995), 1021-1027.

[60] F. Kapteijn, J. A. Moulijn, S. Matzner, H.-P. Boehm, The development of nitrogen functionality in model chars during gasification in CO2 and O2, Carbon, 37, (1999), 1143-1150.

[61] Linfei Lai, Jeffrey R. Potts, Da Zhan, Liang Wang, Chee Kok Poh, Chunhua Tang, Hao Gong, Zexiang Shen, Jianyi Lin and Rodney S. Ruoff, Exploration of the active center structure of nitrogen-doped graphene-based catalysts for oxygen reduction reaction, Energy Environ. Sci., 2012, 5, 7936-7942.

[62] Elizabeth J. Biddinger and Umit S. Ozkan, Role of Graphitic Edge Plane Exposure in Carbon Nanostructures for Oxygen Reduction Reaction, J. Phys. Chem. C, 2010, 114 (36), 15306–15314.

[63] Xiaogang Fu, Jutao Jin, Yanru Liu, Zhiyang Wei, Fuping Pan, and Junyan Zhang, Efficient Oxygen Reduction Electrocatalyst Based on Edge-Nitrogen-Rich Graphene Nanoplatelets: Toward a Large-Scale Synthesis, ACS Appl. Mater. Interfaces, 2014, 6 (6), 3930–3936.

[64] R. E. Davis, G. L. Horvath and C. W. Tobias, The solubility and diffusion coefficient of oxygen in potassium hydroxide solutions, Electrochimica Acta, 1967, 12, 287-297.

[65] Shankhamala Kundu, Tharamani Chikka Nagaiah, Wei Xia, Yuemin Wang, Stefan Van Dommele, Johannes Hendrik Bitter, Monika Santa, Guido Grundmeier, Michael Bron, Wolfgang Schuhmann and Martin Muhler, Electrocatalytic Activity and Stability of Nitrogen-Containing Carbon Nanotubes in the Oxygen Reduction Reaction, J. Phys. Chem. C, 2009, 113 (32), 14302–14310.

[66] Nalini P. Subramanian, Xuguang Li, Vijayadurda Nallathambi, Swaminatha P. Kumaraguru, Hector Colon-Mercado, Gang Wu, Jong-Won Lee, Branko N. Popov, Nitrogen-

modified carbon-based catalysts for oxygen reduction reaction in polymer electrolyte membrane fuel cells, Journal of Power Sources, 188, (2009), 38-44.

[67] Chitturi Venkateswara Rao, Carlos R. Cabrera, and Yasuyuki Ishikawa, In Search of the Active Site in Nitrogen-Doped Carbon Nanotube Electrodes for the Oxygen Reduction Reaction, J. Phys. Chem. Lett., 2010, 1 (18), 2622–2627.

[68] Jingjie Wu, Lulu Ma, Ram Manohar Yadav, Yingchao Yang, Xiang Zhang, Robert Vajtai, Jun Lou, and Pulickel M. Ajayan, Nitrogen-Doped Graphene with Pyridinic Dominance as a Highly Active and Stable Electrocatalyst for Oxygen Reduction, ACS Appl. Mater. Interfaces, 2015, 7 (27), 14763–14769.

[69] R. W. B. Pearse and A. G. Gaydon, The Identification of Molecular Spectra, Chapman and Hall, New York, 1976.

[70] Morishita T., Ueno T., Panomsuwan G., Hieda J., Yoshida A., Bratescu M. A., and Saito N., (2016) Fastest Formation Routes of Nanocarbons in Solution Plasma Processes. Scientific Reports, 6, 36880.

[71] Jaganathan Senthilnathan, Chih-Chiang Weng, Jiunn-Der Liao and Masahiro Yoshimura, Scientific Reports, 3, 2414 (2013)

[72] K. Fujisawa, T. Tojo, H. Muramatsu, A. L. Elías, S. M. Vega-Díaz, F. Tristán-López, J. H. Kim, T. Hayashi, Y. A. Kim, M. Endo and M. Terrones, Nanoscale, 2011, 3, 4359.

[73] L. Wang, P. Yu, L. Zhao, C. Tian, D. Zhao, W. Zhou, J. Yin, R. Wang and H. Fu, Sci. Rep., 2014, 4, 5184.

Chapter 4
Solution Plasma Synthesis of Boron-Carbon-Nitrogen Catalyst with Controllable Bond Structure

Chapter 4 Solution Plasma Synthesis of Boron-Carbon-Nitrogen Catalyst with Controllable Bond Structure

4.1 Introduction

Boron-carbon-nitrogen (BCN) ternary systems with graphitic phase have been highlighted for their novel structural and electronic properties. [1-10] Interestingly, BCN nanocarbon can be regarded as alternative low-cost metal-free electrocatalysts for oxygen reduction reaction (ORR). [2, 11-18] Electrochemical oxygen reduction activity is an essential reaction in metal-air cells and fuel cells which are catalyzed on cathodes by commercial noble metal materials (e.g., Pt or Pd based). High Pt loading is required to secure the efficient ORR performance by overcoming the slow reaction kinetics of the cathode. However, the high cost and the finite resources of Pt as well as the short-term stability and inactivation by CO poisoning, have obstructed large-scale commercialization of the metal-air batteries and fuel cells. [19-21] One of the most feasible Pt alternatives is the carbonaceous materials, which have attracted considerable attention either as catalyst supports or as metal-free catalysts in the electrocatalytic chemistry of oxygen. [22-28]

Carbon provides outstanding advantages including low cost, wide availability, high electrical conductivity and good stability under harsh conditions. [22] Although the abundant π electrons in the *sp2* carbon materials could make them as potential catalysts for reactions needing electrons, these conjugated π electrons are not active to directly react in ORR. [12, 13] Therefore, heteroatoms such as N, B, P, I, and S doping the carbon materials is an emerging field.[16, 29] In particular, N and B-doped carbon-based materials have drawn extensive

attention as new non-noble catalysts for ORR. Co-doping with two elements, one with higher and one with lower electronegativity than that of carbon ($\chi=2.55$) such as nitrogen ($\chi=3.04$) and boron ($\chi=2.04$) can create charged sites in the carbon that are favorable for O_2 adsorption. Also, the unique electronic structure with a synergistic effect between heteroatoms makes such dual doped carbon-based catalysts much more catalytically active than single dopant of carbon-based catalysts. [14, 17, 30] However, the compensation effect between the p- (B atoms) and n–type (N atoms) dopants would result in the formation of boron nitride, for example, during the synthesis of BCN nanocarbon, leading to inactive ORR activity. [2, 3, 12, 17] Current approaches based on the chemical vapor deposition (CVD) [4, 10, 30-34] and the chemical method involving the co-annealing of graphite oxide under boric acid and ammonia conditions are the most common and successful synthesis methods for boron and nitrogen co-doped carbon.[11, 14, 35] Indeed, although an extensive research has been carried out on nitrogen and boron co-doping in carbon for ORR, few studies exist which adequately covers the synergistic effect according to the conjugation of B-C-N for the ORR activity. Thus, it is necessary to demonstrate that the synergistic effect according to how two dopants co-exist chemically in the carbon framework such as coupling or uncoupling leads to different electronic structure, these also undoubtedly facilitate the distinct electrocatalytic ORR.

In our previous work, we reported an emerging synthesis method, named Solution Plasma Process (SPP) defined as non-equilibrium plasma in solutions. The method has been used to synthesize successfully heteroatoms doped in carbonaceous materials by utilizing a simple organic precursor. [36-40] In the present work, SPP is characterized by conserving the bond structure of the monomer applied as the starting material followed by polymerization via the activated species from precursors. [41] This novel strategy enables the simultaneous synthesis of nanocarbon, incorporation of heteroatoms into the nanocarbon matrix, as well as the control

of the bond structure of the dopants. Another significant advantage of SPP consists of the processing time which is much faster than that of the conventional methods, such as CVD and annealing of various organic compounds. In this study, we have synthesized BCN nanocarbon with different bond structures (B/N coupling and uncoupling) by SPP and the electrocatalytic activity of BCN nanocarbon was investigated through the chemical bond state between B and N.
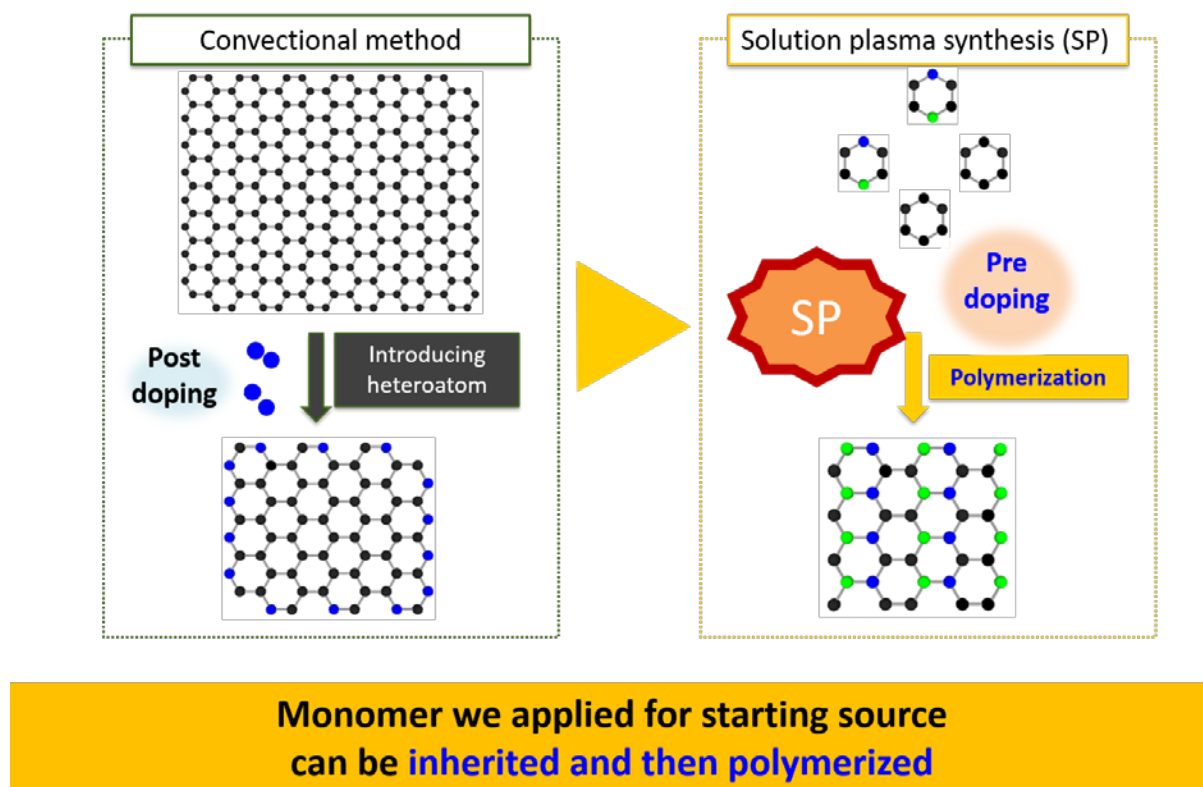

Fig. 4.1 Concept of SPP for simultaneous synthesis of nanocarbon, incorporation of heteroatoms into the nanocarbon matrix, as well as the control of the bond structure of the dopants.

4.2 Experimental procedure

4.2.1 Synthesis of BCN nanocarbon by SPP

SPP was performed by using a pair of tungsten electrodes (Φ0.8, purity 99.9%, Nilaco Corporation) shielded with an insulating ceramic tube placed in the center of the Teflon® vessel with a gap distance of 1.0 mm (Fig. 4.2). A bipolar pulsed power supply (MPS-R06K01C-WP1-6CH, Kurita, Japan) with variable pulse width and repetition frequency was used to generate plasma. The optimized conditions of the discharge were found to be 0.5 μs and 100 kHz, and 2 kV for the pulse duration, pulse repetition frequency, and voltage, respectively. The discharge in the liquid was produced during 30 min. in various solvents serving as carbon, nitrogen and boron precursors for synthesizing BCN nanocarbon. The optical emission spectra (OES) were measured during the synthesis using a spectrograph coupled to an optical fiber.
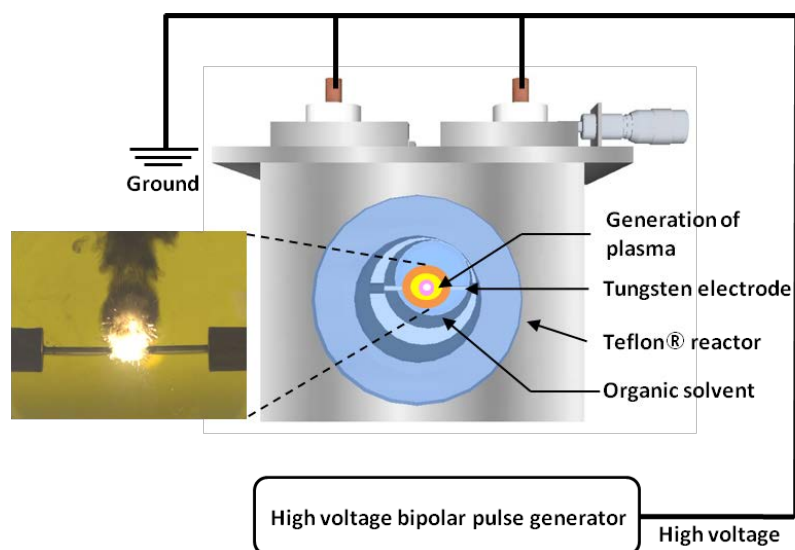

Fig. 4.2 Schematic illustration of the experimental set-up for solution plasma process. The inserted photo shows the discharge during the BCN nanocarbon synthesis.

Two different strategies to control the bond configuration were applied to prepare the nitrogen and boron co-doping nanocarbon. The synthesis of B/N coupling nanocarbon material consists in the processing of 200 mL of pyridine (C_5H_6N, Kanto Chemical) as a pure precursor including carbon and nitrogen atoms in the ring and 20 mM of B-tribromoborazine ($H_3B_3Br_3N_3$, Wako Chemical) as a boron source. The contained stable B-N single bond in the ring of B-tribromoborazine could be preserved, producing B/N coupling nanocarbon. The B/N uncoupling nanocarbon material was synthesized by using 200 mL of pyridine and 20 mM of boric acid (H_3BO_3, Kanto Chemical) as a boron source. In this configuration, N-doped nanocarbon is preferentially synthesized, and B atom dopes the N-doped carbon, hence determining the uncoupling bond between N and B atoms.

The properties of different single dopants in the carbon structure were investigated. So only the N-doped nanocarbon was prepared by using 200 mL of pyridine, and the B-doped nanocarbon was produced by using 20 mM of boric acid in 200 mL of benzene (C_6H_6, Kanto Chemical) solvent, which has only C atoms in the aromatic ring. The produced materials with different bond states of the heteroatom doping carbon were denoted as CN (only N-doped), CB (only B-doped), B/N coupling (B and N co-doped with a chemical bond between B and N), and B/N uncoupling (B and N co-doped with C separately bonded to B and N). To purify the obtained carbon materials, the solution after SPP was filtrated using a 100 nm membrane filter paper by a suction pump system. The obtained carbon materials were dispersed, washed and filtrated in 200 ml pyridine solution. This process was repeated for several times until the wash solvent became colorless.

4.2.2 Characterization

Transmission electron microscopy, scanning electron microscopy, selected area electron diffraction, and energy dispersive spectroscopy (TEM, SEM, SAED, and EDS, JEOL JEM-2500SE at 200 kV) observations were conducted to study the microstructure, shape, and size of the synthesized heteroatom-doped carbon. X-ray diffraction patterns (XRD, Rigaku Smart Lab) were obtained using Cu Kα (1.54 Å) as the X-ray source using a scan range from 10° to 60° with 0.02° step and 2° min^{-1} scan speed. Raman spectra were acquired by a Raman spectrometer (JASCO NRS-3100) equipped with a laser excitation wavelength at 785 nm. The chemical bond structures were examined by X-ray photoelectron spectroscopy (XPS, Ulvac-PHI 5000 VersaProbe II). All the measurements were carried out using Al Kα radiation (1486.6 eV) as an X-ray source. The emission current and anode voltage were operated at 0.1 mA and 15 kV, respectively. The values of the binding energies were calibrated with respect to the C1s peak on 284.5 eV. The spectra of N1s, B1s, and C1s were curve-fitted using mixed Gaussian-Lorentzian component profiles using the PHI MultiPak data analysis software installed in XPS. The full width at half maximum of the peak was limited to a maximum value of 1.8 eV and the binding energy was mainly referred from NIST XPS Database. [42]

4.2.3 Electrochemical characterization

To examine the electrochemical properties of the synthesized BCN nanocarbon, cyclic voltammetry (CV) and linear sweep voltammetry (LSV) were conducted using a three-electrode electrochemical cell with a potentiostat (Hokudo Denko Inc. HZ-5000). The three-electrode cell consists of a glassy carbon (GC) electrode (3 mm in diameter) as working electrode, a Pt wire counter electrode and Ag/AgCl reference electrode (in saturated KCl solution). The GC electrode coated with the sample was attached to the rotating disk electrode

(RDE) system. The samples used in the electrochemical measurements to cover the GC electrode were prepared as follows: 50 µL of Nafion® solution (Aldrich, 5 wt% Nafion®) was added in 0.5 mL ethanol, and then 5 mg of finely ground catalyst was dispersed in the as-prepared solution by at least 30 min sonication to form a homogeneous suspension. The carbon materials loaded on the electrode was then dried in air for 12 h at room temperature before the electrochemical measurements, yielding a uniformly smooth surface with a catalyst loading of 0.1 mg_{cat} cm^{-2}. For comparison, a commercial 20 wt.% platinum on graphitized carbon (Sigma-Aldrich) catalyst loaded on the GC electrode was also prepared to adjust a catalyst amount of 0.02 mg_{Pt}cm^{-2}. CV and LSV were conducted in a 0.1 M KOH electrolyte saturated with O_2, from -1.0 to 0.3 V (vs. Ag/AgCl), and with a scan rate of 50 mVs^{-1} and 10 mVs^{-1}, respectively. The rotation speed was varied from 400 to 2500 rpm. The commercial 20 wt. % Pt/C was selected as a performance benchmark. The electrochemical durability was measured by chronoamperometric responses in 0.1 M KOH saturated with oxygen during 20000 s at -0.4 V. When the number of transferred electrons was calculated by K-L equation, the background of current density, i.e., capacitive current, was corrected based on the current density in N_2 saturated solution.
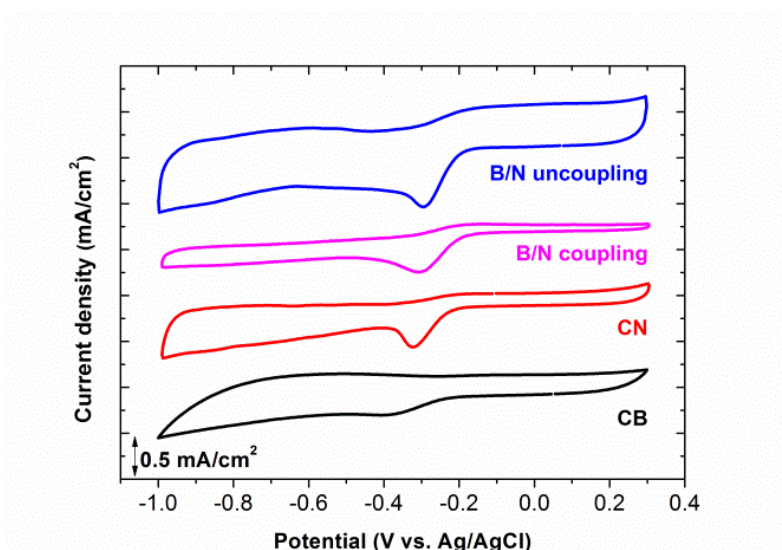
4.3 Results and discussion
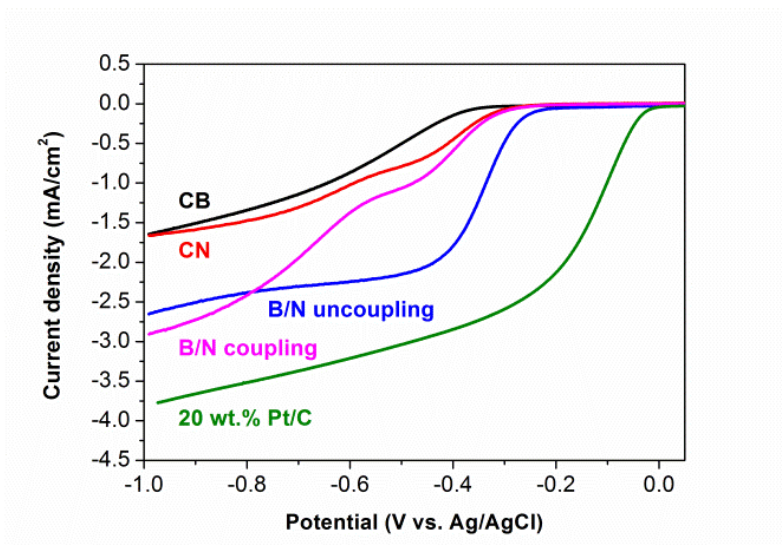
4.3.1 Electrocatalytic activity toward ORR

The electrocatalytic oxygen reduction was used as a probe reaction to understand the synergistic effect of the BCN nanocarbon. The influence of single or binary dopants on the ORR activity was first evaluated using the CV method (Fig. 4.3 (a)). In the saturated oxygen condition, a clear reduction peak appears between -0.37 and -0.28V in the CV curves of all the samples. Between the nanocarbon doped with a single dopant, the CN material shows better

84

ORR performance than CB nanocarbon, but still having a small ORR activity. The ORR peaks observed in the CV indicate a weak and inefficient four-electron ORR process. The performances of both dual doped nanocarbons present a higher cathodic current density and more positive onset potential, which means more efficient ORR activity than the single doped nanocarbons. In the case of the dual doped nanocarbons, the B/N uncoupling shows more positive onset potential and higher cathodic current density, which reveals better ORR activity than the B/N coupling material.
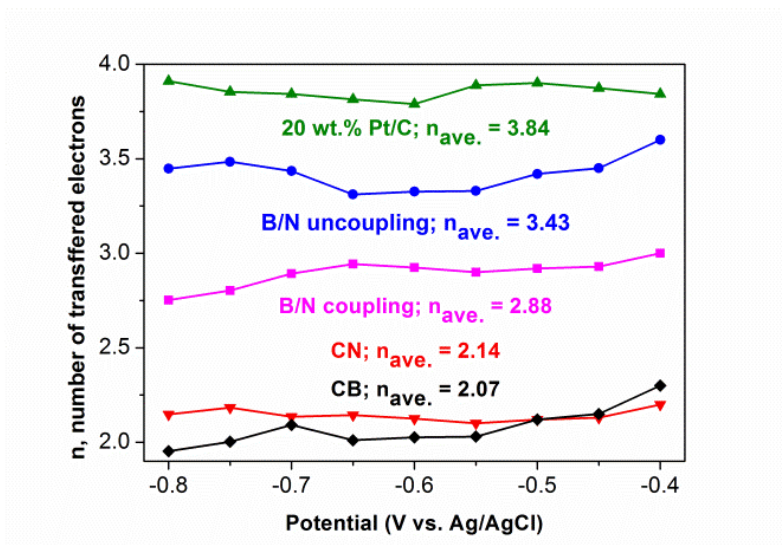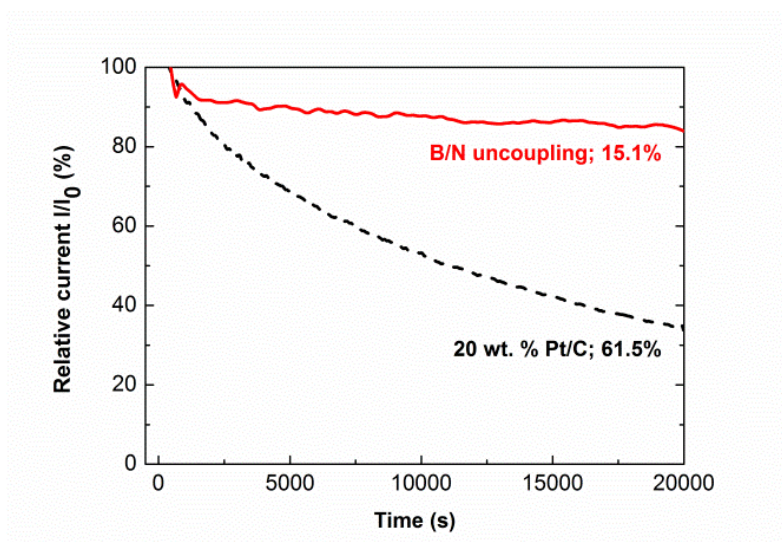
(a)

(b)

(c)

(d)

Fig. 4.3 Electrochemical measurements: (a) CV curves of CB, CN, B/N coupling and B/N uncoupling in an O_2-saturated 0.1 M KOH solution at a scan rate of 50 mV s^{-1}. (b) LSV curves of CB, CN, B/N coupling, B/N uncoupling, and 20 wt. % Pt/C in 0.1 M KOH solution at a rotation speed of 1600 rpm and a scan rate of 10 mV s^{-1}. (c) The number of the transferred electrons per O_2 molecule at different potential ranging from -0.4 to -0.8 V for CB, CN, B/N coupling, B/N uncoupling and 20 wt. % Pt/C. (d) Current-time *(I-t)* chronoamperometry response of B/N uncoupling and Pt/C at -0.4 V in O_2-saturated 0.1 M KOH solution during 20000 s.

86

To gain further insight into the ORR activity, we performed the LSV at a rotation speed of 1600 rpm using RDE (Fig. 4.3 (b)). The active sites of the material give the onset potentials which are determined by the bond state of nitrogen and boron in nanocarbon. It is worthy to note that all co-doped catalyst showed more positive onset potential, which indicates more productive ORR activity than single dopant (Fig. 4.3 (b)). The LSV curve of the CB and CN nanocarbon exhibits relatively weak ORR activity with the onset potential at -0.37 and -0.30 V (vs. Ag/AgCl reference), respectively and a low cathodic current density of -0.8 and -1.0 mA cm^{-2} at -0.6 V, respectively. According to the dual doping condition, the ORR onset voltage progressively moves toward a more positive direction, and the small cathodic current density remarkably also increased. Especially, the B/N uncoupling indicates the highest ORR activity concerning both onset potential (-0.25 V vs. Ag/AgCl) and the limiting cathodic current density (-2.25 mA cm^{-2} at -0.6 V). This result clearly implies the enhanced synergistic activity of the B/N uncoupling nanocarbon which can boost the activity of the carbon structure by generating additional active sites. To explore the ORR mechanism and the key electrocatalytic processes of the prepared catalysts, we carried out RDE experiments for BCN nanocarbon (Fig. 4.4 and 4.5). The kinetic and diffusion mechanisms of the reduction reaction can be explained by the slope of Koutecky-Levich (K-L) equations (see Supporting Information).[43] Fig. 4.3 (c) presents the calculated number of transferred electrons for ORR found to be 3.43 for the B/N uncoupling nanocarbon, which is the closest value to that of the commercial Pt/C catalyst (n= 3.84). The long term durability is another important requirement to realize practical applications of the metal-air batteries and fuel cells. The current-time chronoamperometric response was measured for the most active BNC nanocarbon and the commercial 20 wt. % Pt/C catalyst to confirm the durability, as is shown in Fig. 4.3 (d). The relative current density (I/I$_0$) of B/N uncoupling exhibits a slow rate of attenuation and decreases to approximately

84.9% after 20000 s. For the commercial 20 wt. % Pt/C catalyst, the relative current density reduces to about 38.5% after 20000 s. Although the ORR activity of the B/N uncoupling material is not yet as comparable as that of the 20 wt. % Pt/C catalyst, its satisfactory ORR activity and reliable stability hold promise for use in the direct metal-air cell and fuel cells.
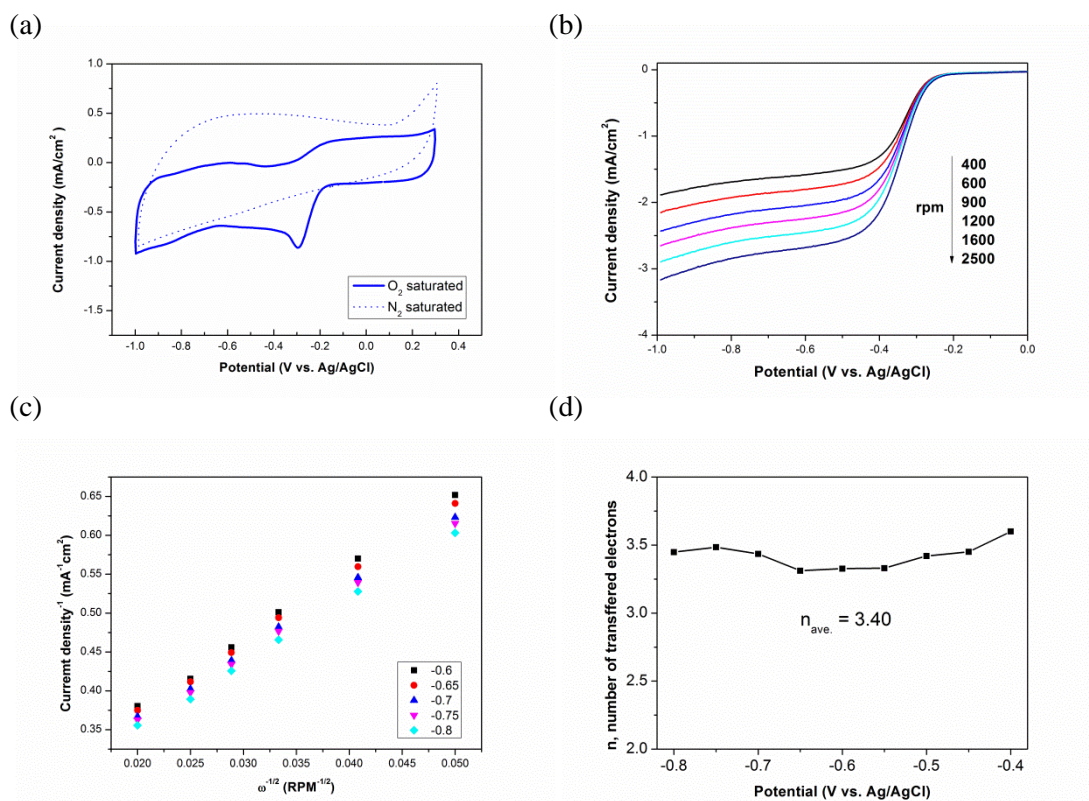

Fig. 4.4 Electrochemical measurements of B/N uncoupling: (a) CV curves of the ORR in O_2 and N_2-saturated 0.1M KOH solutions at a scan rate of 10 mV s^{-1}. (b) LSV curves of the ORR in O_2-saturated 0.1 M KOH solution at a scan rate of 10 mV s^{-1} with different rotation speeds from 400 to 2500 rpm. (c) The Koutecky-Levich (K-L) plots of current density^{-1} versus $\omega^{-1/2}$ at various potentials obtained from LSV curves in an O_2-saturated 0.1 M KOH solution at a scan rate of 10 mV s^{-1}. (d) The number of transferred electrons calculated from the slopes of the K-L plots in (c).
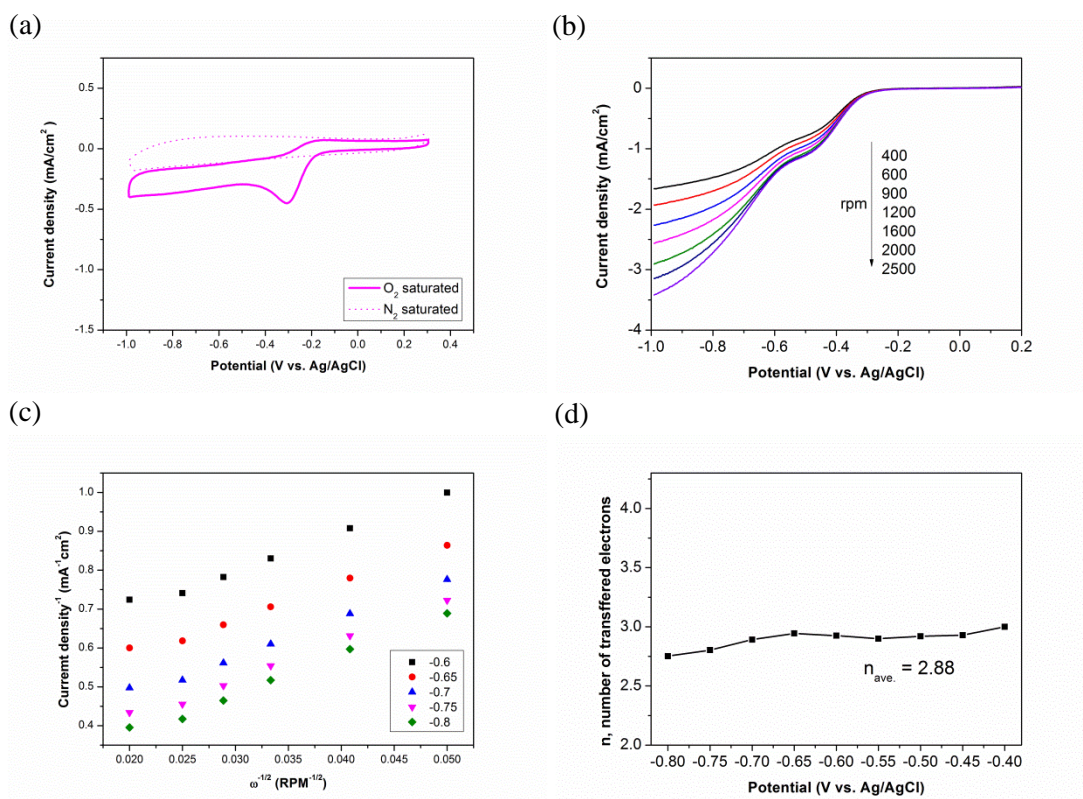
Fig. 4.5 Electrochemical measurements of B/N coupling: (a) CV curves of the ORR in O_2 and N_2-saturated 0.1M KOH solutions at a scan rate of 10 mV s^{-1}. (b) LSV curves of the ORR in O_2-saturated 0.1 M KOH solution at a scan rate of 10 mV s^{-1} with different rotation speeds from 400 to 2500 rpm. (c) The Koutecky-Levich (K-L) plots of current density^{-1} versus $\omega^{-1/2}$ at a various potentials obtained from LSV curves in an O_2-saturated 0.1 M KOH solution at a scan rate of 10 mV s^{-1}. (d) The number of transferred electrons calculated from the slopes of the K-L plots in (c).
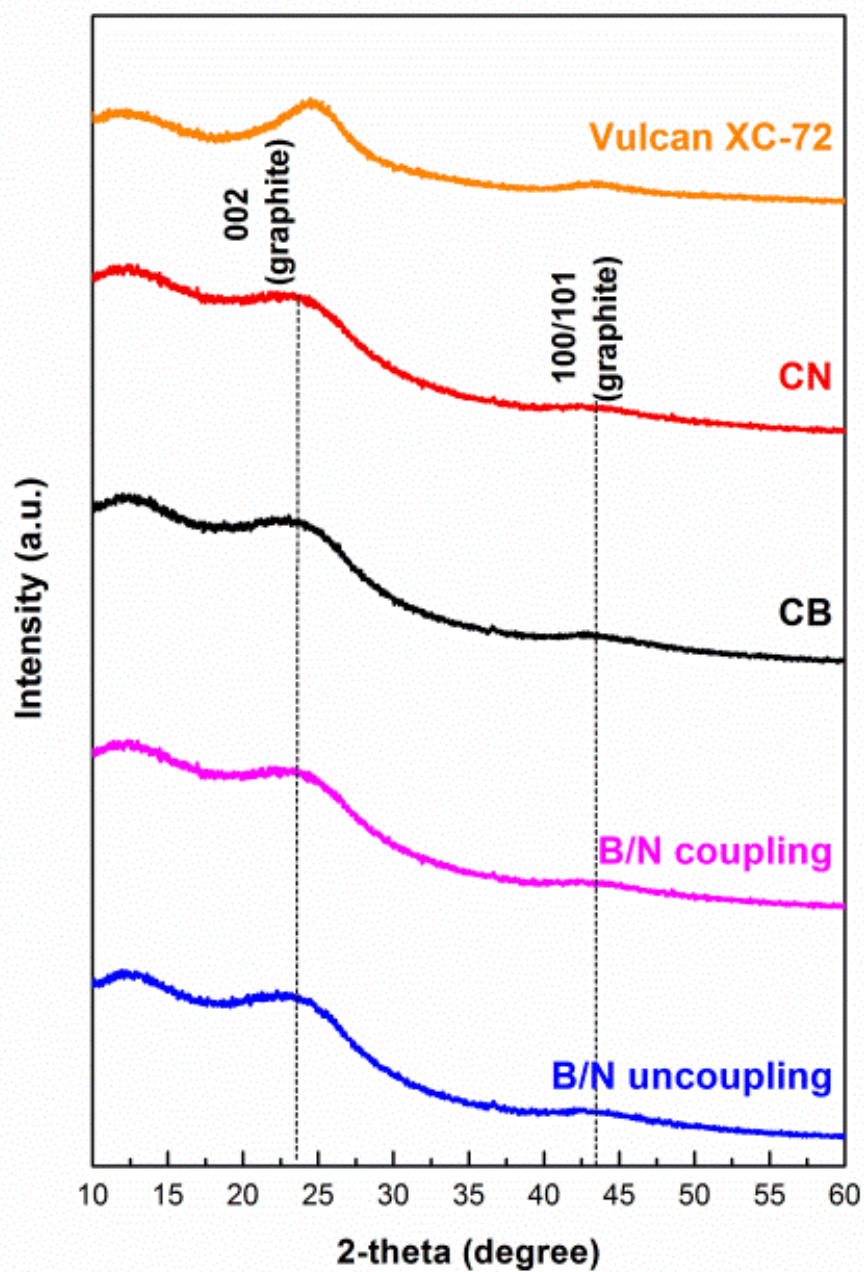
4.3.2 Structure and morphology

X-ray diffraction studies revealed structural information of the CB, CN, B/N coupling, and B/N uncoupling nanocarbon materials compared to commercial carbon black Vulcan XC-72 (Fig. 4.6 (a)). There are two kinds of broad peaks at 2θ = 23.3° and 43.3° which indicate (002) and (100) diffraction planes of graphite, respectively. The broad diffraction peak on (002) basal plane means that all the prepared samples are composed of small crystallized structures with a partially disordered moiety. Also, all the nanocarbon materials show a negative shift and a decrease in the intensity of the 002 peak compared to the peaks of Vulcan XC-72 and standard graphite powder (2θ= 26.5º), [44] mainly due to the smaller crystallite size and the increasing of the disordered structure.

Additional structural information was obtained by Raman spectroscopy of all nanocarbon materials. Two prominent peaks emerged near 1350 cm^{-1} and 1590 cm^{-1}, which are associated with the D band and G band, respectively (Fig. 4.6 (b)). The G band refers to the E_{2g} vibration mode in the D^4_{6h} symmetry group of graphite crystal planes, while the D band is attributed to breaking of the symmetry caused by disorder or structure (e.g., lattice distortion, bond length disorder, vacancy, and impurity). The relative intensity ratio of D and G band (I_D/I_G) is used as a measure of carbon disorder, and a high value indicates numerous defects in the carbon structure. [45] The I_D/I_G values for the prepared catalysts are also noted in Fig. 4.6 (b). The I_D/I_G values of CN and CB, which are single doped nanocarbons, were lower than that of the dual doped nanocarbons. Moreover, the crystallite size L_a of the nanocarbons was calculated from the equation: $L_a(nm) = (2.4\times 10^{-10})\lambda_l^4(I_D/I_G)^{-1}$, where λ_l is the laser wavelength in nanometer units (Fig. 4.6 (b)). [46] We observed that the crystallite size of dual doped nanocarbons was smaller than single doped nanocarbons since the incorporation of the nitrogen and boron atoms into the nanocarbon structure creates structural defect sites and higher degrees
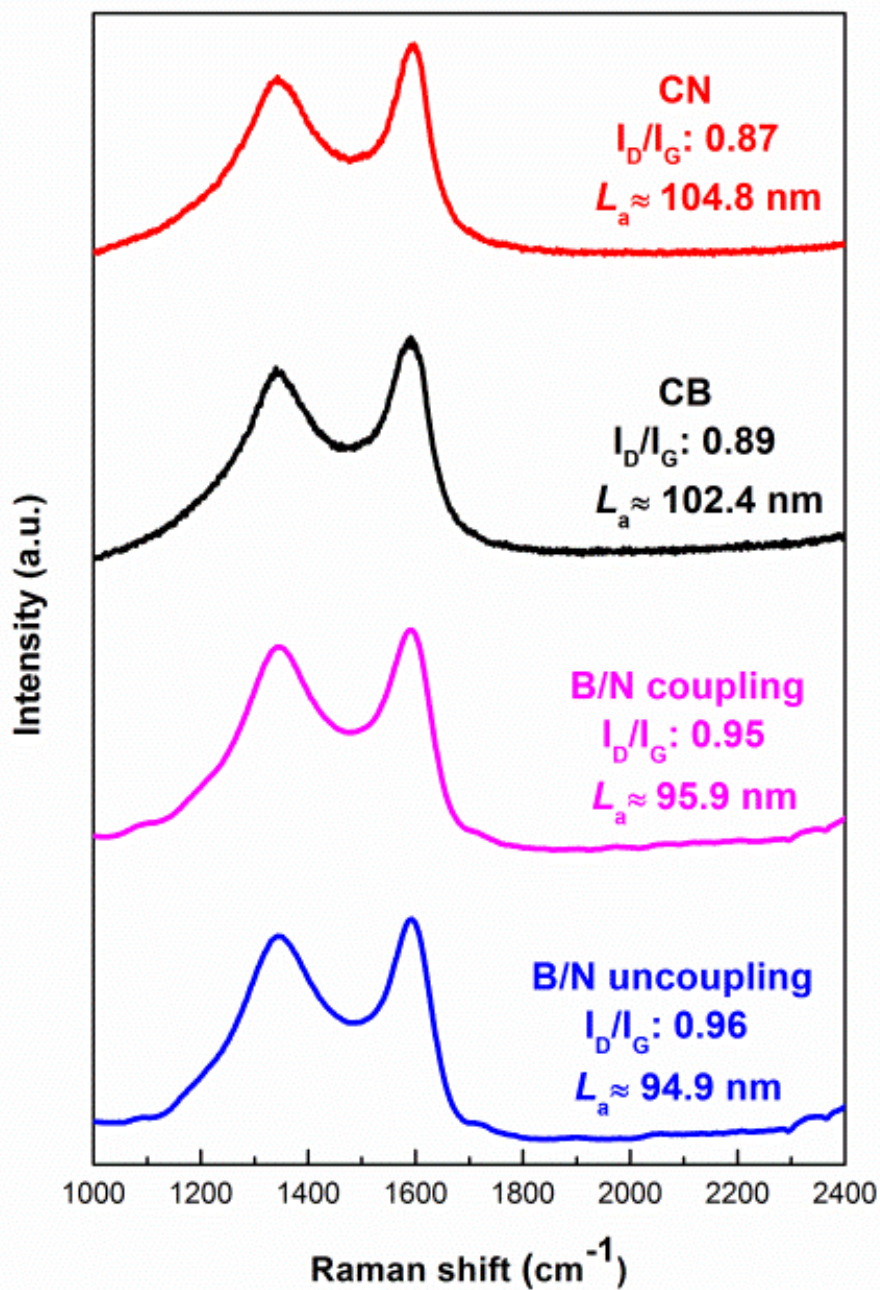
of disorder.

(a)

(b)

Fig. 4.6 (a) XRD patterns of CN, CB, B/N uncoupling, B/N coupling, and commercial carbon (Vulcan XC-72). (b) Raman spectra with the corresponding I_D/I_G ratios and crystallite size (L_a, nm) of CN, CB, B/N coupling, and B/N uncoupling.

The morphology of the catalysts was investigated by TEM and SEM. A representative TEM image of B/N uncoupling reveals a flake-like morphology as shown in Fig. 4.7 (a). Also, Fig. 4.8 (a-c) presents wide-field TEM images with selected-area electron diffraction (SAED) of CB, CN and B/N coupling. The average layer distances corresponding to the interlayer distance (d_{002}) were evaluated by the contrast line profiles obtained from high-resolution TEM images (Fig. 4.9). From wide-field TEM images and SEM images (Fig. 4.8 (d)), all nanocarbons are exhibited a flake-like morphology as well. All the SAED patterns show two diffuse rings, where the inner ring is the diffraction attributed to 002 plane indices and the outer ring is the diffraction to 001 plane indices. This ring patterns and the diffusion resulted from polycrystalline and the small crystallite size and an increase of random layer stacking structure, respectively. The interlayer distance obtained from contrast profiles were around 0.38 nm, which is in accordance with the d_{002} values of synthesized carbon (ca ≈ 0.38 nm). Also, these distances are longer than of ideal graphite (0.335 nm), [47, 48] which originates in the decrease of the π-π stacking interactions among layers, i.e., the decrease of the number of stacking layers, the decrease of the crystallite size, and the presence of randomly layered stacking structure. This result also agrees with the small crystallite size L_a obtained from Raman spectroscopy. In the EDS mapping, as shown in Fig. 4.7 (c), the B, C and N elements were homogeneously observed in B/N uncoupling carbons.
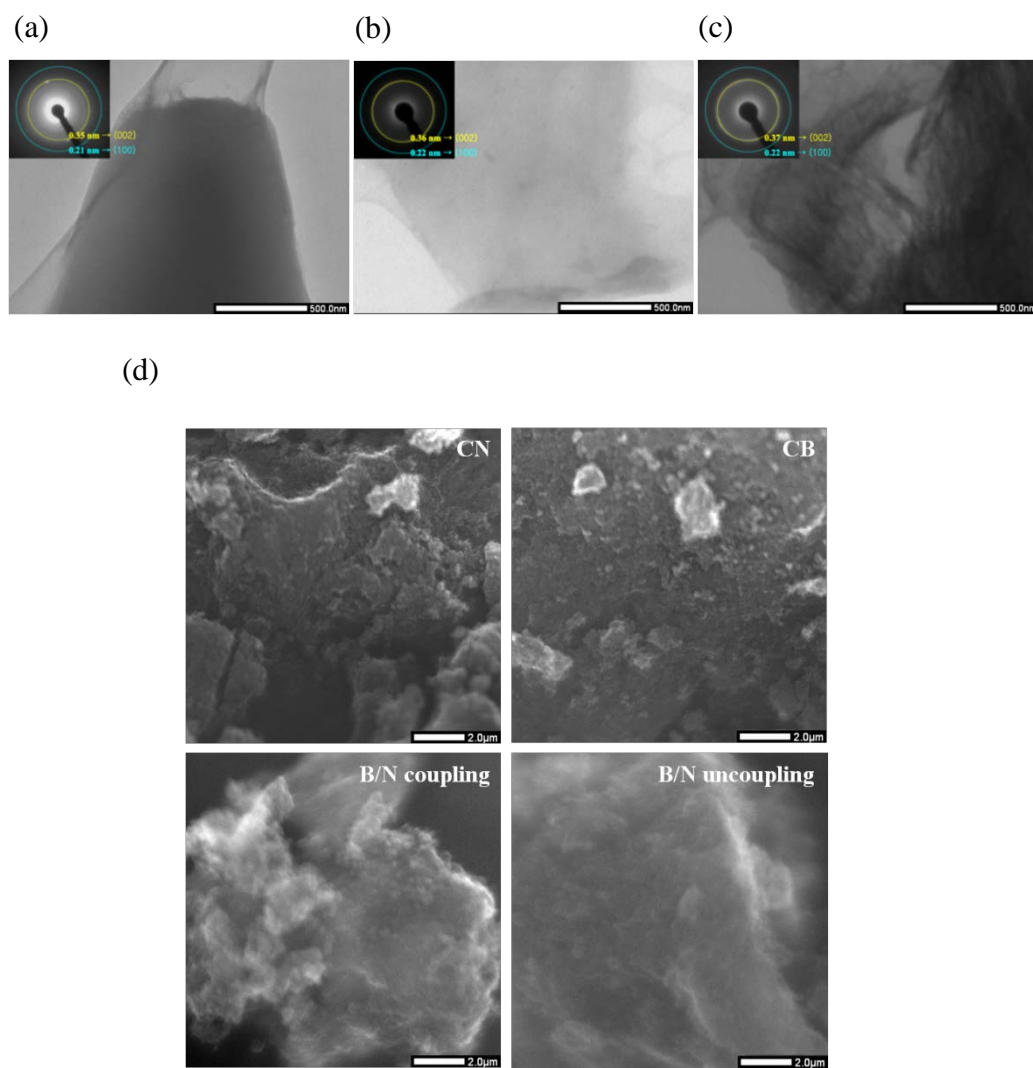
(a)   (b)   (c)

(d)

Fig. 4.8 Wide-field TEM images with selected-area electron diffraction (SAED) of (a) CB, (b) CN, and (c) B/N coupling. (d) SEM images of all nanocarbons.
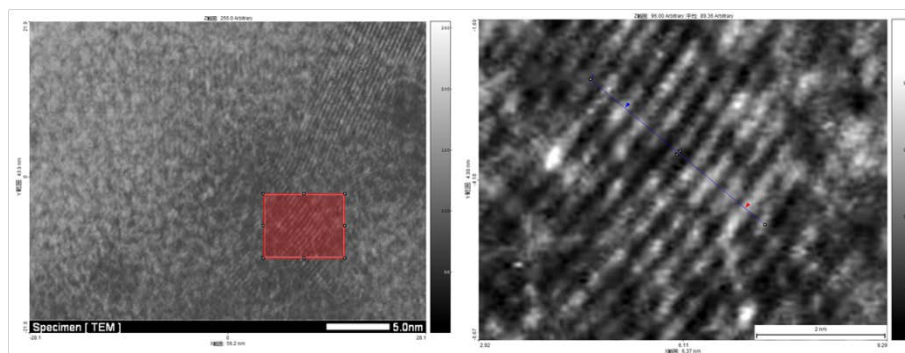
Fig. 4.9 Contrast line profiles of B/N uncoupling.
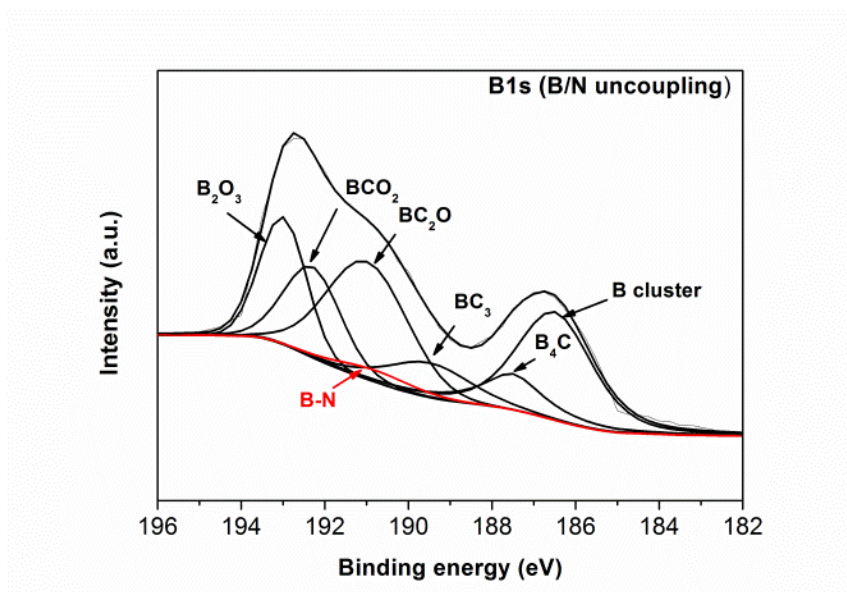
4.3.3 Content and bonding of nitrogen and boron

To figure out how nitrogen and boron dopant increases the ORR activity in the nanocarbon, XPS was conducted to measure the content and bond of the dopants in each catalyst. Table 4.1 shows the calculated mass concentration of different atoms in CN, CB, B/N coupling, and B/N uncoupling nanocarbon. The B/N coupling has a higher content of nitrogen (5.71 %) than B/N uncoupling (3.80 %), while the boron content in B/N coupling (0.54 %) is lower than that in B/N uncoupling (1.20 %). Although, B/N coupling shows a higher relative doping in nitrogen and boron to carbon of 7.03 % than B/N uncoupling, which has 5.58 % dopants, the catalytic activity of B/N uncoupling is better than that of B/N coupling

Table 4.1 The calculated mass concentration of different atoms in CN, CB, B/N coupling, and B/N uncoupling nanocarbon.
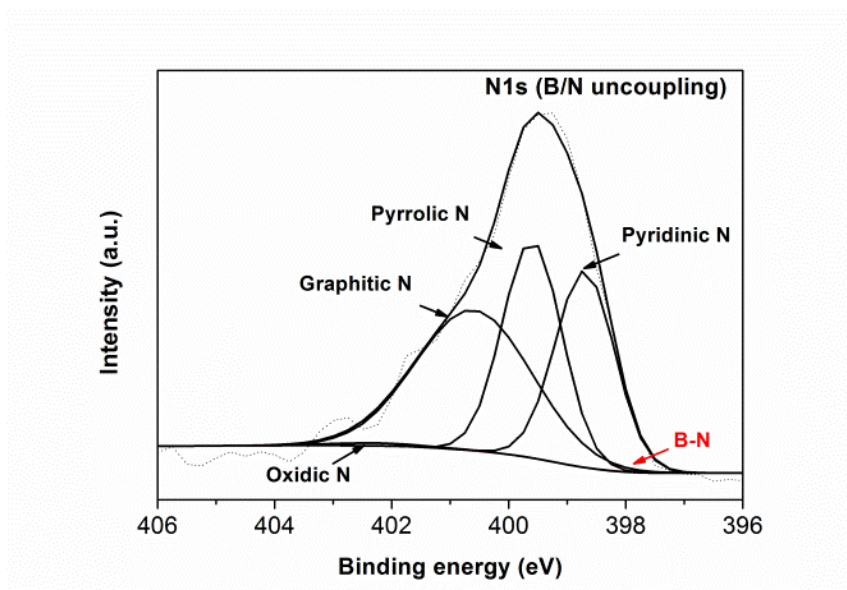
	C (at.%)	O (at.%)	N (at.%)	B (at.%)	Relative doping (%)
CN	90.10	4.70	5.20	-	5.77
CB	97.09	2.08	-	0.83	0.85
B/N coupling	88.82	4.93	5.71	0.54	7.03
B/N uncoupling	89.60	5.40	3.80	1.20	5.58

Fig. 4.10, typical XPS spectra of N1s and B1s exhibit significantly different chemical states of the constituent species for B and N co-doped coupling and uncoupling bond state obtained using different precursors. The B1s peak was deconvoluted using seven different binding energies corresponding to B cluster (186.5 eV), B_4C (187.5 eV), BC_3 (189.5 eV), BC_2O (191.0 eV), B-N (190.8 eV), BCO_2 (192.3 eV), B_2O_3 (193.0 eV). [12, 49, 50] The N1s XPS peak is comprised of the B-N, pyridinic N, pyrrolic N, graphitic N and, oxidic N peaks at 398.7, 399.96, 400.6 and 402.3 eV, respectively.[12, 51-53] The XPS spectra of C1s of BCN nanocarbon are shown in Fig. 4.11, where no significant difference between B/N coupling and B/N uncoupling catalyst was observed. In both cases, C-B and C-N bonds were identified. In the case of B/N uncoupling, B and N atoms can be incorporated in different positions in carbon framework (Fig. 4.12). The B1s and N1s spectra of B/N uncoupling show little to no contribution from the peak at 190.8 eV and 398.2 eV corresponding to B-N bond (Fig. 4.10 (a) and (b)). [10, 12] On the other hand, in the case of B/N coupling nanocarbon, the XPS spectra for N1s and B1s clearly indicate the presence of a significant amount of B-N bond, suggesting that the introduced starting precursor is well integrated into the BCN nanocarbon structure. [10-12, 54, 55] In particular, when nitrogen and boron co-doped into carbon framework, the XPS data are different to that of nitrogen mono-doped carbon. The broadening of graphitic N is in accordance with other results for B and N coped carbon materials. [12, 13, 17] This is because of the interaction among C, N, and B which can influence the chemical bond structure.
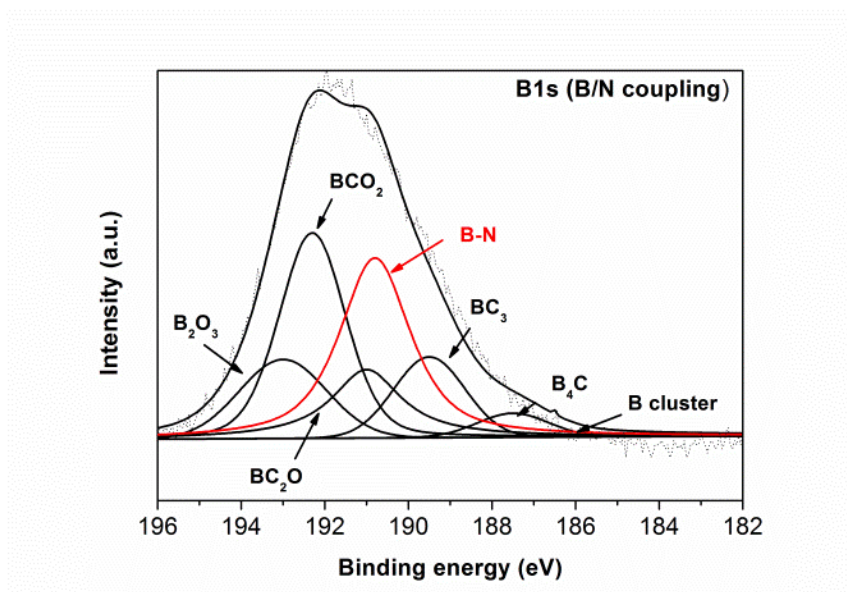
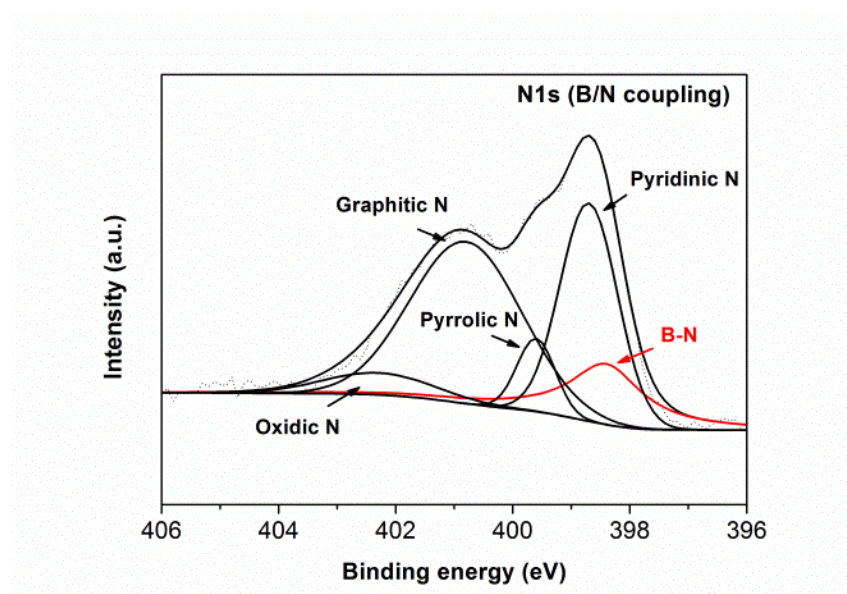(a)

(b)

(c)

(d)

Fig. 4.10 Narrow scan XPS of (a) B1s and (b) N1s of B/N uncoupling and (c) B1s and (d) N1s of B/N coupling. The spectra were deconvoluted by Gaussian fitting corresponding to the instrumental parameters of the device.
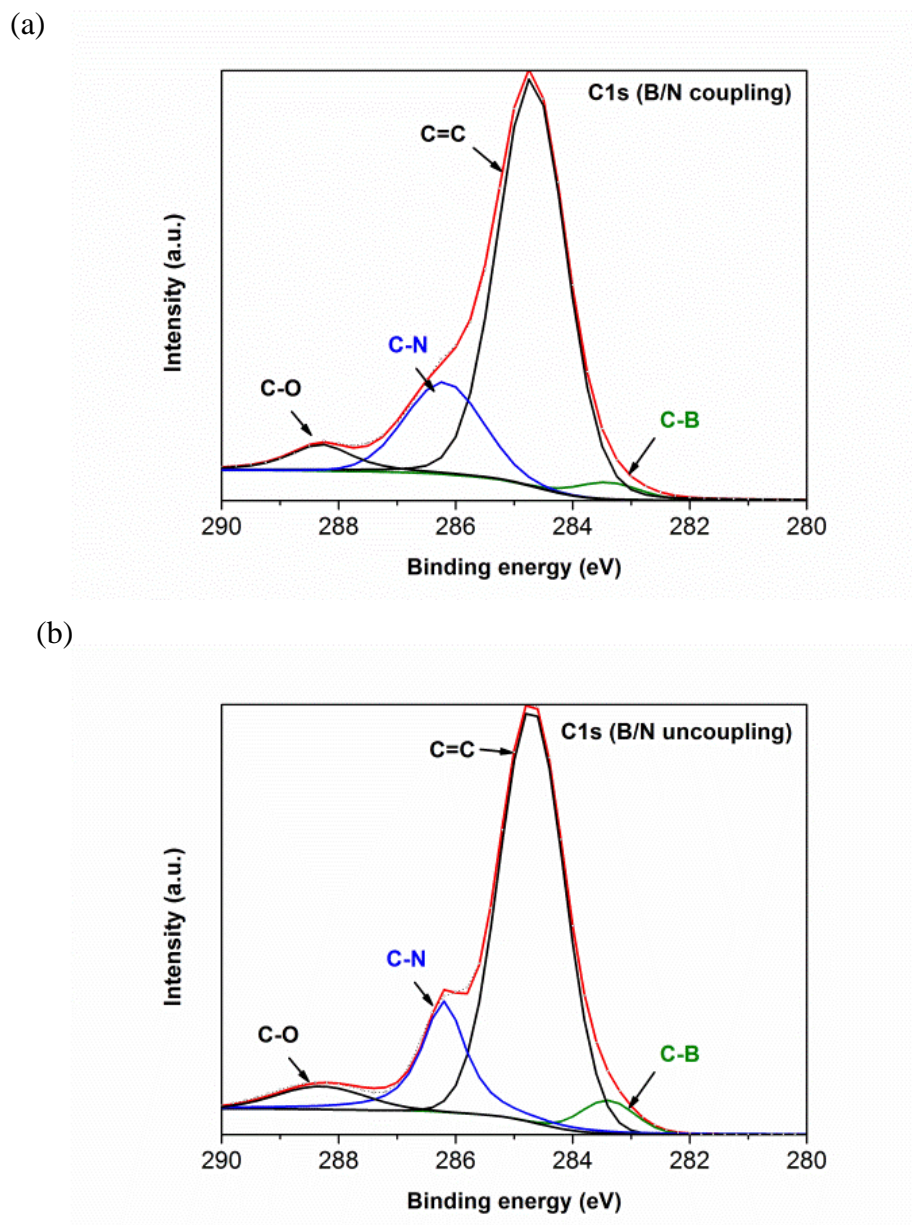
Fig. 4.11 Narrow scan XPS of (a) B/N uncoupling and (b) B/N coupling for C1s. The four deconvoluted peaks in the high resolution C1s spectrum at 283.4, 284.7, 286.2 and 288.3 eV can be attributed to C-B, C=C, C-N and C-O bonds, respectively. [13]
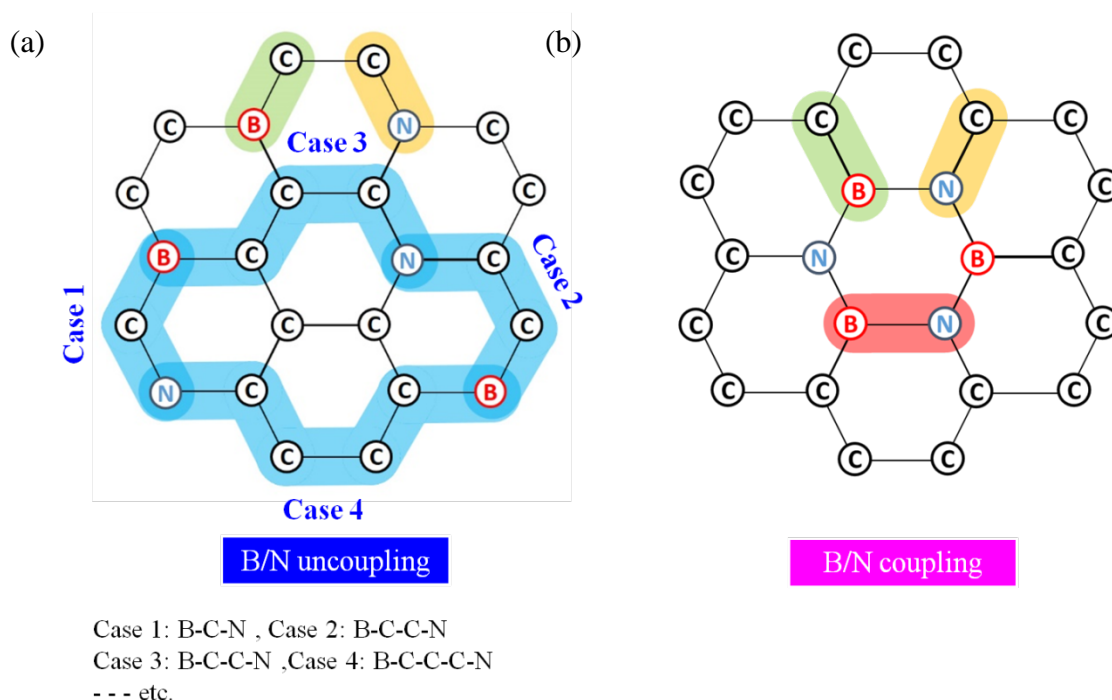
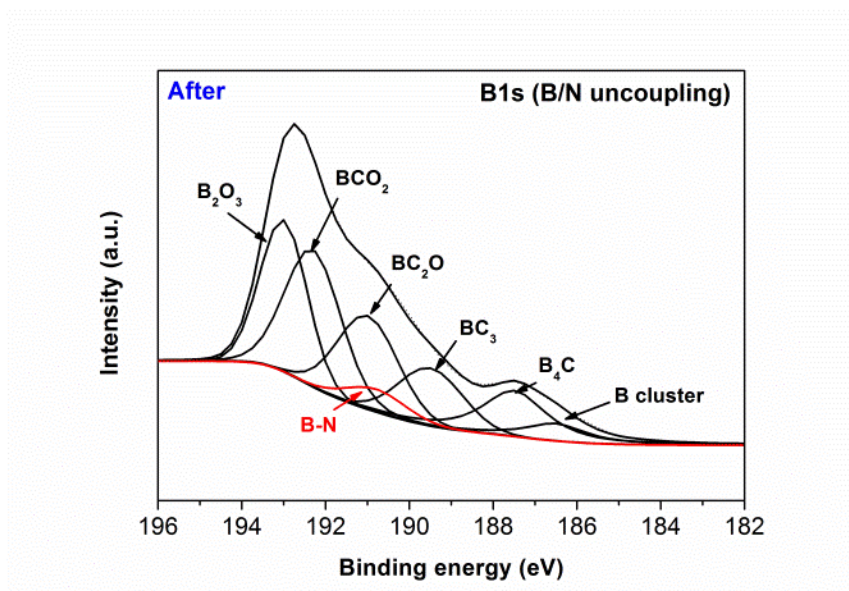**Fig. 4.12** Possible schematic structure of BCN nanocarbon: (a) B/N uncoupling and (b) B/N coupling.

Consequently, the presence of B-N bond in B/N coupling nanocarbon affects the deconvolution of nitrogen spectra, which means that the proportion of pyrrolic N decreases as compare to the absence of B-N bond in B/N uncoupling nanocarbon. The conclusion of these findings is that the formation of B-N bond was associated mainly with the pyrrolic N in B/N coupling material.

In From the comparison with ORR result in Fig. 4.3, it is demonstrated that the presence of B-N bond in B/N coupling nanocarbon contributes to a poor ORR activity. [12] The direct bond between nitrogen and boron leads to compensation of the electroneutrality in the *sp2* carbon framework, which means that the electrons provided by nitrogen combine with the empty orbitals provided by boron, leaving no electron or empty orbital conjugated into the carbon system. Thus, the electronic structure cannot be activated, due to the uninduced the
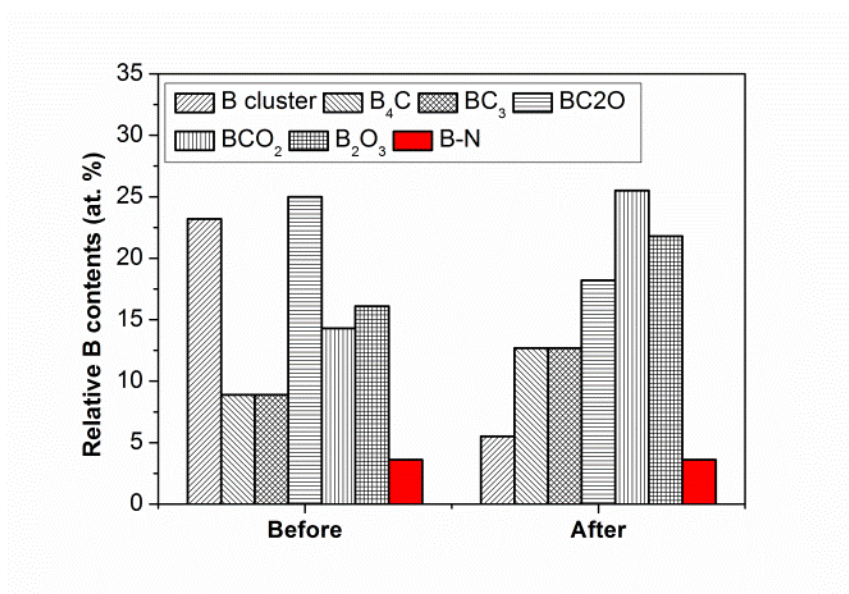
host-guest electronic interaction. [30] However, B/N uncoupling nanocarbon shows good activity for ORR. Here, nitrogen and boron atoms bonded to carbon atoms separately play the role of an electron donor and acceptor which facilitate the charge transfer in the nanocarbon, leading to a unique electronic structure with a synergistic co-doping effect. The critical point related to the ORR activity of the B/N uncoupling catalyst is the charge delocalization of the carbon atoms. It was revealed that the carbon π electrons in the nitrogen doping nanocarbon, which is an electron rich structure, can be activated by conjugation with the lone-pair electrons from nitrogen. In this way, the oxygen molecule can be reduced on the positively charged carbon atoms surrounding nitrogen. Nanocarbon doped with boron is a deficient electron structure so that the vacant orbital of boron is conjugated with the π electrons of carbon. Consequently, the adsorbed oxygen molecules on boron atoms are reduced on the positively charged boron atoms. [11-15]

The chemical states of the constituent species explain the durability experiment of the BCN electrocatalyst. The XPS analysis shows the chemical bond in the B/N uncoupling catalyst after the chronoamperometry measurements during 20000 s. The C-B and C-N bonds (B_4C, BC_3, pyridinic N, and pyrrolic N) were almost preserved after the durability test. However, B cluster and graphitic N bond decreased. Furthermore, the boron oxide bond (BCO_2 and B_2O_3) increased (Fig. 4.13 and Table 4.2). Based on XPS results, the C-N and C-B bonds indicate almost no change after the durability test, suggesting a stability of the N and B in the carbon structure against oxidation. [13, 35] After the durability experiment, the XPS spectra of Pt 20 wt. % on graphitized carbon show an increased amount of oxidized states of platinum, which can explain the lower catalytic stability of this material than B/N uncoupling nanocarbon as shown in Fig 4.14

(a)

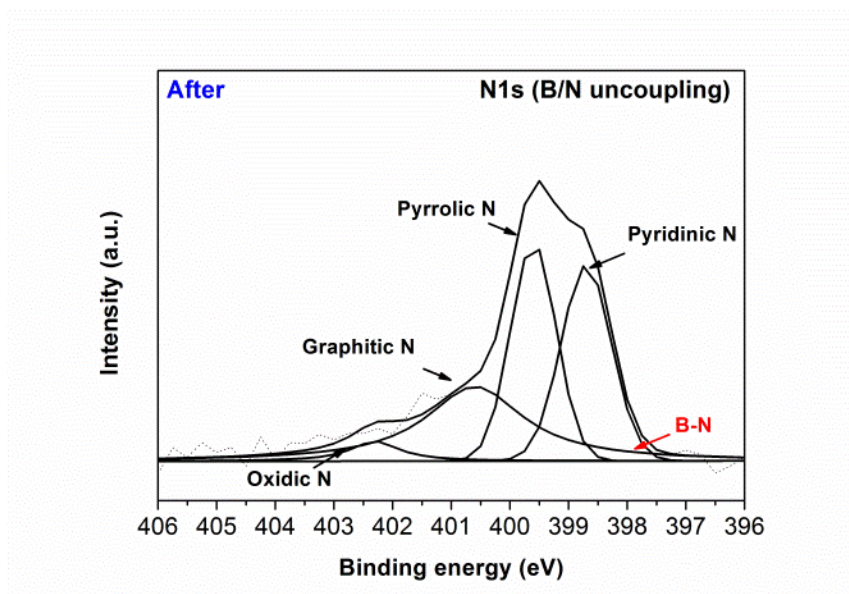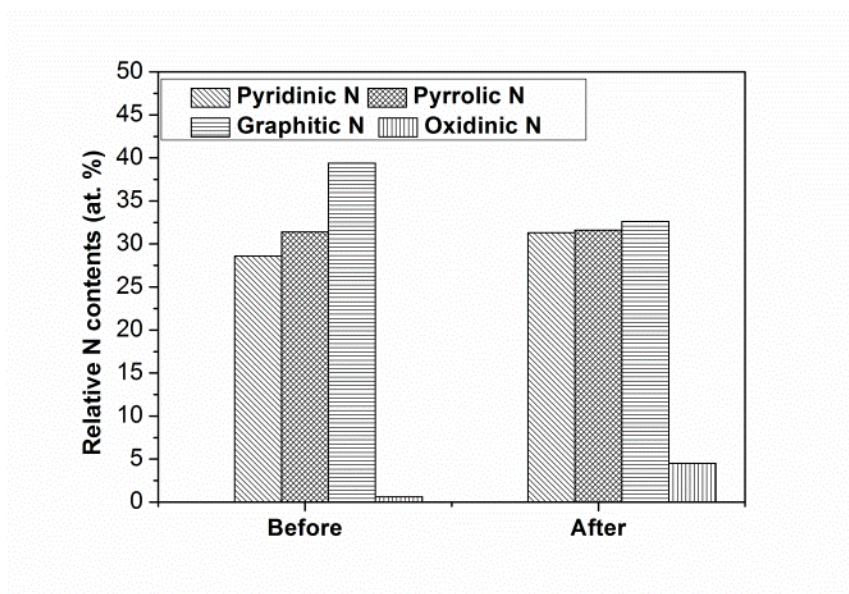

(b)

(c)

(d)

Fig. 4.13 Narrow scan XPS of (a) B1s and (c) N1s of B/N uncoupling after durability experiment. The relative contents of elements before and after the durability experiment for (b) boron and (d) nitrogen of B/N uncoupling.

Table 4.2 Relative content of (a) B atom (b) N atom and (c) Pt atom before and after chronoamperometry test.

	(a) Chemical state containing B atom (%)						
	B cluster	**B$_4$C**	**BC$_3$**	**BC$_2$O**	**BCO$_2$**	**B$_2$O$_3$**	**B-N**
Before	23.2	8.9	8.9	25	14.3	16.1	3.6
After	5.5	12.7	12.7	18.2	25.5	21.8	3.6

	(b) Chemical state containing N atom (%)				
	B-N	**Pyridinic N**	**Pyrrolic N**	**Graphitic N**	**Oxidic N**
Before	0	28.6	31.4	39.4	0.6
After	0	31.3	31.6	32.6	4.5

	(c) Chemical state containing Pt atom (%)					
	Pt^{4+}(4f5/2)	**Pt^{4+}(4f7/2)**	**Pt^{2+}(4f5/2)**	**Pt^{2+}(4f7/2)**	**Pt^0(4f5/2)**	**Pt^0(4f7/2)**
Before	2.8	3.1	7.5	11	40.8	34.8
After	4.6	5.6	15.8	20.1	26	27.9

(a)

(b)

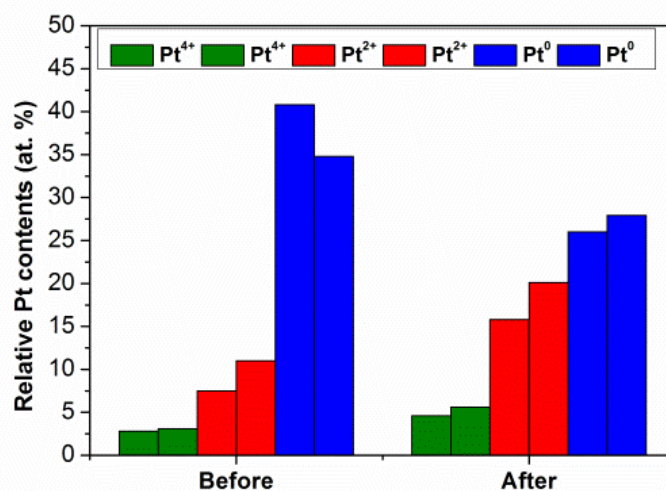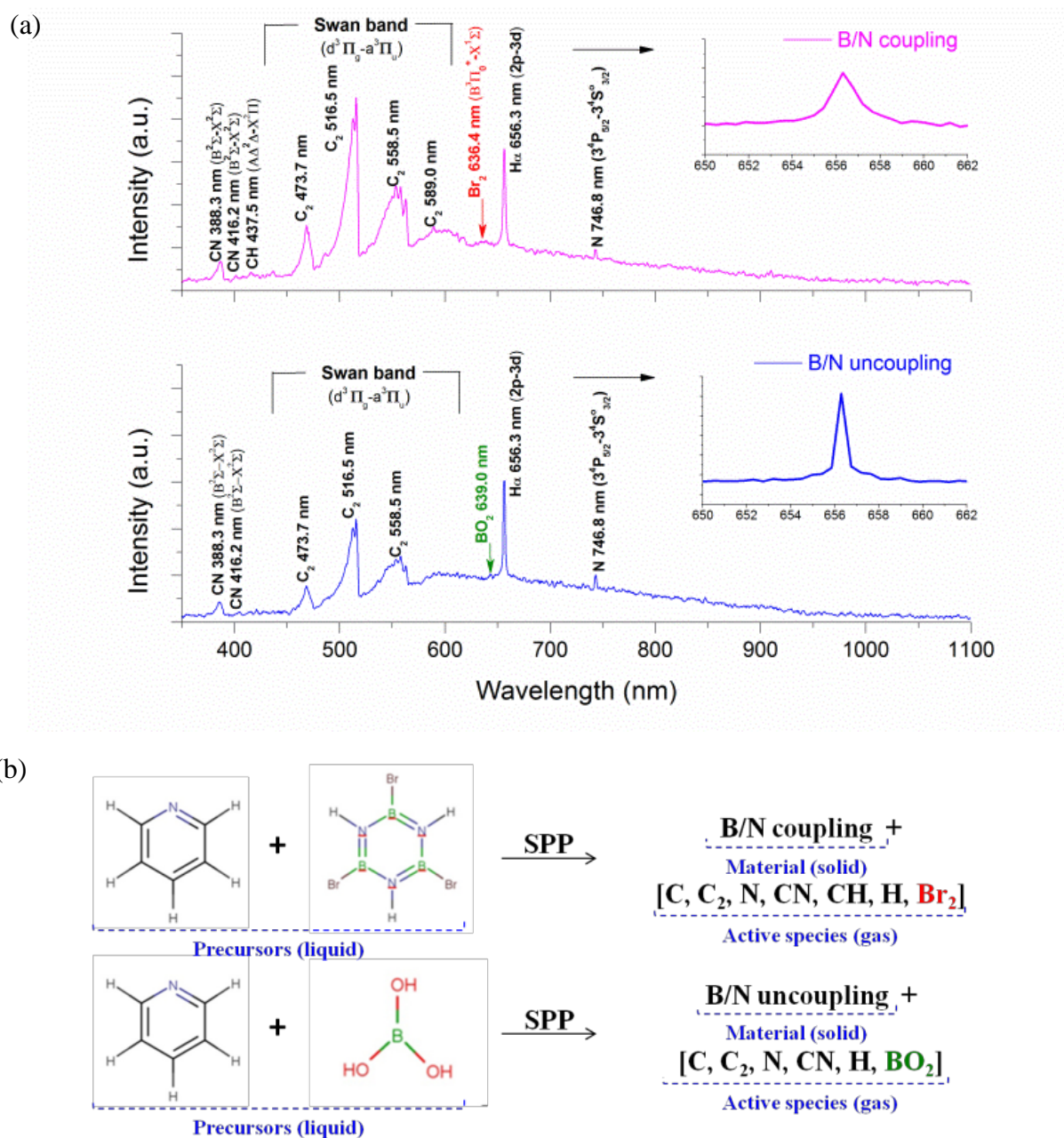**Fig. 4.14** XPS narrow scan after durability experiment of (a) Pt4f of 20 wt. % Pt/C and the relative element contents before and after the chronoamperometry for (b) Pt.

To explain the BCN nanocarbon synthesis, we performed some plasma diagnostics. The B/N coupling contains the N-B bond from the original precursor after the SPP making this method a useful tool to control the material composition. The OES data show the dissociation degree of the precursors in the SPP and the presence of the active species as radicals in the plasma gas phase. The OES measurements give the relative values of the emission intensities so that only a comparative discussion is valid. [56] The Swan bands of the C_2 molecule emission are about 1.4 times higher intensity in the case of plasma during the synthesis of the B/N coupling nanocarbon than that for the B/N uncoupling, indicating a higher dissociation degree of pyridine. The C_2 radicals play a significant role in the formation and growth of carbon materials as was demonstrated in the other SPP experiments. [36, 57-60] This means that the amount of carbon in the B/N coupling nanocarbon might be higher than in the B/N uncoupling nanocarbon, determining a smaller conductivity and as a consequence a poor ORR activity. [61] The appearance of CN, CH, C, and N radicals is also due to pyridine decomposition. From the dissociation of boric acid and B-tribromoborazine containing hydroxyl and bromine, respectively, a tiny band of the BO_2 radical, and a band of the Br_2 molecule appeared in the OES. [62] It is measured that the pure pyridine during the discharge in order to compared with the addition of boric and B-tribromoborazine as exhibited in Fig 4.16. The H-alpha line was broader in plasma used for the B/N coupling than that for the B/N uncoupling indicating a higher electron density, and consequently, a large number density of C_2 molecule formation and excitation since the dissociation of the organic compounds is mainly done through electron collisions. A schematic representation of the processes during the SP for the synthesis of the BCN nanocarbon is shown in Fig 4.15(b). In the low energy plasma, the bond structure of the precursor can be preserved and incorporated after discharge in the carbon material.

Fig. 4.15 (a) OES of the SPP during the synthesis of B/N coupling and B/N uncoupling nanocarbon materials. The insets in the spectra show the H-alpha line. (b) Schematics of the processes during the SP used for synthesis and control of the BCN nanocarbons. The active species in the gas phase were deduced from OES.
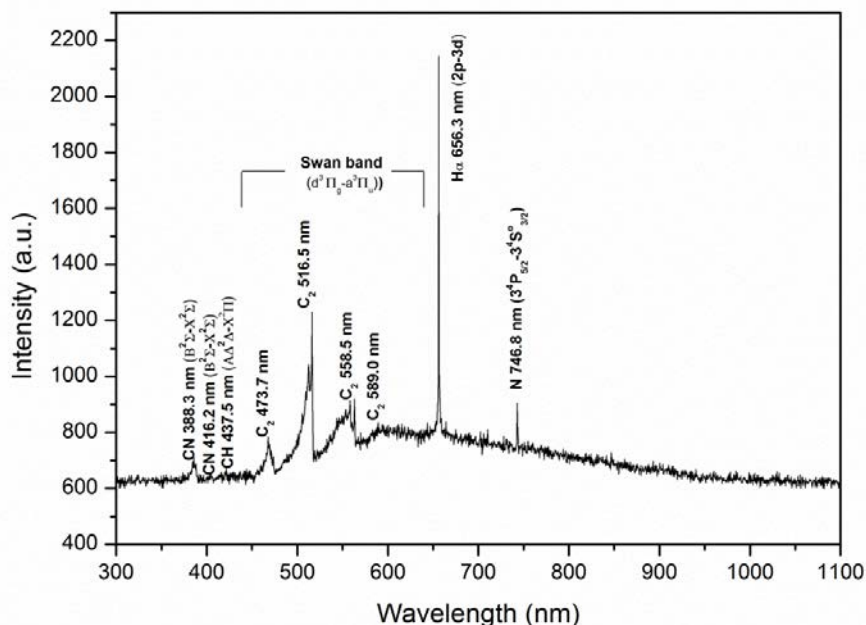
Fig. 4.16 OES spectra of the SPP in pure pyridine for synthesis CN (nitrogen doped carbon).

4.4 Conclusion

In summary, two types of BCN nanocarbon materials presenting electrocatalytic activity ORR with a coupling and uncoupling bond state between N and B atoms have been controlled by synthesis in a one-step, fast, and easy solution plasma process. The SPP provides the possibility of simultaneous production of nanocarbon co-doped with heteroatoms. The synthesis time was much shorter the conventional method such as CVD and chemical process. The B and N bond states can be controlled by selecting the precursors in plasma in organic solutions. The plasma energy was pretty low to conserve the B-N bond. With N and B atoms bonded together, the BCN nanocarbon contributes to a reduced ORR activity by forming a balanced electronic structure in the carbon framework. Meanwhile, the synergetic effect of N and B atoms with an uncoupling bond state improved the formation of active sites for the ORR

performance by the charge delocalization.

REFERENCES

[1] M. Kawaguchi, *Advanced Materials,* 1997, **9**, 615-625.

[2] J. Jin, F. Pan, L. Jiang, X. Fu, A. Liang, Z. Wei, J. Zhang and G. Sun, *ACS Nano,* 2014, **8**, 3313–3321.

[3] K. Raidongia, A. Nag, K. P. S. S. Hembram, U. V. Waghmare, R. Datta and C. N. R. Rao, *Chemistry A European Journal,* 2010, **16**, 149-157.

[4] O. Stephan, P. M. Ajayan, C. Colliex, R. H. Redlich, J. M. Lambert, P. Bernier and P. Lefin, *Science,* 1994, **266**, 1683-1685.

[5] L. Song, Z. Liu, A. L. M. Reddy, N. T. Narayanan, J. Taha-Tijerina, J. Peng, G. Gao, J. Lou, R. Vajtai and P. M. Ajayan, *Advanced Materials,* 2012, **24**, 4878–4895.

[6] J. D. R. Martins and H. Chacham, *ACS Nano,* 2011, **5**, 385–393.

[7] B. Wang, Y. Ma, Y. Wu, N. Li, Y. Huang and Y. Chen, *Carbon,* 2009, **47**, 2112 – 2115.

[8] S. Y. Kim, J. Park, H. C. Choi, J. P. Ahn, J. Q. Hou and H. S. Kang, *J. Am. Chem. Soc.,* 2007, **129**, 1705–1716.

[9] S. F. Huang, K. Terakura, T. Ozaki, T. Ikeda, M. Boero, M. Oshima, J. Ozaki and S. Miyata, *Physical Review B,* 2009, **80**, 235410.

[10] L. Ci, L. Song, C. Jin, D. Jariwala, D. Wu, Y. Li, A. Srivastava, Z. F. Wang, K. Storr, L. Balicas, F. Liu and P. M. Ajayan, *Nature Materials*, *2010*, **9**, 430-435.

[11] Y. Zhang, X. Zhuang, Y. Su, F. Zhang and X. Feng, *Journal of Materials Chemistry A,* 2014, **2**, 7742-7746.

[12] Y. Zhao, L. Yang, S. Chen, X. Wang, Y. Ma, Q. Wu, Y. Jiang, W. Qian and Z. Hu, *Journal of the American Chemical Society,* 2013, **135**, 1201–1204.

[13] L. Wang, P. Yu, L. Zhao, C. Tian, D. Zhao, W. Zhou, J. Yin, R. Wang and H. Fu, *Scientific Reports,* 2014**, 4**, 5184.

[14] S. Wang, L. Zhang, Z. Xia, A. Roy, D. W. Chang, J. N. Baek and L. Dai, *Angew. Chem. Int. Ed.,* 2012*, **51**, 4209 -4212.

[15] T. Ikeda, M. Boero, S. F. Huang, K. Terakura, M. Oshima, J. Ozaki and S. Miyata, *J. Phys. Chem. C,* 2010*, **114**, 8933–8937.

[16] J. P. Paraknowitsch, A. Thomas, *Energy & Environmental Science,* 2013*, **6**, 2839-2855.

[17] Y. Zheng, Y. Jiao, L. Ge, M. Jaroniec and S. Z. Qiao, *Angew. Chem. Int. Ed.,* 2013*, **125**, 3192-3198.

[18] H. Fei, R. Ye, G. Ye, Y. Gong, Z. Peng, X. Fan, E. L. Samuel, P. M. Ajayan and J. M. Tour, *ACS Nano,* 2014, **8**, 10837-10843.

[19] J. Wu and H. Yang, *Accounts of Chemical Research,* 2013*, **46**, 1848-1857.

[20] M. K. Debe, *Nature,* 2012*, **486**, 43–51

[21] Y. Nie, L. Li and Z. Wei, *Chem. Soc. Rev.,* 2015*, **44**, 2168-2201.

[22] Y. Shao, J. Liu, Y. Wang and Y. Lin, *J. Mater. Chem.,* 2009*, **19**, 46-59.

[23] R. L. McCreery, *Chem. Rev.,* 2008*, **108**, 2646-2687.

[24] S. Pylypenko, A. Queen, T. S. Olson, A. Dameron, K. O'Neill, K. C. Neyerlin. B. Pivovar. H. N. Dinh. D. S. Ginley. T. Gennett and R. O'Hayre, *J. Phys. Chem. C,* 2011*, **115**, 13667-13675.

[25] I. Dumitrescu, P. R. Unwin and J. R. Macpherson, *Chem. Commun.,* 2009*, **45**, 6886-6901.

[26] D. W. Wang and D. Su, *Energy & Environmental Science,* 2014*,**7**, 576-591.

[27] N. Daems, X. Sheng, I. F. J. Vankelecoma and P. P. Pescarmona, *J. Mater. Chem. A,* 2014,**2**, 4085-4110.

[28] Y. Zheng, Y. Jiao, M. Jaroniec, Y. Jin and S. Z. Qiao, *Small,* 2012*, **8**, 3550-3566.

[29] L. Dai, Y. L. Xue, L. L. Qu, H. J. Choi and J. B. Baek, *Chem. Rev.,* 2015*,* **115**, 4823-4892.

[30] S. Wang, E. Iyyamperumal, A. Roy, Y. Xue, D. Yu and L. Dai, *Angew. Chem. Int. Ed.,* 2011*,* **50**, 11756-11760.

[31] M. P. Levendorf, C. Kim, L. Brown, P. Y. Huang, R. W. Havener, D. A. Muller and J. Park, *Nature,* 2012*,* **488**, 627-632.

[32] C. Chang, S. Kataria, C. Kuo, A. Ganguly, B. Wang, J. Hwang, K. Huang, W. Yang, S. Wang and C. Chuang, M. Chen, C. Huang, W. Pong, K. Song, S. Chang, J. Guo, Y. Tai, M. Tsujimoto, S. Isoda, C. Chen, L. Chen, and K. Chen, *ACS Nano,* 2013*,* **7**, 1333-1341.

[33] T. Wu, H. Shen, L. Sun, B. Cheng, B. Liu, J. Shen, *New J .Chem.,* 2012*,* **36**, 1385-1391.

[34] X. H. Li, M. Antonietti, *Angew. Chem. Int. Ed.,* 2013*,* **52**, 4572- 4576.

[35] Y. Su, Y. Zhang, X. Zhuang, S. Li, D. Wu, F. Zhang and X. Feng, *Carbon,* 2013*,* **62**, 296-301.

[36] G. Panomsuwan, S. Chiba, Y. Kaneko, N. Saito and T. Ishizaki, *J. Mater. Chem. A,* 2014*,* **2**, 18677-18686.

[37] G. Panomsuwan, N. Saito and T. Ishizaki, *Carbon,* 2016*,* **98**, 411-420.

[38] G. Panomsuwan, N. Saito and T. Ishizaki, *J. Mater. Chem. A,* 2015*,* **3**, 9972-9981.

[39] D. W. Kim, O. L. Li, P. Pootawang and N. Saito, *RSC Adv,* 2014*,* **4**, 16813-16819.

[40] D. Kim, O. L. Li and N. Saito, *Phys. Chem. Chem. Phys.,* 2015*,* **17**, 407-413.

[41] J. Senthilnathan, C. C. Weng, J. D. Liao and M. Yoshimura, *Scientific Reports,* 2013, **3**, 2414.

[42] NIST X-ray Photoelectron Spectroscopy Database, Version 4.1 (National Institute of Standards and Technology, Gaithersburg, 2012); http://srdata.nist.gov/xps/.

[43] W. Xing, G. Yin, J. Zhang, Rotating Electrode Methods and Oxygen Reduction Electrocatalysts, Elsevier, Amsterdam, 2014; Chapter 6, pp. 199-229.

[44] Z. Q. Li, C. J. Lu, Z. P. Xia, Y. Zhou and Z. Luo, *Carbon,* 2007, **45**, 1686-1695.

[45] AC. Ferrari and J. Robertson, *Physical Review B,* 2000, **61**, 14095-14107.

[46] L. G. Cancado, K. Takai and T. Enoki, *Applied Physics Letters,* 2006, **88**, 163106.

[47] A. Rubio, J. L. Corkill and M. L. Cohen, *Physical Review B,* 1994, **49**, 5081-5084.

[48] P. Paredez, M. E. H. Maia da Costa, L. F. Zagonel, C. T. M. Ribeiro and F. Alvarez, *Carbon,* 2007, **45**, 2678-2684.

[49] L. Yang, S. Jiang, Y. Zhao, L. Zhu, S. Chen, X. Wang, Q. Wu, J. Ma, Y. Ma and Z. Hu, *Angew. Chem. Int. Ed.,* 2011, **123**, 7270-7273.

[50] L. G. Jacobsohn, R. K. Schulze, M. E. H. Maia da Costa and M. Nastasi, *Surface Science,* 2004, **572**, 418-424.

[51] L. Lai, J. R. Potts, D. Zhan, L. Wang, C. K. Poh, C. Tang, H. Gong, Z. Shen, J. Lin and R. S. Ruoff, *Energy Environ. Sci.,* 2012, **5**, 7936-7942.

[52] E. J. Biddinger, v. D. Deak and S. O. Ozakan, *Topics in Catalysis,* 2009, **52**, 1566-1574.

[53] H. Wang, T. Maiyalagan and X. Wang, *ACS Catal.,* 2012, **2**, 781-794.

[54] D. H. Berns and M. A. Cappelli, *Appl. Phys. Lett.,* 1996, **68**, 2711-2713.

[55] M. C. Polo, E. Martínez, J. Esteve and J. L. Andújar, *Diamond and Related Materials,* 1998, **7**, 376-379.

[56] M. Plank, *Annalen der Physik,* 1901, **4**, 1-6.

[57] S. M. Kim, Y. K. Heo, K. T. Bae, Y. T. Oh, N. H. Lee and S. Y. Lee, *Carbon,* 2016, **101**, 420-430.

[58] O. Matsuda, N. Ohno and S. Takamura, *Plasma Sources Sci. Technol.,* 1996, **5**, 356–362.

[59] Y. Yang, X. Liu, X. Guo, H. Wen and B. Xu, *J. Nanopart. Res.,* 2011, **13**, 1979-1986.

[60] N. Sano, H. Wang, I. Alexandrou, M. Chhowalla, K. B. K. Teo, G. A. J. Amaratunga and K. Limura, *J. Appl. Phys.,* 2002, **92**, 2783-2788.

[61] H. S. Lee, T. Ueno, N. Saito, *The Surface Finishing Society of Japan,* 2015, **66**, 416-9.

[62] R. W. B. Pearse and A. G. Gaydon, The Identification of Molecular Spectra, Chapman and Hall, New York, 1976

Chapter 5
Summary

Chapter 5 Summary

5.1 Summary of the thesis

In this thesis, metal-free hetero-nanocarbons based electocatalyst for ORR have been synthesized by tune-up solution plasma.

In chapter 2, the non-equilibrium SP condition, in terms of, tune-up SP at which the electron energy was higher than the ion energywas controlled by introducing the RC component in the plasma circuit. In the SP discharge, the maximum discharge current of the low-pass filter circuit was 13 A, which was higher than 6 A of the conventional circuit. The frequency and amplitude of the current oscillations related to the ion oscillations were decreased by means of low-pass filter circuit, leading to the enhanced SP discharge stability. From the analyses of OES, it was found that the low-pass filter circuit provided a higher electron density and temperature (i.e., higher electron energy) compared with the conventional circuit. The modified SP circuit increasing the electron energy will provide an effectiveway to synthesize metastable materials formed under the non-equilibrium condition.

In chapter 3, we suggest a novel route to synthesize nitrogen doped graphitic carbon nanosheets (NGS), using a tune-up solution plasma system. The proposed method gives several advantages over assembling of nanocarbons: (a) one-step process, (b) ambient reaction environment, (c) straightforward and easy setup, (d) cost-effective production, (e) possible large-scale of synthesis quantities, and (f) eco-friend fabrication. In particular, the tune-up SP synthesis provides stability during the discharge in liquid, influencing the synthesized nanocarbon characteristics. The NGS material has not only a large surface area, high nitrogen content, good electrical conductivity, but also the appropriate active N species of a catalyst to

enhance the ORR activity. In detail, the electrochemical measurements demonstrate that NGS shows comparable catalytic activity and superior stability to Pt/C in alkaline medium, so that a low cost and large scale of nitrogen self-doped nanocarbon is a promising candidate for the next generation of electrocatalyst in metal-air batteries.

In chapter 4, two types of BCN nanocarbon materials presenting electrocatalytic activity ORR with a coupling and uncoupling bond state between N and B atoms have been controlled by synthesis in a one-step, fast, and easy solution plasma process. The solution plasma synthesis provides the possibility of simultaneous production of nanocarbon co-doped with heteroatoms. The synthesis time was much shorter the conventional method such as CVD and chemical process. The B and N bond states can be controlled by selecting the precursors in plasma in organic solutions. The plasma energy was pretty low to conserve the B-N bond. With N and B atoms bonded together, the BCN nanocarbon contributes to a reduced ORR activity by forming a balanced electronic structure in the carbon framework. Meanwhile, the synergetic effect of N and B atoms with an uncoupling bond state improved the formation of active sites for the ORR performance by the charge delocalization. Although the onset potential and activity of N and B doped nanocarbon are still not as good as those of commercial Pt/C, its good ORR activity, more reliable stability, and low cost make N and B nanocarbon materials a promising candidate for the next generation of catalysts for ORR in alkaline media.

Achievements

List of publication

[1] Generation of non-equilibrium condition in solution plasma discharge using low-pass filter circuit ; Yong-Kang Heo, Seung-Hyo Lee, Maria Antoaneta Bratescu, Sung-Min Kim, Gyoung-Ja Lee, Nagahiro Saito, Plasma Process Polym 2016; 9999: e201600163

[2] Enhancement of Nitrogen Self-Doped Nanocarbons Electrocatalyst Activity via Tune-up Solution Plasma ; Seung-Hyo Lee, Maria Antoaneta Bratescu, Nagahiro Saito, (Under review, *RSC Advance*)

[3] Solution Plasma Synthesis of Boron-Carbon-Nitrogen Catalyst with Controllable Bond Structure ; Seung-Hyo Lee, Yong-Kang Heo, Maria Antoaneta Bratescu, Tomonaga Ueno, Nagahiro Saito, *Phys.Chem. Chem. Phys.*, 2017, 19, 15264-15272

List of presentation in international conferences

[1] Seung-Hyo Lee, Tomonaga Ueno, Nagahiro Saito, "CN_x Nanosheets as Metal-Free Catalysts for the Oxygen Reduction Reaction by Solution Plasma Process", 7th International Symposium on Advanced Plasma Science and Its Applications for Nitrides and Nanomaterials / 8th International Conference on Plasma-Nano Technology & Science, March 26-31, 2015, Nagoya, Japan

[2] Seung-Hyo Lee, Tomonaga Ueno, Nagahiro Saito, "BNC Nanocarbon with tunable bond structure toward synergistically enhancing electrochemical oxygen reduction activity", The 16th International Symposium on Biomimetic Materials Processing (BMMP-15), January, 2015, Nagoya, Japan

[3] Seung-Hyo Lee, Tomonaga Ueno, Nagahiro Saito, "Synergistically Enhanced Electrochemical Activity (ORR) Nitrogen and Boron Doped Nanocarbon by Solution Plasma Process", Solution Plasma and Molecular Technologies (SPM-5), May 6-9, Bangkok, Thailand

[4]] Seung-Hyo Lee, Tomonaga Ueno, Nagahiro Saito, "Facile synthesis of nitrogen doped sheet like nanocarbon as enhanced electrocatalysts for Zn-air batteries", 2015 MRS Fall

Meeting, November 29-December 4, 2015, Boston, United State of America (USA)

[5] Seung-Hyo Lee, Tomonaga Ueno, Nagahiro Saito, "BNC Nanocarbon with tunable bond structure toward synergistically enhanced electrochemical oxygen reduction activity" The 16th International Symposium on Biomimetic Materials Processing (BMMP-16), January 22-26, Nagoya, Japan